RCA Review

NOT TO BE REMOVED FROM
NASA LIBRARY
AMES RESEARCH CENTER
NOV 26 1979
COPY NO. 1
MOFFETT FIELD, CALIF.

September 1979 Volume 40 No. 3

RCARCI 40(3) 239-368 (1979)

RCA Review, published quarterly in March, June, September and December by RCA Research and Engineering, RCA Corporation, Princeton, New Jersey 08540 Entered as second class matter July 3, 1950 under the Act of March 3, 1879 Second-class postage paid at Princeton, New Jersey, and at additional mailing offices Effective January 1, 1978, subscription rates as follows. United States and Canada: one year $8.00, two years $14.00, three years $18 00; in other countries, one year $8.60, two years $15 20, three years $19.80 Single copies (except for special issues) up to five years old $3.00

RCA Review

A technical journal published quarterly by RCA Research and Engineering in cooperation with the subsidiaries and divisions of RCA.

Contents

241 **Low-Loss Charge-Coupled Device**
Walter F. Kosonocky and Donald J. Sauer

278 **Analysis of the Effective Transfer Losses in a Low-Loss CCD**
Donald J. Sauer

295 **Review and Analysis of Laser Annealing**
A. E. Bell

339 **Laser Annealing to Round the Edges of Silicon Structures**
C. P. Wu and G. L. Schnable

345 **Optical Recording With the Encapsulated Titanium Trilayer**
A. E. Bell, R. A. Bartolini, and F. W. Spong

363 **Patents**

365 **Authors**

September 1979 Volume 40 Number 3 ISSN 0033-6831

RCA Corporation

E. H. Griffiths President and Chief Executive Officer

Editorial Advisory Board

Chairman, J. J. Tietjen RCA Laboratories

N. L. Gordon RCA Laboratories
G. C. Hennessy RCA Laboratories
E. O. Johnson RCA Research Laboratories, Inc
H. Kressel RCA Laboratories
C. H. Lane Picture Tube Division
D. S. McCoy RCA Research and Engineering
W. Merz Laboratories RCA, Ltd.
K. H. Powers RCA Laboratories
L. A. Shotliff International Licensing
T. O. Stanley, RCA Laboratories
W. M. Webster RCA Laboratories

Secretary, Charles C. Foster RCA Laboratories

Editor **Ralph F. Ciafone**

Associate Editors

D. R. Higgs Missile and Surface Radar Division
C. Hoyt Consumer Electronics
T. King RCA Research and Engineering
R. Mausler National Broadcasting Company
M. Rosenthal RCA Americom, Inc.
J. Schoen Solid-State Division
M. G. Pietz Government and Commercial Systems
W. S. Sepich Commercial Communicatons Systems Division
J. E. Steoger RCA Service Company
D. Tannenbaum Government Communications Systems

© RCA Corporation 1979. All rights reserved, except that express permission is hereby granted for the use in computer-based and other information-service systems of titles and abstracts of papers published in RCA Review.

Low-Loss Charge-Coupled Device*

Walter F. Kosonocky and Donald J. Sauer

RCA Laboratories, Princeton, N.J. 08540

Abstract—Two closed-loop CCD structures (256-stage and 1024-stage) were built to demonstrate a low-loss mode of operation for a very long CCD delay line or a closed-loop CCD structure. The low-loss CCD concept consists of operating a CCD with each signal-charge well followed by one or more trailing-bias-charge wells. An improvement of two orders of magnitude in the effective transfer losses was demonstrated experimentally by periodically recombining at a signal-regeneration stage the (first-order) signal-charge transfer losses collected by the trailing bias charges with the corresponding signal-charge packets. An effective transfer loss of 2.4×10^{-7} per transfer was demonstrated. The maximum time delay has also been improved by more than two orders of magnitude over that of conventional CCDs by means of a dark-current subtraction technique. The 256-stage closed-loop low-loss CCD was also operated as a synchronous signal correlator producing an improvement in the signal-to-noise ratio of 17.5 dB as a result of 100 signal recirculations in the loop.

1. Introduction

The typical charge transfer loss (charge transfer inefficiency) of a surface-channel CCD is on the order of 10^{-4} per transfer and for a buried-channel CCD it is on the order of 10^{-5} per transfer. The low-loss CCD[1] described in this paper represents a special mode of operation of a CCD structure that can result in about two orders of magnitude reduction in the effective charge transfer losses. This is achieved by operating the

* This work was supported by the Deputy for Electronic Technology (RADC/ET) Hanscom AFB, MA 01731.

CCD structure with each signal-charge well followed by one or more trailing-bias-charge wells. The function of trailing bias charge is to keep the trapping states in the CCD channel filled. A very low effective transfer loss is achieved by periodically recombining the charge transfer losses collected by the trailing-bias-charge wells with the corresponding signal-charge packets at low-loss signal-regeneration stages. By adjusting the level of the trailing bias charge to be above the signal-charge level, we can assure that the effective transfer losses in a low-loss CCD are reduced to the second-order trapping losses encountered by the trailing bias charge. These trapping losses are due to the modulation of the trailing-bias-charge level by the first-order trapping losses experienced by the signal-charge packets. Previously reported structures using isolation wells[2-4] did not use the large trailing-bias charge or periodic signal regeneration.

To demonstrate experimentally the low-loss CCD concept we have developed a low-loss CCD test chip that includes a 256-stage and a 1024-stage closed-loop low-loss CCD. In addition to low-loss signal regenerators, floating-gate output stages for nondestructive signal sensing, and input and output charge switching circuits, each of the closed-loop CCDs has been constructed with a dark-current-subtraction stage. The dark-current-subtraction technique described in this paper can extend the useful delay time of the signal in the closed-loop CCDs by more than two orders of magnitude.

2. Low-Loss CCD Test Array

2.1 General Description

To study the characteristics and the performance of the low-loss CCD concepts,[1] we have designed, fabricated, and operated a low-loss CCD test array. The test array that was designed and fabricated includes two separate 4.95 × 2.15 mm test chips. The photomicrograph in Fig. 1 shows the first test chip, which contains a 1024-stage closed-loop low-loss CCD, and the photomicrograph in Fig. 2 shows the second test chip, which contains a 256-stage closed-loop low-loss CCD and a number of process control test devices.

The low-loss CCD test chips were processed using a two-level polysilicon n-channel buried-channel CCD (BCCD) technology with non-self-aligned n^+ diffusions, p^+ channel stops, 1000-Å-thick channel oxide, and n^+ polysilicon gates processed with phosphorus-doped reflow glass. The BCCD channels are 25-μm wide. The gate structure has 10-μm polysilicon gates with 5-μm spaces, thus resulting in 30-μm-long CCD stages. The closed-loop CCD structures were designed to operate as a

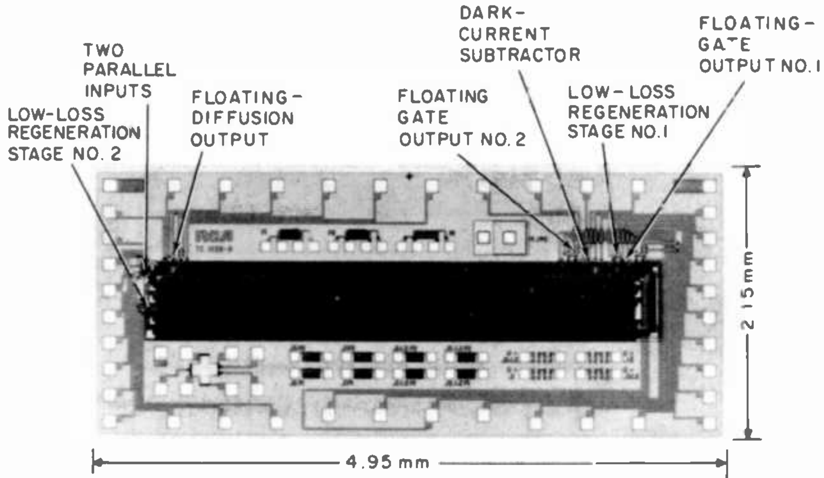

Fig. 1—Photomicrograph of 1024-stage closed-loop low-loss CCD test chip.

two-phase CCD with a dc offset voltage to be applied between the storage gates and the transfer gates, i.e., between the clock phases ϕ_{1S} and ϕ_{1T}, as well as ϕ_{2S} and ϕ_{2T}. The charge-corners of both closed loops were designed for a complete charge-transfer operation with the available two-phase CCD clocks.

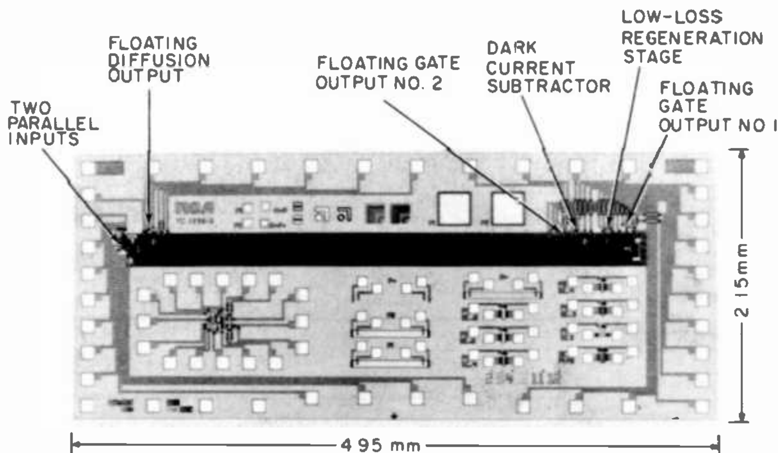

Fig. 2—Photomicrograph of 256-stage closed-loop low-loss CCD test chip.

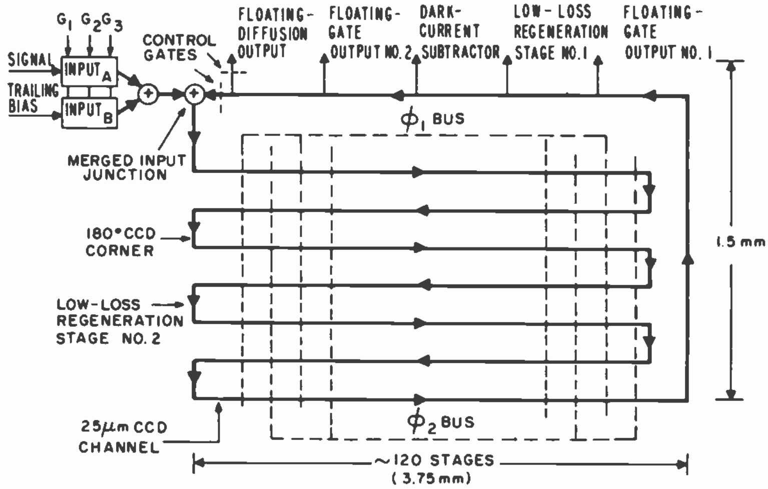

Fig. 3—Schematic of the layout of the 1024-stage low-loss CCD loop.

2.2 Features of the Closed-Loop Low-Loss CCDs

The schematics of the 1024-stage and 256-stage, closed-loop CCDs are shown in Figs. 3 and 4, respectively. Except that the larger closed-loop structure has two low-loss signal-regeneration stages, both of these structures have the same features, as described below.

2.2.1 Input Structure

The detailed layout of the input structure of the closed-loop CCDs is shown in Fig. 5. Two parallel input channels are provided: one is for the

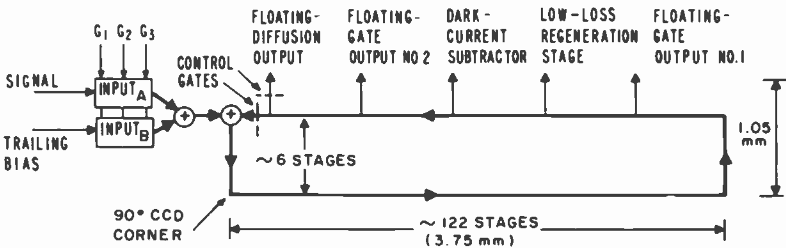

Fig. 4—Schematic of the 256-stage low-loss CCD loop.

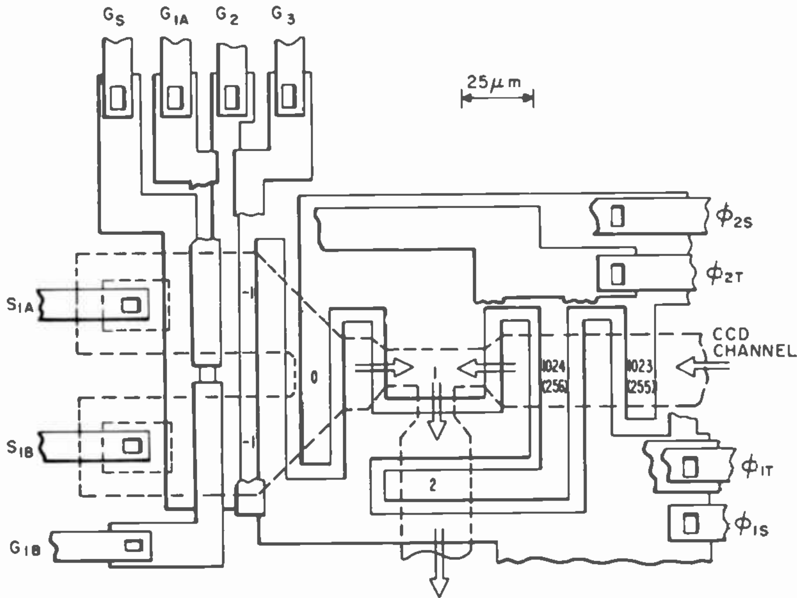

Fig. 5—Layout of parallel inputs and merged input junction.

signals, and the other is for introducing the trailing bias charge between the signal samples. These input channels are 35-μm wide to provide sufficient dynamic range for a full well in the main CCD register. The inputs are operated using standard charge preset (fill-and-spill), with a negative pulse on the input-source diffusions.

The input signals are introduced into the closed-loop CCD at the merged input junction. This junction is designed to operate as a signal adder. Thus, if the closed loop is empty, a new signal can be introduced into the loop. Moreover, an input signal can also be added to a signal already circulating in the loop. The direction of the signal flow is built into the merged input junction as designated by the arrows in Fig. 5.

2.2.2 Low-Loss Signal-Regeneration Stage

The detailed layout of the low-loss signal-regeneration stage #1 shown in the photograph in Fig. 1 is illustrated in Fig. 6. To increase the charge-handling capacity of the potential wells carrying the signal charge combined with the trailing bias charge, the width of the CCD channel at this stage was increased from 25 to 37.5 μm and the length of the storage gates G_{RGS} and G_{1S} was increased from 10 to 15 μm.

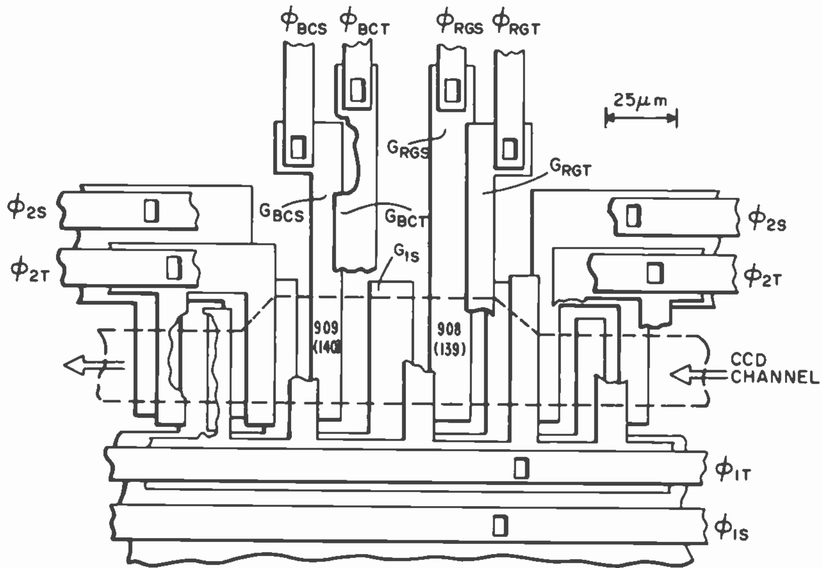

Fig. 6—Layout of the low-loss signal-regeneration stage.

Another design feature of the signal-regeneration stage that should be mentioned is the increased length of the trailing-bias-charge generating transfer gate, G_{BCT}. The length of this gate was increased from the typical value of 5 μm to 10 μm. The longer barrier formed under this transfer gate is provided to give lower charge-transfer loss at this incomplete charge transfer which separates the signal charge from the trailing bias charge.

The two low-loss signal-regeneration stages in the 1024-stage loop are laid out for operation with separate clock pulses. Thus, this loop can be operated with either one or two low-loss signal regenerations. Of course, there is always the possibility of operating the closed loop as a conventional two-phase CCD not involving low-loss signal regeneration. The operation of the low-loss signal-regeneration stage is described in Sec. 2.3.

2.2.3 Floating-Gate Outputs

Two floating-gate, nondestructive signal-sensing stages are placed in each loop on both sides of the low-loss signal-regeneration stage. In the case of the large loop, with a 1024-stage two-phase CCD, only one signal-regeneration stage has the associated floating-gate output stages.

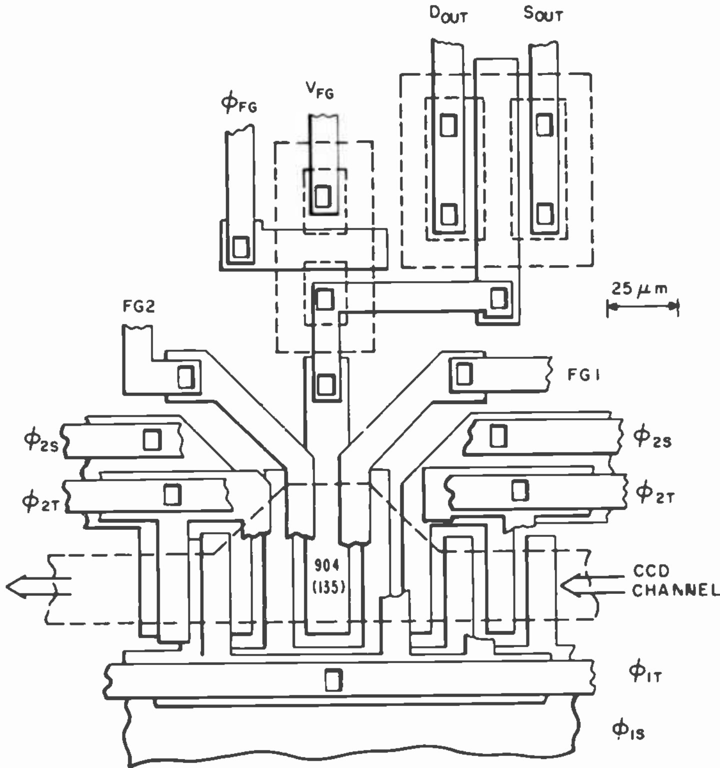

Fig. 7—Layout of the floating-gate output stage.

The layout of the floating-gate output stage is illustrated in Fig. 7. The signal-sensing floating gate of this stage can be periodically reset to a reference potential V_{FG} by a clock pulse ϕ_{FG}. The function of two externally controllable dc levels, FG1 and FG2, is to provide isolation from the two-phase clocks and to assure a complete charge transfer at this floating-gate output.[5]

2.2.4 Floating-Diffusion Output

The signal is removed from the closed-loop CCDs by the floating-diffusion output stage. This stage provides the destructive readout from the loop. The layout of the floating-diffusion output stage is shown in Fig. 8. The floating-diffusion output is controlled by the transfer pulses ϕ_{FDT} (floating-diffusion transfer) and ϕ_{REC} (recirculation transfer) operating in conjunction as complementary pulses.

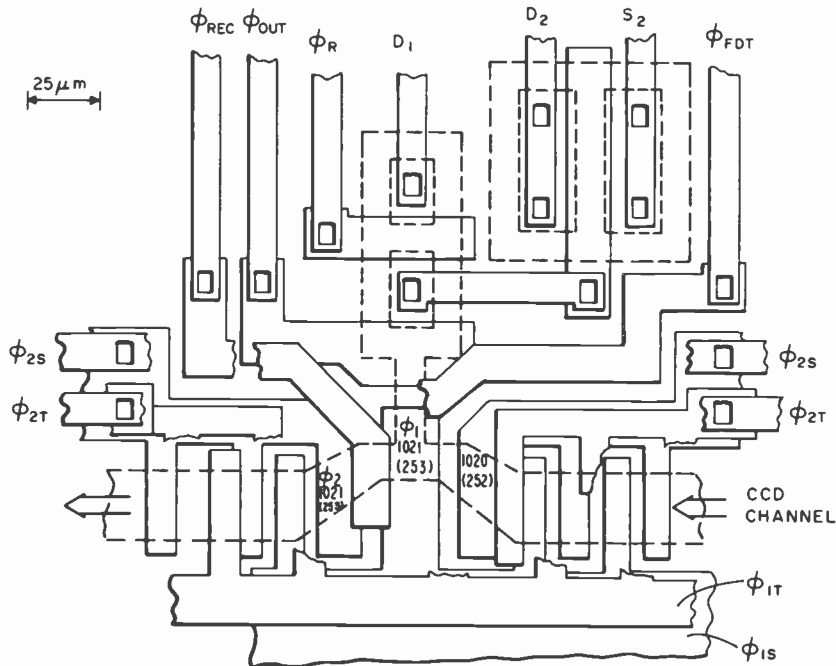

Fig. 8—Layout of the floating-diffusion output stage.

2.2.5 Dark-Current Subtraction Stage

Each loop is constructed with a dark-current subtraction stage, as shown in Fig. 9. The operation of this stage, which can be adjusted to remove a fixed amount of charge from the loop, will be described in Sec. 2.5. This stage can also be operated as a proportional charge subtractor and in this mode of operation will allow a removal of 25% of charge from the signal-charge packets and/or the trailing bias-charge packets. Operation of the dark-current subtraction stage as a proportional subtractor has not been tested, however, and will not be discussed in this paper.

2.3 Operation of Low-Loss CCD

The low-loss CCD concept is based on operating a CCD register in such a way that each signal-charge well is followed by at least one trailing well. The function of the trailing well (or wells) is to collect the charge left behind during each transfer of the signal-charge packet. Periodically, i.e., after a given number of transfers, the charge collected by the trailing

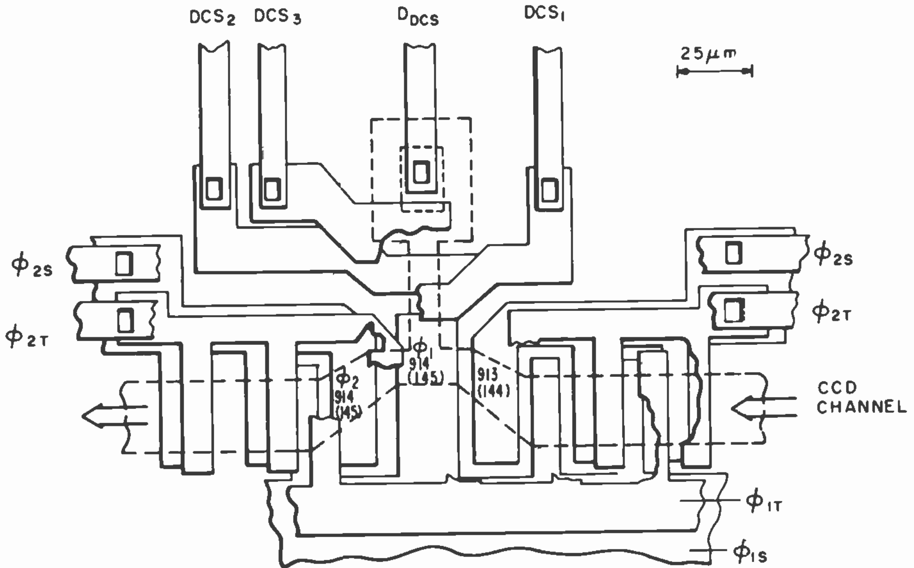

Fig. 9—Layout of the dark-current subtraction stage.

wells is recombined with the corresponding charge-signal packet at a low-loss signal-regeneration stage. Therefore, a low-loss CCD with one trailing well following each signal-charge well will recover the first-order transfer losses, i.e., the losses of the first-loss trailer of a conventional CCD register.

The relatively constant transfer losses in surface-channel and buried-channel CCDs at the intermediate and low clock frequencies are attributed to the "edge-effect" type of charge trapping.[5-9] Therefore, to achieve the best performance, the trailing wells should contain a large bias charge (fat zero) that is adjusted to be larger than the maximum charge in the signal wells. Such a large bias charge placed in the trailing wells between each signal well is expected to have maximum effect in maintaining the trapping states of the CCD channel filled and, hence, of minimizing the edge-effect losses. It should be noted that the charge left behind in each transfer of the large bias charge will be practically the same at each stage. Therefore, such steady-state transfer loss of the large trailing bias charge will not appear as the transfer loss of the signal, but rather as a small shift of the signal-bias-charge level. At this point we should also add that, for optimum performance, the signal wells should also contain a certain amount of bias charge in addition to the signal charge.

The operation of the low-loss signal-regeneration stage consists of first recombining the signal charge with its respective trailing bias charge and then separating the signal from a regenerated (reshaped) trailing bias charge. Therefore, the effective transfer losses of a low-loss CCD operating with one trailing bias charge are due to the second-order trapping losses resulting from the modulation of the trailing bias charge by the first-order trapping losses of the signal charge. For further discussion of the nature of the effective transfer losses of a low-loss CCD see the analysis by D. J. Sauer.[10]

2.4 Low-Loss Signal Regeneration

The construction and operation of a low-loss signal-regeneration stage is illustrated in Figs. 10 and 11. The charge-coupling structure of the signal-regeneration stage is shown schematically in Fig. 10(a) in the form of a two-phase CCD. The transfer of the charge packets in and out of the signal-regeneration stage is illustrated in Fig. 10(b) by means of channel potential profiles at time instants (t_1, t_2, t_3, t_4, t_5, and t_1') which are indicated on the clock waveforms shown in Fig. 11. To explain the operation of the low-loss signal-regeneration stage, we will focus our attention on the transfers of signal charge S_1 and its trailing bias charge (fat zero) T_1. The signal-regeneration stage first combines the signal

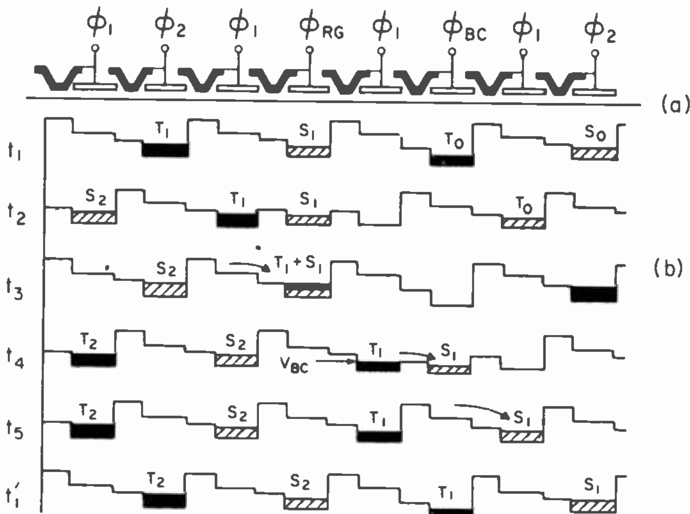

Fig. 10—Low-loss CCD: (a) charge-coupling structure; (b) potential wells illustrating the operation.

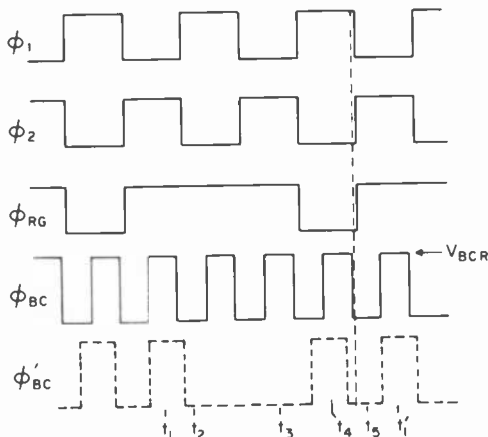

Fig. 11—Clock waveforms for operation of the low-loss CCD shown in Fig. 10.

charge S_1 with the contents of the trailing well, which in addition to the trailing bias charge T_1, also contains the first-order transfer losses. Then, one clock cycle later the regenerated signal S_1 is separated from its trailing bias charge T_1. To accomplish the above functions two additional clocks, ϕ_{RG} and ϕ_{BC}, are required. The clock ϕ_{RG} delays the signal charge S_1 by one clock cycle, i.e., from time t_1 to t_3. Because of this delay at time t_3, the signal charge S_1 is combined with the trailing bias charge T_1 and the first-order transfer losses contained in the trailing well. At time t_4, the combined charge ($S_1 + T_1$) is transferred to the adjacent potential well induced by clock ϕ_1. Note, however, that the adjacent CCD well is pulsed by a double-frequency bias-charge generating clock ϕ_{BC}. The result is that at time t_4 the signal charge, S_1, is skimmed by the potential barrier formed under the transfer gate and stored in the storage well formed by ϕ_{BC}. Then at time t_5 the signal S_1 is advanced forward to an empty well powered by the adjacent ϕ_1 clock. The function of the clock ϕ_{BC} is to establish a transfer barrier V_{BC} which leaves a regenerated trailing bias charge in the well induced by the clock ϕ_1. The beginning of the next cycle of the signal-regeneration stage is illustrated at time t_1'.

In general, the signal-regeneration stage described delays the signal, S_1, at time t_3 by one clock cycle. This delay results in combination of the signal S_1 with its trailing bias charge T_1. Also, at the same time, an empty well is generated at the following stage. The signal S_1 is advanced by one cycle (at times t_4 and t_5) by the double frequency trailing-bias-generating clock ϕ_{BC} (see Fig. 11) and transferred into this empty well. The same

basic operation can also be obtained by using a slower clock ϕ_{BC}', as shown in Fig. 11. The ϕ_{BC}' clock may be preferable for operation of the low-loss CCD at higher clock frequencies.

Referring to the channel potential profiles in Fig. 10(b), we see that the signal charge S_1 is always followed by the trailing bias charge T_1, except during two transfers when S_1 and T_1 are together in a single well (at the transfer at t_3 and a subsequent transfer before t_4). Another charge transfer that results in a second-order transfer loss is the transfer at time t_4 which separates the trailing bias charge T_1 and the signal charge S_1. This transfer is referred to as an incomplete (or bucket-brigade type) charge transfer.[5,11] To assure higher charge-transfer efficiency at this point, the transfer gate powered by ϕ_{BCT} and generating the barrier potential V_{BC} was designed longer (10 μm long) as shown in Fig. 6. Experimental results, however, showed that even with the above modification, we have about 0.7% charge transfer loss at this transfer. This transfer loss was reduced to 0.1% by an externally modified clock ϕ_{BC} so that skimming of the signal charge (as shown at t_4 in Fig. 10(b)) and dumping it into the next empty well (as shown at time t_5 in Fig. 10(b)) is repeated twice: the first time, to transfer most of the charge Q_{S1}, and the second to measure-off the trailing bias charge with an approximately empty storage well under the clock ϕ_{BC}. The results of this test are described in Sec. 3.4.3.

2.5 Dark-Current Subtraction

The construction and operation of the dark-current subtraction stage are illustrated in Fig. 12. Fig. 12(a) is a cross-sectional view showing one gate of a CCD register (G_{1S}) and three gates of the dark-current subtraction stage. Operation of the dark-current subtraction stage is illustrated by the channel potential profiles shown in Figs. 12(b), (c), and (d). In (b), the charge signal introduced into the storage gate G_{1S} of the CCD register spills over into the potential well under the gate G_{DSC2}. In (c), the charge signal is spilled back into the potential well under the gate G_{1S} while a small, fixed amount of charge Q_{DC} is left behind in the potential well under the gate G_{DCS2}. Finally, in Fig. 12(d), the charge subtracted from the CCD channel, Q_{DC}, is spilled to the drain V_{DD}. This operation can be accomplished at the same time the signal charge is transferred out from the well under the gate G_{1S}.

Assuming that the same type of surface channel is constructed under all the gates in Fig. 12(a), the charge Q_{DC} removed by the above process is

$$Q_{DC} = C_{DCS2}(V_{DCS2} - V_{DCS1}), \qquad [1]$$

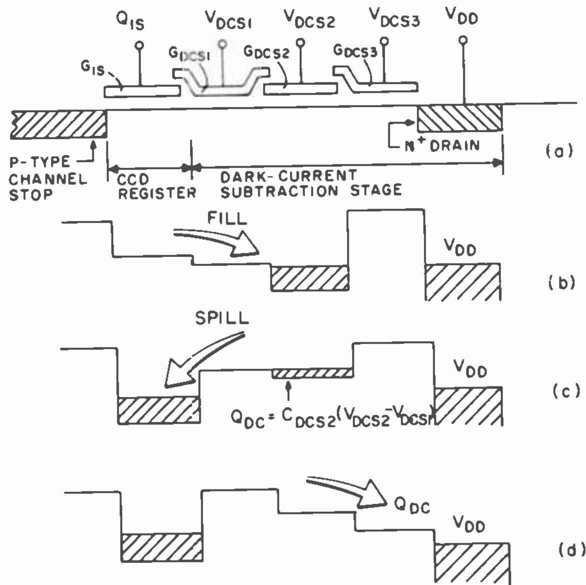

Fig. 12—Construction (a) and operation (b, c, d) of the dark-current subtraction stage.

where C_{DCS2} is the capacitance of the gate G_{DCS2}. For a buried-channel CCD, C_{DCS2} will represent an effective capacitance associated with the gate G_{DCS2}. The only requirement of the above charge-scooping operation is that the charge Q_{DC} be constant and independent of the signal-charge magnitude. Also, for any given long CCD delay line, the magnitude of the charge Q_{DC} to be removed from the CCD structure should be controlled by a self-adjusting feedback circuit. This was done in the operation of the closed-loop CCD devices, described in Sec. 3.

Since the dark-current subtraction stage removes a fixed amount of charge from a CCD structure, it can suppress the effect of the dark current on the reduction of the charge-handling capability of the CCD wells. But, it is not expected to remove the shot noise generated by the dark current. In fact, the process of the dark-current subtraction will also introduce a kTC noise.[12]

Let us assume that the full-well signal charge in a buried-channel CCD corresponds to 10^6 charge carriers and has $s/n = 5 \times 10^3$. Now, if this CCD is operated with 10 dark-current subtraction stages, each removing 10% of full well of dark-current generated charge, the total generated dark-current charge will correspond to 10^6 charge carriers. The resulting rms noise will be

$$N_{rms} = \sqrt{10^6} = 10^3, \quad [2]$$

and the s/n will be decreased to

$$s/n = 10^3. \quad [3]$$

Now, let us assume that the time delay is increased 100 times by operating the above CCD as a closed-loop structure with 100 signal recirculations. The resulting shot noise introduced by the dark current should be increased to

$$N_{rms} = \sqrt{10^8} = 10^4, \quad [4]$$

and the s/n should be decreased to

$$s/n = 100. \quad [5]$$

The above analysis, however, does not include the reduction in the noise due to the time-dependent bandwidth limited operation because of the transfer losses in the operation of the low-loss CCD with very many transfers. Our experimental results (see Sec. 3.4) show that when the closed-loop CCD is operated with the dark-current subtraction in the loop, adjusted to remove the thermally generated dark current, the shot noise due to the dark current does not increase progressively but rather tends to saturate at a relatively low value. The result is that the closed-loop CCD structure can be operated continuously with a closed loop without developing appreciable dark-current noise (see Section 3.4 for more discussion of this effect).

2.6 Clock Waveforms for Operation of the Closed-Loop CCDs

The clock generator for operation of the 256-stage and the 1024-stage closed-loop low-loss CCDs was designed to operate with a provision to adjust the number of loop cycles for recirculation of the signal in the loop. In the initial LOOP CYCLE 0 the signal is introduced into the loop, then the signal is recirculated in a closed loop for N-1 cycles. Finally in the LOOP CYCLE N, the loop is opened and the signal is removed from the loop via the floating diffusion output stage.

A simplified timing diagram for operation of the 256-stage CCD loop is shown in Fig. 13. The CCD clock frequency f_c is divided down to provide a LOOP SIZE signal ($f_c/2^9$) whose pulse width corresponds to the length of the CCD loop (256 clock cycles), and a TOTAL DELAY signal ($f_c/2^{11}$) whose period determines the overall test cycle time. The leading edge of the TOTAL DELAY signal initiates Loop Cycle N during which ϕ_{FDT} is pulsed for 256 clock cycles, which reads out all of the charge stored in the CCD loop via the floating-diffusion output stage.

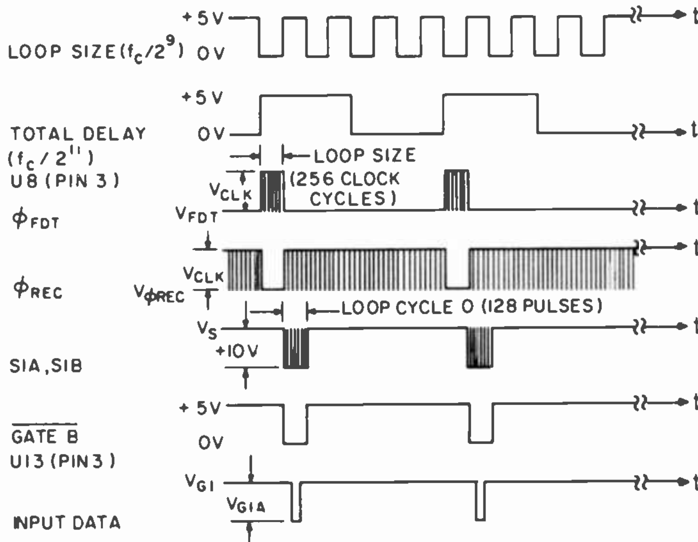

Fig. 13—Simplified timing diagram for the 256-stage closed-loop CCD.

This period is followed by Loop Cycle 0, during which new signals are introduced into the CCD register at the dual-channel input stage and charge is recirculated by pulsing ϕ_{REC}.

Fig. 14 is a timing diagram for the 256- and 1024-stage, closed-loop CCDs operating in the low-loss mode. A more detailed timing diagram for Loop Cycle 0 is shown in Fig. 15. The input signal is applied to gate G_{1A}. In the timing diagrams, a data input pattern of 0110 is used. Note that a '1' level corresponds to a more negative level on the input gate G_{1A}, and the negative S_{1A} strobe pulses occur when ϕ_1 is off. The S_{1A} pulses occur during even clock cycle times, and S_{1B} pulses (for introducing trailing bias charge in the second input channel) occur at odd clock cycle times. A total of 128 S_{1A} and 128 S_{1B} pulses occur during Loop Cycle 0. At the beginning of Loop Cycle 1, the S_{1A},S_{1B} pulses are inhibited and no further charge is introduced to the CCD via the dual-channel input stage.

At the beginning of Loop Cycle 0, the transfer out of the floating-diffusion stage ends by terminating the ϕ_{FDT} pulses, and the recirculation mode is started by initiating the ϕ_{REC} pulses. In the 256-stage loop, the first signal S_1 appears at the floating-gate output #1 during clock time 136 in each loop cycle, and the bias charge trailing behind signal S_1 appears at clock time 137 as shown in Fig. 14.

During Loop Cycle N the signals are transferred to the floating-dif-

Fig. 14—Timing diagram for the 256- and 1024-stage closed-loop CCDs.

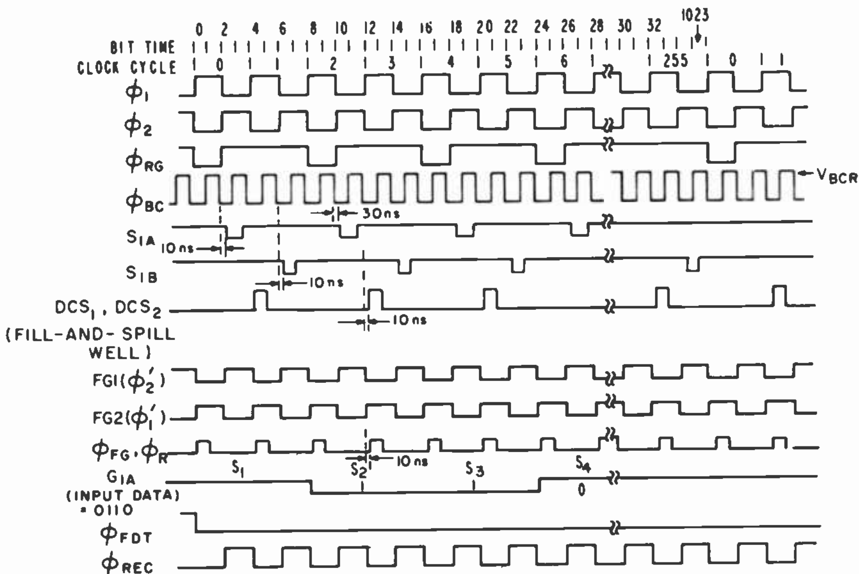

Fig. 15—Detailed timing diagram of loop cycle in Fig. 14

fusion output by applying pulses to ϕ_{FDT} and inhibiting ϕ_{REC}. The first signal to appear at the floating-diffusion output (during clock time 0) is S_2. Signal S_1 appears during clock time 254 after signal S_{128} at the end of the data stream. This reordering of data is due to a two-stage differential delay between the input stage to the merged input junction and the floating-diffusion output stage to the merged input junction.

The timing for operation of the 1024-stage CCD loop is very similar to that for the 256-stage CCD loop and is also shown in Fig. 14. In this case, a total of 512 signals are stored in the low-loss mode of operation.

3. Experimental Data

3.1 Typical Operating Waveforms

The actual clock waveforms used in the operation of the 256-stage and the 1024-stage closed-loop low-loss CCDs are illustrated in Fig. 16. The most critically controlled waveform was the bias-charge generating clock ϕ_{BC}. The rise-time of this clock was adjusted to guarantee no overshoot. The upper clock frequency of the clock waveform generator used in these experiments was f_c = 2.2 MHz.

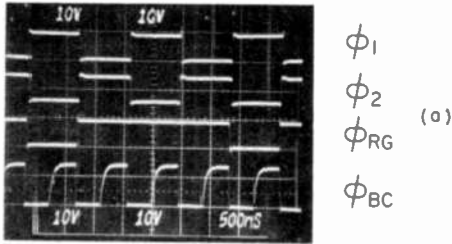

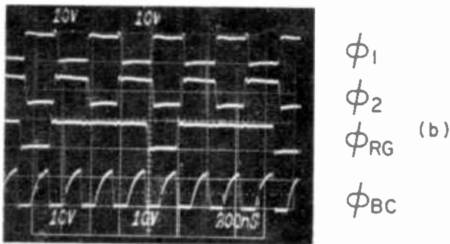

Fig. 16—Pulser waveforms for clock frequency of (a) 0.55 MHz, and (b) 2.2 MHz.

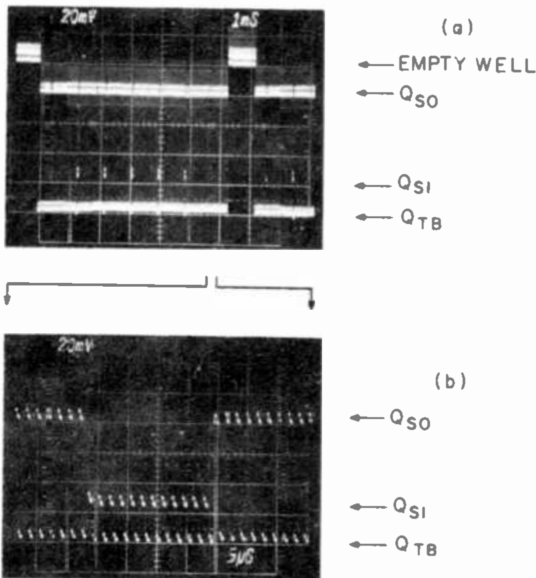

Fig. 17—Output waveforms for 1024-stage closed-loop CCD operating in low-loss CCD mode at (a) f_c = 1.1 MHz with seven recirculations, and (b) an expanded output signal after 14096 transfers.

Typical oscilloscope pictures of the output of the 1024-stage closed-loop low-loss CCD detected at the nondestructive floating-gate are shown in Fig. 17. Part (a) shows the detected output for seven recirculations of the signal followed by dumping of the signal charge out of the loop via the floating-diffusion output. Part (b) shows an expanded view of the detected signal after 14096 transfers in the loop. The detected signals in Fig. 17 consist of "one" signal-charge level Q_{S1}, "zero" signal-charge level Q_{S1}, and the trailing-bias-charge level Q_{TB}.

3.2 Input/Output Transfer Characteristics

The input transfer curve shown in Fig. 18 illustrates the calibration and the linearity of the dual input stage of the 1024-stage or the 256-stage closed-loop CCD. This curve was obtained by operating the input stage (one channel) in the standard charge preset (fill-and-spill) mode[5] with a dc bias applied to the gate G_2 and the input voltage, V_{G1}, applied to gate G_{1A}.

Typical floating-gate output characteristics measured for two different 1024-stage closed-loop low-loss CCDs (TC 1230A) are shown in Fig. 19. In this test we compare the signal charge, Q_s, with the observed oscilloscope waveform of the floating-gate output. Here, as well as in the case in Fig. 18, Q_s was measured by an electrometer. An inspection of Fig. 19 shows that the floating-gate output stage has a linear output transfer curve.

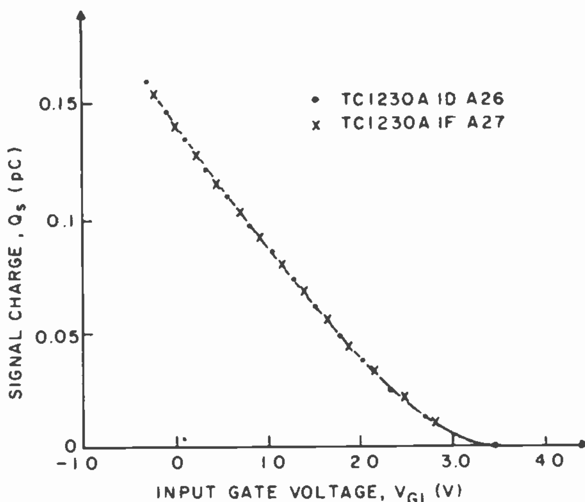

Fig. 18—CCD input transfer characteristics.

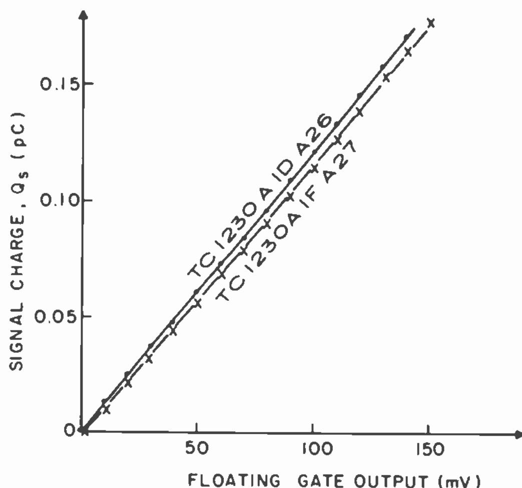

Fig. 19—Floating-gate output characteristics.

3.3 Transfer Losses for Standard Two-Phase CCD Mode

The measured transfer loss as a function of clock frequency, f_c, of a 256-stage closed-loop CCD operating in a standard two-phase CCD mode is shown in Fig. 20. This data was obtained for closed-loop operation with 20% of full-well bias charge (fat zero) and illustrates the first-order (standard) transfer losses as a function of clock frequency due to the

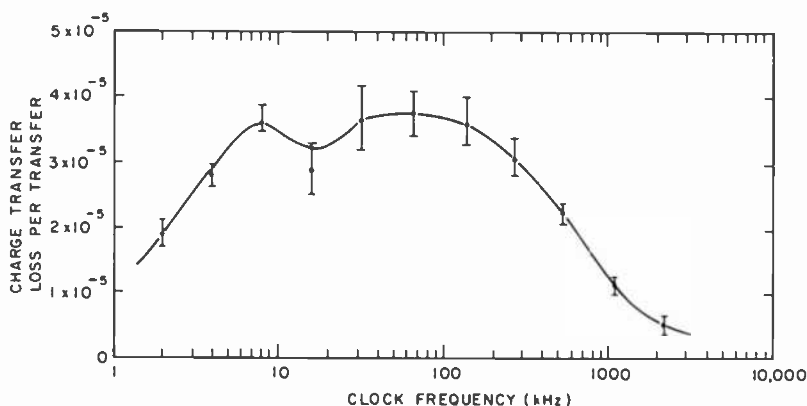

Fig. 20—Transfer loss for closed-loop 256-stage CCD operating with a standard two-phase clock and 20% bias charge (fat zero) as function of clock frequency.

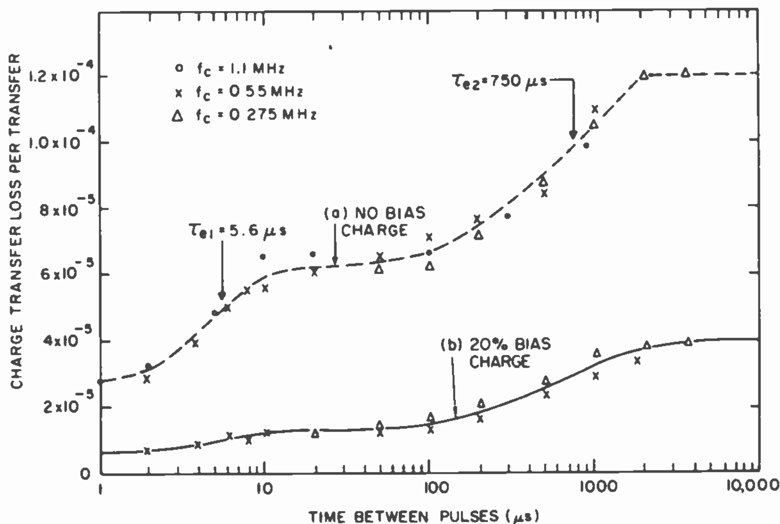

Fig. 21—Transfer loss of the leading-edge signal charge in the double-pulse trapping-loss test for 1024-stage open-loop CCD operating with standard two-phase clock and with (a) no bias charge (fat zero), and (b) 20% bias charge.

trapping of charge by bulk states present in buried-channel CCDs. A more quantitative characterization of the charge-trapping losses due to the bulk-trapping states is presented in Fig. 21. The curves show the transfer loss of a leading signal "one" in a string of "ones" as a function of time between the string of ones for operation with no bias charge and with 20% bias charge. This type of double-pulse test can be used to identify the emission times and calculate the densities of bulk traps in a BCCD.[9] Our data suggest the presence of two traps with the following densities and emission times:

$$N_{t1} = 3.6 \times 10^{11}\ \text{cm}^{-3}$$

$$\tau_{el} = 5.6\ \mu\text{s}$$

and

$$N_{t2} = 3.6 \times 10^{11}\ \text{cm}^{-3}$$

$$\tau_{e2} = 750\ \mu\text{s}.$$

The transfer loss measurements for the data in Fig. 21 were obtained by the operation of our 1024-stage device as an open-loop standard two-phase CCD. A typical output waveform observed during this double-pulse test is shown in Fig. 22.

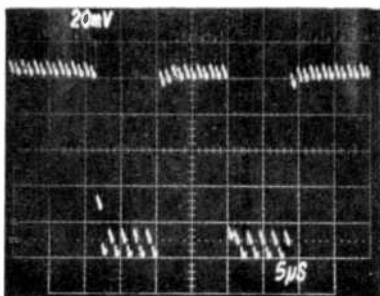

Fig. 22—Typical output waveform for double-pulse test of trapping losses after 1808 transfers of open-loop 1024-stage CCD operating with standard two-phase clock f_c = 1.1 MHz.

3.4 Transfer Losses for Low-Loss Mode of Operation

3.4.1 Performance of Closed-Loop Low-Loss CCDs

The performance of the 256-stage closed-loop low-loss CCD is illustrated by the waveforms shown in Fig. 23. As demonstrated by this figure we

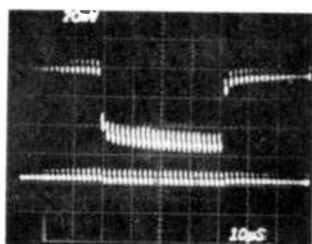

(a)

τ_D = 0.5 s
N = 1.1 x 10^6
ϵ = 2.4 x 10^{-7}

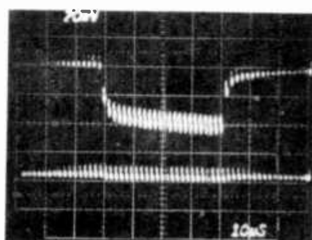

(b)

τ_D = 1.0 s
N = 2.2 x 10^6
ϵ = 2.6 x 10^{-7}

Fig. 23—Output waveforms of closed-loop low-loss 256-stage CCD at f_c = 1.0 MHz for initial values of Q_{S0} = 20 mV, Q_{S1} = 80 mV, and Q_{TB} = 100 mV.

have achieved an effective transfer loss of 2.5×10^{-7} per transfer. We define the effective transfer loss of the low-loss CCD as the transfer loss of the leading edge of an input pulse (the first "one" in a string of "ones"). The effective low-loss CCD transfer loss is

$$\epsilon_2 = \frac{\Delta Q_{S1}(1)}{N(Q_{S1} - Q_{S0})}, \quad [6]$$

where $\Delta Q_{S1}(1)$ is the difference between the initial value of the "one" at the input (i.e., as detected in the first recirculation) and the first "one" after N transfers, Q_{S1} is the amplitude of the signal charge "one," and Q_{S0} is the signal charge "zero." For the waveform in Fig. 23 we have used typical signal levels with $Q_{S0} = 0.2\ Q_{TB}$ and $Q_{S1} = 0.8\ Q_{TB}$, where Q_{TB} is the trailing bias charge adjusted just below the full well of the BCCD.

The waveforms shown in Fig. 23 indicate that the transfer losses obtained in the low-loss CCD are about two orders of magnitude lower than the transfer losses of the same device operating in the standard two-phase CCD mode. Furthermore, the transfer losses of the low-loss CCD are qualitative different from the standard CCD losses. First, the low-loss CCD losses appear to be symmetrical between the leading and the trailing edge of a signal pulse, i.e., about the same transfer loss is observed for the first "one" following a string of "zeros" as for the first "zero" following a string of "ones." Secondly, when a pulse input is used, the detected output after a large number of transfers (i.e., N on the order of 10^6) tends to have a long rise time that is some function of the emission times of the bulk traps. A similar time constant is also present at the trailing edge of the pulse. The effect of the long time constant on the output waveforms is illustrated in Fig. 24. Here, we show two output waveforms of a 1024-stage closed-loop low-loss CCD in the double-pulse test at clock frequency of (a) 1.1 MHz, and (b) 140 kHz. As shown in (a), a short pulse with a total delay time, τ_D, of 0.2 s exhibits a transfer loss at the leading edge in combination with some attenuation. However, a long signal pulse after a time delay of 3 s exhibits a rise time that is directly related to the time delay between the two signal pulses. The larger transfer loss at the leading edge of the first pulse is due to approximately one loop delay time between the second pulses and the first pulse. In connection with the long rise time obtained in the output of the low-loss CCD after a large number of transfers, we would like to point out that a short output pulse will appear at the output attenuated with an apparent transfer loss that is smaller than determined by Eq. [6].

It is also interesting to note that the signal charge used in this test is

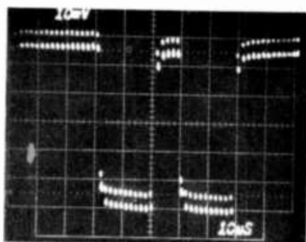

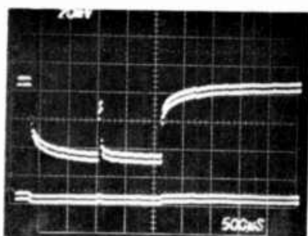

Fig. 24—Output waveforms for double-pulse test of trapping losses in closed-loop low-loss 1024-stage CCD.

$Q_{S1} - Q_{S0} = 0.12$ pC, which corresponds to about 0.8×10^6 electrons. This means that while in the standard CCD mode the transfer loss of 1.6×10^{-5} per transfer corresponds to an average charge trapping of 13 electrons, in the low-loss CCD mode the transfer loss of 2.5×10^{-7} per transfer corresponds to an effective average charge trapping of 0.2 electrons per transfer.

3.4.2 Effect of Bias Charge

The operation of a 1024-stage closed-loop CCD in the low-loss mode and the effect of bias charge on the transfer losses are illustrated in Fig. 25. Parts (a) and (b) compare the detected signal for $Q_{S0}/Q_{TB} = 0.2$ after 1808 transfers with the detected signal after 4.4×10^5 transfers, from which a transfer loss of 5.7×10^{-7} per transfer is estimated. Comparison of (c) and (d) shows the improvement in the transfer loss from 2.8×10^{-7} to 2.4×10^{-7} as Q_{S0}/Q_{TB} is increased from 0.4 to 0.6. Then in (e) we show the operation with $Q_{S0}/Q_{TB} = 0.8$ in a negative input signal pulse, or $Q_{S1}/Q_{TB} = 0.2$. In this case the transfer loss is 2.8×10^{-7} per transfer. Finally, the comparison of (c) with (f) shows the change in the pulse signal as the number of transfers, N, is increased from 4.4×10^5 to 2 ×

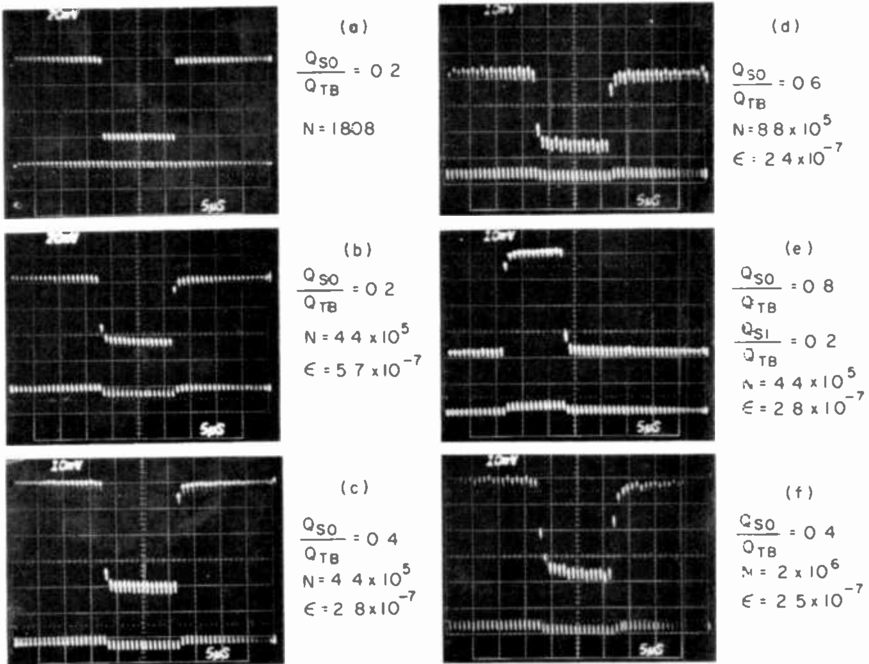

Fig. 25—Comparison of transfer loss, ϵ, of closed-loop low-loss 1024-stage CCD at f_c = 2.2 MHz for various "zero" signal charge levels, Q_{S0}, and number of transfers, N.

10^6. The general conclusion of the above test is that signal bias charge $Q_{S0} = 0.4Q_{TB}$ is sufficient to achieve the minimum transfer losses. Also, the transfer loss for negative signal pulse in the presence of large Q_{S0} is lower but still comparable to the transfer loss for positive signal pulse.

3.4.3 Optimization of the Low-Loss Signal Regenerator

Our study of the operation of low-loss CCD loops indicates that the effective transfer losses are associated with a second-order trapping of charge by the bulk states from the trailing bias charge. The magnitude of the trailing bias charges is slowly modulated by the first-order trapping losses of the signal charge. The second-order trapping loss involves only the amount of trailing bias charge, Q_{TB1}, following the "one" signal charge, Q_{S1}, that is larger than the preceding trailing bias charge, Q_{TB0}. In other words, the second-order trapping loss is due only to the charge difference,

$$\Delta Q_{TB} = Q_{TB1} - Q_{TB0}. \qquad [7]$$

In view of the above transfer loss mechanism for the low-loss CCD (described in more detail by D. J. Sauer[10]), it is important that the trailing bias charge regenerated periodically at the low-loss signal regenerator be constant and independent of the signal-charge magnitude. Our study of the operation of the regenerated trailing bias charge indicated that the incomplete charge transfer taking place when the signal charge is separated from the regenerated trailing bias charge (see Fig. 10(b) at t_4) produced a first-order transfer loss of about 7×10^{-3}. We observed this effect initially by comparing the trailing-bias-charge waveform detected by floating-gate amplifier No. 1 with the waveform detected by the floating-gate amplifier No. 2. Assuming a first-order charge-trapping loss of $\epsilon_1 = 3 \times 10^{-5}$ the second-order trapping loss will be $\epsilon_{2R} = 7 \times 10^{-3} \times 3 \times 10^{-5} = 2.1 \times 10^{-7}$ per transfer.

To reduce this second-order trapping loss we have modified the operation of the signal regenerator so that this incomplete transfer is ac-

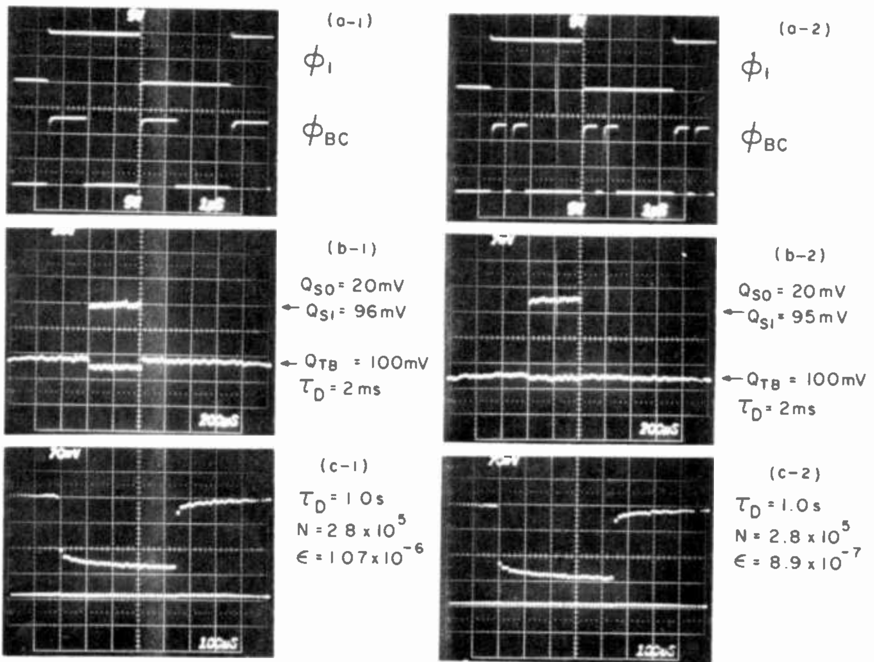

Fig. 26—Comparison of the operation of a closed-loop low-loss 1024-stage CCD at f_c = 4 kHz using the original ϕ_{BC} clock (in the left side of the figure) and the double ϕ_{BC} clock (in the right side of the figure).

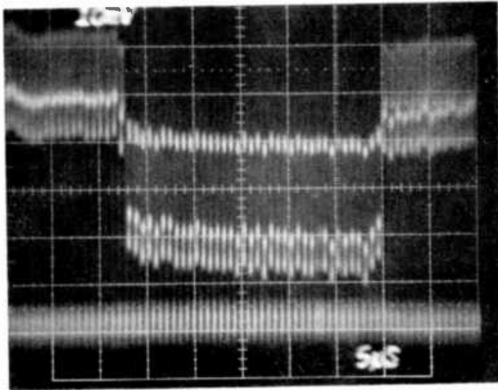

f_C = 2.8 MHz

τ_D = 1.0 s

N = 5.6 x 10^6

ϵ = 4.5 x 10^{-8}

Fig. 27—Operation of closed-loop low-loss 1024-stage CCD with feed-forward-compensated signal regeneration.

complished by a double ϕ_{BC} clock in two steps. First, the major part of the signal is transferred forward to the adjacent empty well and then the final level of the trailing bias is established with very small signal in the receiving wall. The operation of a 1024-stage closed-loop low-loss CCD with the original and the double clock ϕ_{BC} is illustrated on the left and the right side of Fig. 26. The two types of bias-charge generating clocks are shown in Fig. 26 (a-1) and (a-2). Fig. 26 (b-1) and (b-2) show the step in the trailing bias charge, Q_{TB}, due to the signal charge Q_{S1}. For the original ϕ_{BC} clock in (b-1) $\Delta Q_{TB}/(Q_{S1} - Q_{S0}) = 7 \times 10^{-3}$. For the double ϕ_{BC} clock, $\Delta Q_{TB}/(Q_{S1} - Q_{S0}) = 10^{-3}$. The actual transfer losses measured after 2.8×10^5 transfers can be compared between (c-1) and (c-2) as 1.07×10^{-6} for the original case and 8.9×10^{-7} for the operation with the double-pulse ϕ_{BC} clock. Note, the differential decrease of the transfer loss is 1.8×10^{-7} as compared to 2.1×10^{-7} based on our estimate for $\epsilon_{2R} = 7 \times 10^{-3} \times 3 \times 10^{-5} = 2.1 \times 10^{-7}$. The generally larger transfer loss, in the range of 10^{-6}, is typical of an operation at a low clock frequency of 4 kHz.

Since the effective transfer loss of the low-loss CCD is due to the second-order charge trapping of the trailing bias modulated by the signal charge, an experiment was performed whereby the signal detected at floating-gate amplifier No. 1. preceding the signal regenerator, was delayed by the proper amount to adjust the level of the trailing bias charge in an (adjustable) inverse direction to the signal charge. The result of this experiment with feed-forward-compensated signal regeneration is illustrated in Fig. 27, where an effective transfer loss of 4.5×10^{-8} per transfer was achieved.

3.4.4 Comparison of Calculated and Measured Charge-Transfer of the Low-Loss CCD

The analysis of D. J. Sauer[10] predicts the second-order charge-transfer loss, ϵ_2, of the low-loss CCD mode in terms of the measured first-order charge-transfer losses, ϵ_{LE} and ϵ_{TE}, of the same device operated in the conventional CCD mode. For n charge transfers between the low-loss signal regeneration stages, the average second-order low-loss CCD transfer loss is

$$\epsilon_2 = \frac{n+1}{2} \epsilon_{LE}\epsilon_{TE}, \quad [9]$$

where ϵ_{LE} is the leading-edge charge-transfer loss measured as the fractional decrease of the first "one" signal following a number of "zero" (bias-charge level) signals, and ϵ_{TE} is the trailing-edge charge-transfer loss measured as the increase of the first "zero" following a string of "ones". The charge-transfer loss of a low-loss CCD predicted by Eq. [9] is associated with the second-order trapping of charge by the bulk states in the BCCD channel due to the difference in the trailing bias charge associated with "ones" and "zeros."

There are additional charge-transfer losses at the low-loss signal regenerator that may become appreciable depending on the number of transfers, n, between signal regenerations. Included here are the first-order leading-edge charge-trapping losses at two transfers of the signal charge, S_1, combined with the trailing bias charge, T_1, as shown in Fig. 10. The corresponding effective first-order charge-transfer loss for n transfers between signal regenerations is

$$\epsilon_{1R} = \frac{2\epsilon_{LE}}{n}. \quad [10]$$

An additional second-order transfer loss, ϵ_{2R}, is introduced at the signal regenerator when the signal S_1 is separated from the trailing bias T_1 as shown in Fig. 10(a) at t_4. At this point, an incomplete (bucket-brigade type)[5,11] charge transfer takes place when the signal charge is skimmed from the trailing bias charge. The resulting first-order transfer loss, ϵ_{BB}, is produced when a normal ϕ_{BC} clock is used.* The modulation of the trailing-bias-charge level by the signal charge due to this incomplete transfer of charge produces an average second-order charge-transfer loss of

* This incomplete charge-transfer loss, ϵ_{BB}, can be minimized by using the double ϕ_{BC} clock described in Sec. 3.4.3 and Fig. 26 or by replacing the transfer gate powered by ϕ_{BC} clock (see Fig. 10) by two gates with a dc offset.

$$\epsilon_{2R} = \epsilon_{LE}\epsilon_{BB}. \quad [11]$$

Finally, the total charge-transfer loss of a low-loss CCD with n transfers between signal regenerations is

$$\epsilon_{TOT} = \epsilon_{LE}\left(\frac{n+1}{2}\epsilon_{TE} + \frac{2}{n} + \epsilon_{BB}\right). \quad [12]$$

The following first-order charge-transfer losses were measured on a 256-stage closed-loop CCD operating with standard two-phase clock at 1.1 MHz:

$$\epsilon_{LE} = 2.1 \times 10^{-5}$$

$$\epsilon_{TE} = 1.0 \times 10^{-5}$$

$$\epsilon_{BB} = 7 \times 10^{-7}$$

Substituting the above values in Eq. [12] with $n = 512$ charge transfers results in a calculated effective low-loss CCD charge-transfer loss of

$$\epsilon_{TOT\text{-}CALCULATED} = 2.9 \times 10^{-7} \text{ per transfer,}$$

as compared with a directly measured value of

$$\epsilon_{TOT\text{-}MEASURED} = 2.4 \times 10^{-7} \text{ per transfer.}$$

3.5 Dark-Current Subtraction

3.5.1 Variation of the Dark Current With the Signal Charge

One of the possible limitations of the effectiveness of the dark-current subtractor is that if the dark current is signal-dependent, the operation with a periodic subtraction of a fixed amount of dark current will lead to some form of nonlinear signal degradation of the output. To verify this we have made a test in which a closed CCD was operated with certain constant levels of signal charge while the dark-current subtractor was adjusted to remove the excess signal. In this test, the subtracted charge, which was measured by an electrometer as a drain current, I_{DCS}, was equal to the thermally generated dark current. The measured curves for two 1024-stage devices of the drain-current, I_{DCS}, representing the average thermally generated dark current as a function of the signal charge, Q_S, are shown in Fig. 28. These tests indicate that in our buried-channel CCDs there is a large range of signal for which the dark current is relatively constant.

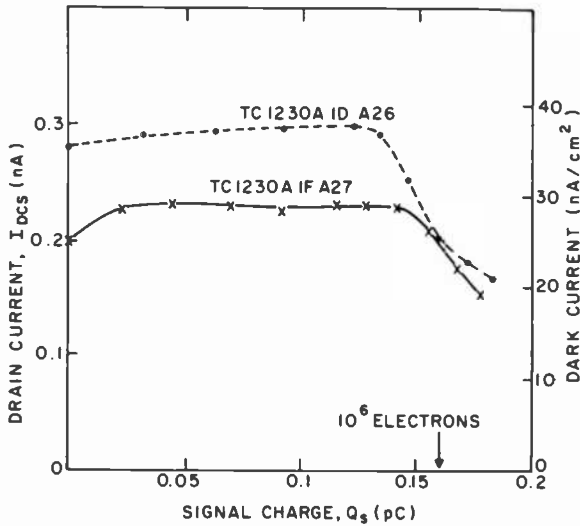

Fig. 28—Variation of dark current with signal charge level.

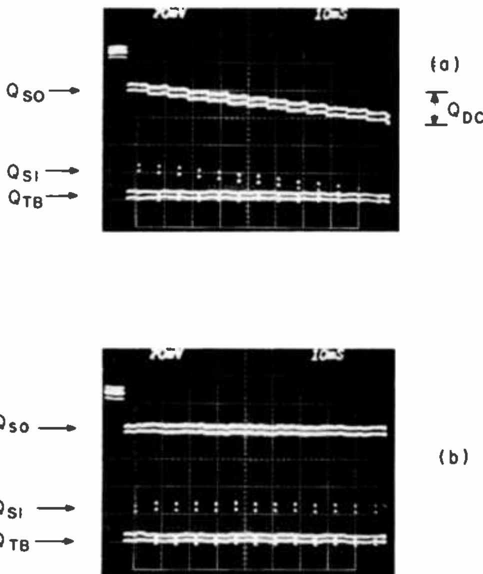

Fig. 29—Operation of the closed-loop low-loss 1024-stage CCD at f_c = 140 kHz (a) with dark-current subtractor OFF and (b) with dark-current subtractor ON.

3.5.2 Performance of the Dark-Current Subtractor

The operation of the dark-current subtractor is illustrated in Figs. 29, 30, and 31. In Fig. 29 we compare the operation of a 1024-stage closed-loop low-loss CCD without subtracting the dark current in (a) and with dark-current subtraction in (b). This comparison is made again in Fig. 30, but with only the signal bias charge, Q_{S0}, and the trailing bias charge, Q_{TB}, introduced in the loop. As we see in Fig. 30(a), the signal bias charge, Q_{S0}, increases to the level of the trailing bias charge, Q_{TB}, (which is periodically regenerated) in about 0.4 s. Then, in about 0.7 s, Q_{S0} reaches a full well and starts spilling into the trailing bias charge. The operation of the closed-loop low-loss CCD is shown in Fig. 30(b) with the dark-current subtractor adjusted to remove the excess thermally generated current. Now, we observe no accumulation of dark current for a total delay time of the signal in the closed loop of 7.5 s.

In Fig. 31, the performance of the closed-loop CCD operating in the standard CCD mode with transfer loss of 5.4×10^{-5} per transfer and a delay time, τ_D, of 0.5 s is compared with the low-loss operation with the

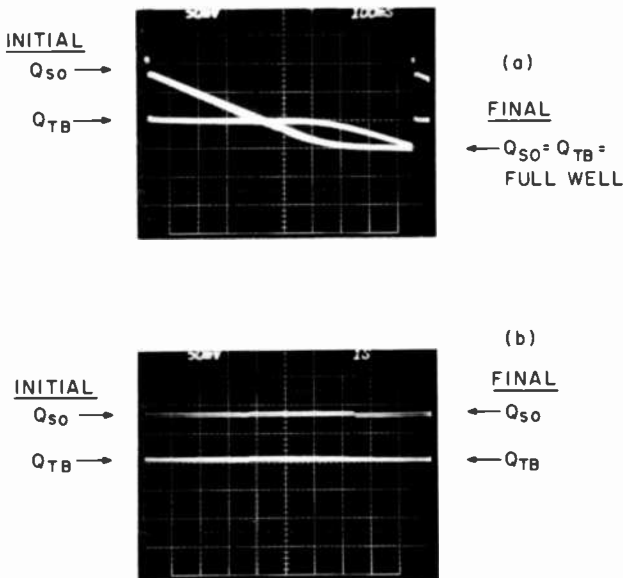

Fig. 30—Waveforms of zero-level signal, Q_{S0}, and trailing bias charge, Q_{TB}, in closed-loop low-loss 1024-stage CCD at f_c = 140 kHz: (a) for dark-current subtractor OFF and total delay time τ_D = 0.925 s and (b) for dark-current subtractor ON and τ_D = 7.4 s.

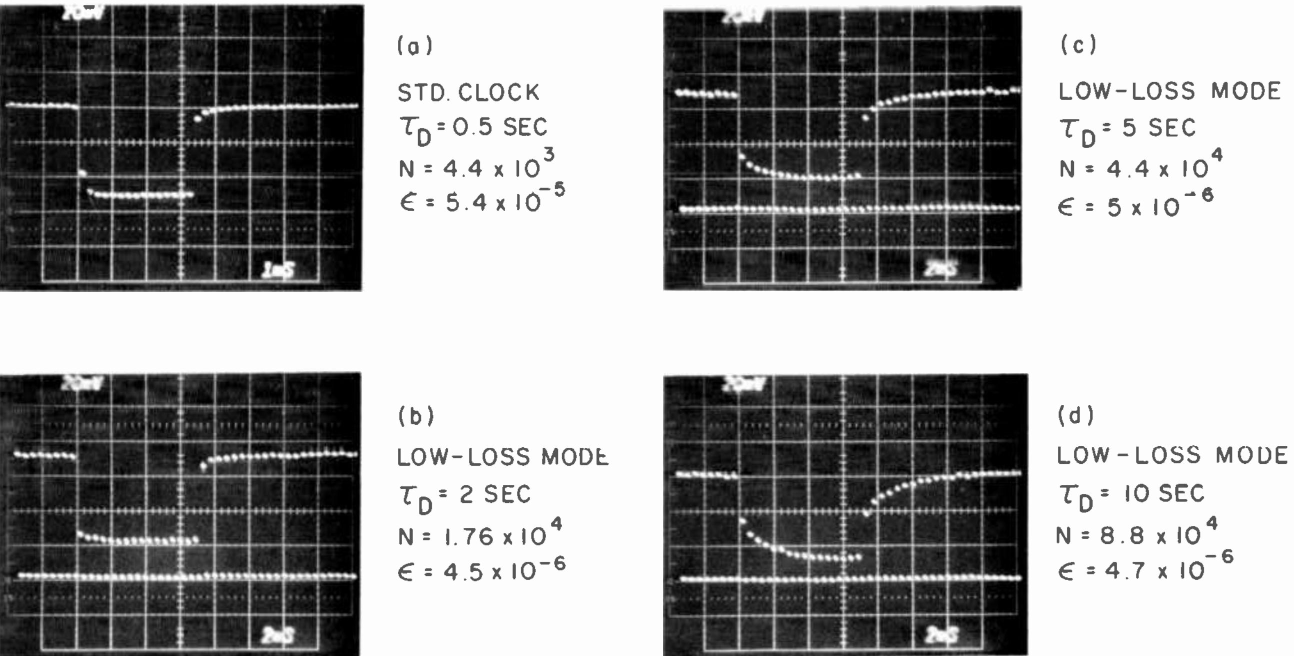

Fig. 31—Performance of closed-loop 256-stage CCD at f_c = 4.4 kHz with the dark-current subtractor ON with standard two-phase clock mode in (a) and low-loss mode in (b), (c), and (d).

delay time, during which the signal is being recirculated in the loop, progressively increased from 2 s, to 5 s, and finally to 10 s. The waveform in Fig. 31 demonstrates that a signal can be recirculated for up to 10 s with the dark-current subtractor in the loop. The only limitation on how long the signal can be delayed or recirculated is not imposed by the dark current but by the transfer losses, which tend to be larger at lower clock frequencies. As indicated in the next section, the shot noise introduced into the CCD by the dark current does not seem to accumulate appreciably.

3.5.3 Noise Introduced by the Dark Current

One of the more surprising results of our test of the closed-loop low-loss CCDs is that we have found that, with the dark-current subtractor in the loop, the dark-current shot noise does not seem to accumulate. This is demonstrated in Fig. 32. Here, the signal is in the form of a constant bias charge, Q_{SO}. The photograph in Fig. 32(a) shows the detected waveform during the first recirculation of the signal where we observe a peak-to-peak noise level of $V'_{(p\text{-}p)} = 0.8$ mV, or $V'_{rms} = 0.13$ mV. For

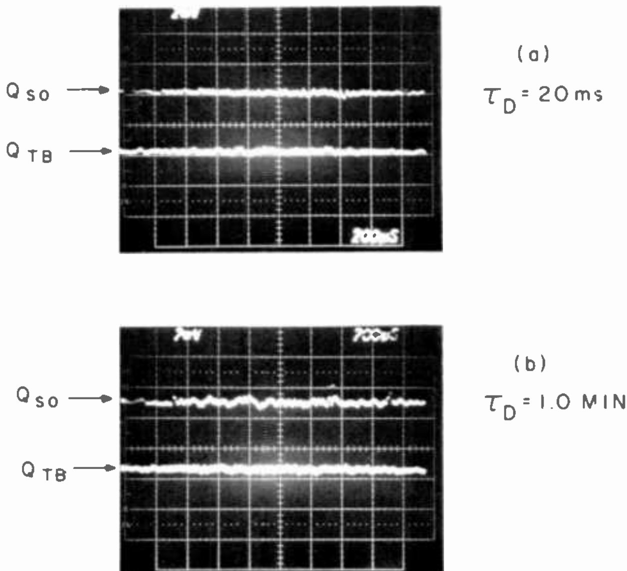

Fig. 32—Amplified output waveforms of $Q_{SO} = 95$ mV and $Q_{TB} = 100$ mV for closed-loop low-loss 256-stage CCD at $f_c = 140$ kHz, showing (a) the initial noise level and (b) the steady-state noise level (after a delay time $\tau_D = 1.0$ min).

Q_{S0} = 95 mV, we estimate the initial s/n_{rms} = 57 dB. Then in Fig. 32(b), after a recirculation delay time of 1.0 min, the value of $V''_{(p-p)} \approx 1.2$ mV and the final s/n_{rms} = 54 dB. Since a full well of charge is generated in this device in about 0.5 s, in 1.0 min 120 full wells of dark-current charge are generated. A full well corresponds to 100 mV, 0.12 pC, or 7.5×10^5 electrons. Thus, the expected shot noise due to the full well of dark current is 9400 electrons. However, the rms noise in Fig. 32(a) of $V'_{N(rms)}$ = 0.13 mV corresponds to N'_{rms} = 975 electrons. Then, after a delay time of 1.0 min with 120 full wells of dark current subtracted, the measured noise corresponds to $V''_{N(p-p)}$ = 1.2 mV, $V''_{N(rms)}$ = 0.2 mV, or N''_{rms} = 1500 electrons. Assuming that in Fig. 32(a) all the noise is due to the output amplifier, then in Fig. 32(b),

$$\sqrt{N^2_{amplifier} + N^2_{dark\ current}} = 1500,$$

or $N_{dark\ current}$ = 1133 electrons, corresponding to the effective number of rms noise electrons due to the dark-current generation of 120 full wells of charge.

The above number should be compared to the calculated rms noise of 9400 electrons corresponding to 120 full wells of dark current. The reduction of the dark-current noise may be attributed to the signal correlation between adjacent charge packets due to the charge transfer losses. This means that while the shot noise due to the dark current will saturate due to the signal averaging effect caused by the transfer losses, we cannot also maintain a signal in the loop indefinitely without dispersing it. There is, however, at least one application where we can use this effect. Namely, a continuously recirculating low-loss CCD loop with a proportional charge subtractor operating as a synchronous signal correlator. In this case the gain of the loop will be

$$A = \frac{1}{m}, \qquad [8]$$

where m is the fraction of charge removed from the loop by the proportional charge subtractor.

3.6 Synchronous Signal Correlator Experiment

In order to evaluate the performance of the closed-loop low-loss CCD in applications such as radar post-detection correlation, the 256-stage delay line was operated as a synchronous recirculating correlator with a continuous input. The input signal consisted of a repetitive pulse occurring at each loop cycle period (256 clock cycles) mixed with random noise. The power spectrum of this random noise is shown in Fig. 33. Continuous S_{1A} strobe pulses were applied to the CCD input stage, so

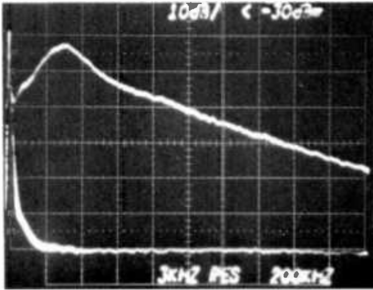

Fig. 33—Power spectrum of external random-noise generator with 3-kHz resolution (vertical scale: 10 dB/div.; horizontal scale: 200 kHz/div.).

that input signal charge was added continuously to the signal charge already recirculating in the loop; however, the trailing bias charges were only introduced once (during Loop Cycle 0). The input-signal bias level was adjusted to be about 10% of a full well, and then the dark-current subtractor was adjusted to subtract out this 10%, so that a steady-signal bias level of about 20% was maintained in the recirculating signal. (Note:

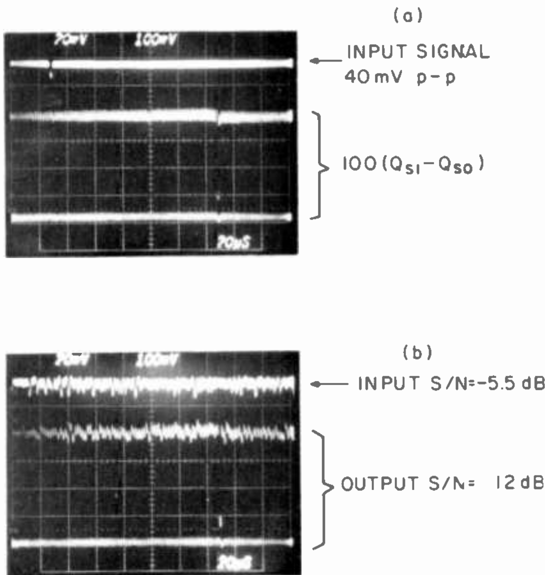

Fig. 34—Operation of the 256-stage closed-loop low-loss CCD at 1.1 MHz as a synchronous recirculating correlator with continuous input (top trace) showing the floating-gate output summation after 100 recirculations (bottom trace): (a) without noise at the input and (b) with noise added to the input signal.

This steady-signal bias level was determined by the signal-regeneration stage ϕ_{BC} skimming level.) The results of this experiment for 100 recirculations at a clock frequency of 1.1 MHz are shown in Fig. 34(a) for the case without random noise added to the input and in Fig. 34(b) for the case with random noise. The top trace in each oscillograph shows the input signal applied to G_{1A} and the bottom trace shows the output signal after 100 times around the CCD loop (total delay τ_D = 23 ms).

In the case of Fig. 34(b) the measured input $s/n = -5.5$ dB and the measured output $s/n = +12$ dB. Thus, using the closed-loop low-loss CCD as a synchronous recirculating correlator, we have demonstrated an improvement in the signal-to-noise ratio of +17.5 dB for 100 summations of the signal which is comparable to the theoretical limit of $\sqrt{100}$ = 20 dB.

4. Conclusions

To verify the proposed low-loss CCD concept,[1] we have developed 256-stage and 1024-stage closed-loop CCD structures that can be operated in the low-loss CCD mode by periodic signal regeneration. With these two devices operating in the low-loss CCD mode, we have demonstrated a reduction in the effective charge transfer losses by two orders of magnitude. While the typical transfer loss of our standard buried-channel CCD is about 2×10^{-5} per transfer, in the low-loss CCD mode we have achieved a transfer loss of 2.5×10^{-7} per transfer. In the case of the feed-forward-compensated signal regenerator we have observed a transfer loss as low as 4.5×10^{-8} per transfer.

We have demonstrated that, by operating the closed-loop low-loss CCDs with a dark-current subtractor in the loop, we can eliminate the effect of the dark current for very long delay times. We have stored a signal in the loop for up to 10 s, during which an estimated 20 full wells of thermally generated charge were subtracted from the loop. The noise generated by the dark current tends to saturate at a low level maintaining a s/n_{rms} = 54 dB independent of the recirculation time.

The closed-loop low-loss CCDs provide temporary storage for analog signals with nondestructive read-out. The low-loss CCD combined with the dark-current-subtraction technique should find applications in new CCD structures requiring a very large number of charge transfers (up to 10^6) and very long time delays (up to 10 minutes). One example of such applications is a synchronous signal correlator that was demonstrated using a 256-stage closed-loop low-loss CCD. With 100 signal recirculations we have obtained an improvement in the signal-to-noise ratio from −5.5 dB to 12 dB.

Acknowledgment

The authors wish to acknowledge the contributions of Dr. F. V. Shallcross and W. S. Romito for processing of the low-loss CCD arrays, Mrs. G. M. Meray for digitizing of the chip layout, and C. Y. Tayag for construction of the low-loss CCD tester.

References:

[1] W. F. Kosonocky and D. J. Sauer, U.S. Patent No. 4,134,028, "Charge Transfer Circuits with Compensation for Transfer Losses," Jan 9, 1979.

[2] T. F. Cheek, A. F. Tasch, J. B. Barton, S. P. Emmons, and J. E. Schroeder, "Design and Performance of Charge-Coupled Device Time-Division Analog Multiplexer," *Proc. 1973 CCD Applications Conf.*, San Diego, Calif., Sept. 18–20, 1973, pp. 127–139.

[3] R. C. Tozer and G. S. Hobson, "Reduction of High Level Nonlinear Smearing in CCDs," *Electron Lett.*, **12,** p. 355, July 8, 1976.

[4] J. Mavor and M. C. Davie, "Techniques for Increasing the Effective Charge-Transfer Efficiency of Tapped CCD Registers," *Electron. Lett.*, **13,** p. 31, Jan. 6, 1977.

[5] W. F. Kosonocky and J. E. Carnes, "Basic Concepts of Charge-Coupled Devices," *RCA Rev.*, **36,** p. 566 (1975).

[6] W. F. Kosonocky and J. E. Carnes, "Design and Performance of Two-Phase Charge-Coupled Devices with Overlapping Polysilicon and Aluminum Gates," Digest Tech. Papers, 1973 International Electron Device Meeting, Wash., D.C., p. 123, Dec. 3–5, 1973.

[7] C. H. Sequin and M. F. Tompsett, *Charge Transfer Devices*, Academic Press, New York, (1975), pp. 70–108.

[8] M. F. Tompsett, "The Quantitative Effects of Interface States on the Performance of Charge-Coupled Devices," *IEEE Trans. Electron Devices*, **ED-20,** p. 45 (1973).

[9] A. M. Mohsen and M. F. Tompsett, "The Effects of Bulk Traps on the Performance of Bulk Channel Charge-Coupled Devices," *IEEE Trans. Electron Devices*, **ED-21,** p. 701 (1974).

[10] D. J. Sauer, "Analysis of the Effective Transfer Losses in a Low-Loss CCD," *RCA Review*, **40,** p. 278, Sept. 1979 (this issue).

[11] W. F. Kosonocky and J. E. Carnes, "Two-Phase Charge-Coupled Devices with Overlapping Polysilicon and Aluminum Gates," *RCA Rev.*, **34,** p. 164 (1973).

[12] J. E. Carnes and W. F. Kosonocky, "Noise Sources in Charge-Coupled Devices," *RCA Rev.*, **33,** p. 327 (1972).

Analysis of the Effective Transfer Losses in a Low-Loss CCD

D. J. Sauer

RCA Laboratories, Princeton, N.J. 08540

Abstract—This article describes a model for the effective charge-transfer losses in a low-loss charge-coupled device (CCD). A low-loss CCD is operated with each signal-charge packet followed by one (or more) trailing-bias-charge packets of constant amplitude. The function of the trailing-bias charge is to keep the trapping states in the CCD channel filled, which greatly reduces the effective charge-transfer loss. The model is based on bulk-trapping losses present in a buried-channel CCD. With this model, the performance of a low-loss CCD may be predicted based on standard CCD measurements.

1. Introduction

The concept of a low-loss charge-coupled device that reduces the transfer losses in a CCD delay line by two orders of magnitude over those in a conventional buried-channel CCD has been experimentally verified, and is described in another article in this issue of RCA Review.[1] The low-loss CCD concept consists of operating a CCD with each signal-charge packet followed by one (or more) trailing-bias-charge packets of constant amplitude. The function of the trailing-bias charge is to keep the trapping states in the CCD channel filled. A very low effective transfer loss is realized by periodically recombining the charge-transfer losses collected by the trailing-bias-charge packets with the corresponding signal-charge packets at low-loss signal-regeneration stages. By setting the level of the trailing-bias-charge to be above the maximum signal-charge level, the effective transfer losses in a low-loss CCD are reduced to the second-

order trapping losses encountered by the trailing-bias-charge. These are due to the modulation of the trailing-bias-charge level by the first-order trapping losses experienced by the signal-charge packets.

Fig. 1 shows a block diagram of one section of a low-loss CCD delay line having $n/2$ CCD stages (which are capable of storing $n/4$ signals in the low-loss CCD mode of operation) located between two low-loss signal-regeneration stages. For the two-phase CCD illustrated there are n transfers in the CCD channel between the signal-regeneration stages. Each signal-charge packet (such as S_1) is followed by a corresponding trailing bias-charge packet (such as T_1) and both charges propagate to the right under the influence of the two CCD clock phases ϕ_1 and ϕ_2. The charge-coupling structure of the signal-regeneration stage is also shown schematically in Fig. 1 in the form of a two-phase overlapping-gate CCD. The location of charge packets S_0, T_0, S_1, and T_1 at a particlular time interval when ϕ_1 is OFF and ϕ_2 is ON is illustrated by the channel potential diagram under the gate structure.

The operation of the low-loss signal-regeneration stage[2] consists of first recombining the signal charge with its respective trailing bias charge, and then separating the signal from a regenerated (reshaped) trailing-bias charge that has a fixed level independent of the signal-charge level. Recombining the signal charge with its respective trailing-bias charge is accomplished by a special clock phase ϕ_{RG} which temporarily delays the signal charge by one clock period, so that the trailing-bias charge transfers into and combines with the signal charge in the CCD well formed under the ϕ_{RG} gate electrode. The signal portion of this combined charge is then "skimmed off" with another special clock pulse ϕ_{BC} leaving

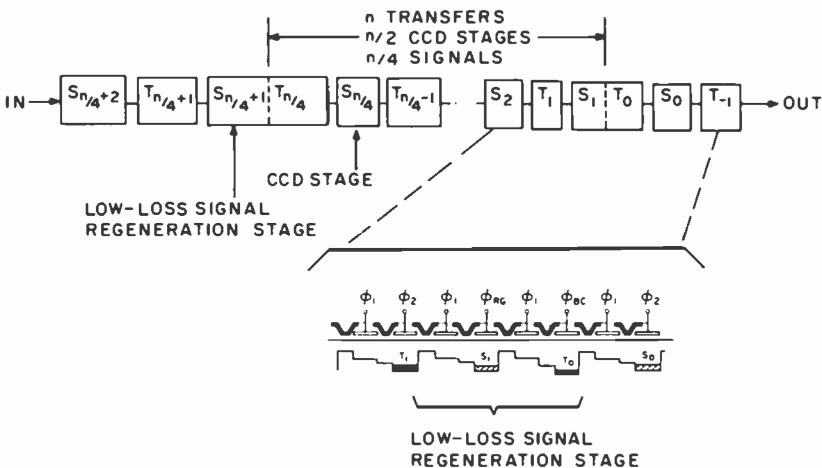

Fig. 1—Low-loss charge-coupled device.

the regenerated (fixed level) trailing-bias charge stored under the ϕ_1 gate electrode immediately preceding the ϕ_{BC} gate electrode. Due to the timing applied to the ϕ_{BC} pulse, the signal charge is pushed ahead by one CCD stage so that there is no net delay in the signal-regeneration stage for either the signal or its respective trailing-bias charge.

The analysis of the effective transfer losses in a low-loss CCD presented in this article was developed to predict the transfer-loss performance of a low-loss CCD from measurements made with standard CCD clocking.

In the discussion that follows, we make the following definitions:

e = electronic charge 1.6×10^{-19} C.
E = energy level of bulk trap below conduction band
ϵ_{BB} = bucket-brigade mode fractional charge-transfer loss
ϵ_{LE} = leading-edge fractional charge-transfer loss
ϵ_{TE} = trailing-edge fractional charge-transfer loss
ϵ_1 = first-order fractional charge-transfer loss
ϵ_2 = second-order fractional charge-transfer loss
k = Boltzmann's constant
n = number of transfers between signal regeneration stages
N_c = effective density of states in the conduction band (cm^{-3})
n_e = density of mobile electrons (C/cm^3)
N_t = density of bulk-trapping states (cm^{-3})
n_t = charge density of filled traps (C/cm^3)
q_t = total trapped charge (C)
Q_S = signal charge level (C)
Q_{TB} = trailing bias charge level (C)
Q_{S0} = signal charge 'zero' level (C)
Q_{S1} = signal charge 'one' level (C)
Q_{TB0} = trailing bias charge level following Q_{S0} (C)
Q_{TB1} = trailing bias charge level following Q_{S1} (C)
Q_{SUM} = sum charge packet $Q_S + Q_{TB}$
T_S = storage time (s)
T_T = transfer time (s)
T_c = clock period (s)
t' = free-charge transfer time (s)
τ_e = bulk state emission time constant (s)
τ_t = bulk state trapping time constant (s)
V_S = volume occupied by signal charge Q_S (cm^3)
V_{TB} = volume occupied by trailing bias charge Q_{TB} (cm^3)
v_{th} = average thermal velocity of electrons (cm/s)
σ = bulk-trap capture cross section (cm^2)

2. Simplified Analysis of the Effective Transfer Losses in a Low-Loss CCD

An expression for the effective (second-order) transfer losses for a CCD operating in the low-loss mode in terms of the first-order transfer losses of the same CCD operating with standard clocking is derived in this analysis. A more detailed analysis is presented in Sec. 3.

2.1 Assumptions Used in the Analysis

We assume that transfer losses in the low-loss buried-channel CCD (BCCD) are dominated by the trapping of charge in the bulk-trapping states, i.e., the device is operating at low-to-medium clock frequencies where free-charge transfer loss is not a significant factor. Furthermore, the low-loss CCD is operated with a large trailing bias charge, Q_{TB}, (close to a full well) placed in every other stage between the signal charge, Q_S. A repetitive signal is assumed to be present in the form of a long string of "zeros" with charge Q_{S0} followed by a single "one" with charge Q_{S1}. The signal charges, Q_{S0} and Q_{S1}, followed by their respective trailing bias charges, Q_{TB0} and Q_{TB1} transfer in succession into and then out of the same stage of the BCCD containing bulk-trapping states with a density N_t (cm^{-3}). A two-phase BCCD is assumed where each clock period T_c consists of a storage time T_s during which the charge is stored in the well and a transfer time T_T during which the charge is being transferred to the successive storage well. Let us assume further that the bulk-trapping states can be represented with a single trapping state having a density N_t (cm^{-3}), a trapping time constant τ_t, and an emission time constant τ_e. We will assume $\tau_t \ll T_s$ and $\tau_t \ll \tau_e$. This means that during the storage time, all of the charge-trapping states will be filled in the volume of the BCCD channel containing the signal charge, Q_{S1} or Q_{S0}, or the trailing bias charge, Q_{TB}.

2.2 First-Order Charge Transfer Loss

The trapping and emission of charge in the operation of the low-loss CCD is illustrated in Fig. 2. The repetitive signal shown here is in the form of a very long string of "zeros" with signal charge Q_{S0} followed by a single "one" with signal charge Q_{S1}. At the input stage of the CCD (or immediately following a signal-regeneration stage), the signal-charge levels Q_{S0} and Q_{S1} and trailing-bias-charge level Q_{TB} indicated by the dotted lines in Fig. 2 are present. The solid lines in Fig. 2 indicate the corresponding charge levels following a single transfer along the CCD register. Note that due to the first-order trapping losses the signal-charge levels

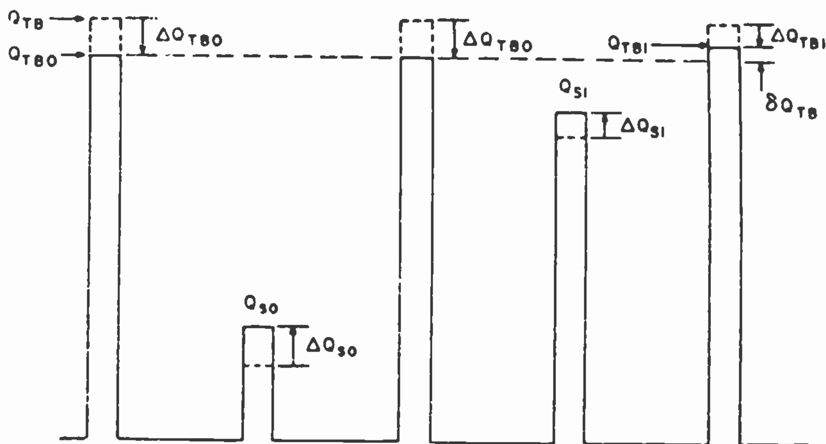

Fig. 2—Trapping and emission of charge in the operation of the low-loss CCD.

increase, and the trailing-bias-charge levels decrease correspondingly. We will now show that to first order $\Delta Q_{S0} = -\Delta Q_{TB0}$ so that in a low-loss CCD mode the net first-order loss for the sum charge packet $Q_{SUM} = Q_{S0} + Q_{TB0}$ is zero.

Our analysis is based on conservation of the total charge (mobile and trapped) in the BCCD. The net change in the total charge contained within a given volume V of the BCCD is equal to the difference between the charge Q (initial) transferred into V and the charge Q (final) transferred out of V. Just before Q (initial) enters, the BCCD well is essentially empty and contains only the trapped charge q_t (initial). Similarly, after Q (final) transfers out of the well, only the trapped charge q_t (final) is present. Therefore, we have:

$$\Delta Q \equiv Q \text{ (final)} - Q \text{ (initial)} = q_t \text{ (initial)} - q_t \text{ (final)}. \qquad [1]$$

For the transfer of the signal charge Q_{S0} and the trailing bias charge Q_{TB0}, Eq. [1] becomes

$$\Delta Q_{S0} = q_t^{S0} \text{ (initial)} - q_t^{S0}\text{(final)} \qquad [2]$$

and

$$\Delta Q_{TB0} = q_t^{TB0} \text{ (initial)} - q_t^{TB0} \text{ (final)}. \qquad [3]$$

Since the trapped charge q_t^{TB0} (initial) is the same as q_t^{S0} (final), the net change in the sum-charge packet Q_{SUM} is

$$\Delta Q_{SUM} = \Delta Q_{S0} + \Delta Q_{TB0} = q_t^{S0} \text{ (initial)} - q_t^{TB0} \text{ (final)}. \qquad [4]$$

Let us calculate how much charge q_t^{TB0} (final) is trapped in volume V_{TB0}

after the trailing bias charge Q_{TB0} transfers out of the BCCD well. During the storage time T_S all of the trapping states in volume V_{TB0} are filled, thus trapping a charge of eN_tV_{TB0} from Q_{TB0}. However, during the transfer time T_T, the BCCD is essentially empty and the trapped charges are re-emitted with a time constant τ_e and join Q_{TB0}. Thus, at the end of the transfer time the bulk trapping states contain the net trapped charge:

$$q_t^{TB0}\,(\text{final}) = eN_t V_{TB0} \exp\left\{\frac{-T_T}{\tau_e}\right\}. \quad [5]$$

It is important to note that since the trailing-bias-charge level Q_{TB0} is larger than any previous signal charges, the trapped charge q_t^{TB0} (final) given by Eq. [5] is independent of the preceding signals. Since the signal charge Q_{S0} is immediately preceded by another trailing bias charge Q_{TB0}, the initial trapped charge q_t^{S0}(initial) in Eq. [4] is also equal to q_t^{TB0} (final). Therefore, the net change in the sum charge packet due to first-order losses is zero:

$$\Delta Q_{SUM} = \Delta Q_{S0} + \Delta Q_{TB0} = 0. \quad [6]$$

Referring again to Fig. 2, the first-order charge transfer losses ΔQ_{S0} and ΔQ_{S1} may be calculated from the trailing-edge fractional charge transfer loss ϵ_{TE} as follows:

$$\Delta Q_{S0} = -\Delta Q_{TB0} = \epsilon_{TE}\,(Q_{TB0} - Q_{S0}) \quad [7]$$

and

$$\Delta Q_{S1} = -\Delta Q_{TB1} = \epsilon_{TE}\,(Q_{TB0} - Q_{S1}). \quad [8]$$

ϵ_{TE} is measured from the increase in the first "zero" signal following a string of "ones" when the CCD is operated with standard clocks and the "zero" signal bias level is on the order of Q_{S0}.

2.3 Second-Order Charge Transfer Loss

As we discussed in the previous section, during each transfer in a low-loss CCD, the signal charge increases by a small amount ΔQ_S and the trailing bias charge following the signal charge decreases by exactly the same amount. However, we see from Eqs. [7] and [8] that ΔQ_{S0} is larger than ΔQ_{S1} and, therefore, the trailing bias charge Q_{TB0} decreases more than the trailing bias charge Q_{TB1} during each transfer. This causes a step in the level of the trailing bias charge at each transfer which has the value

$$\delta Q_{TB} \equiv \Delta Q_{TB0} - \Delta Q_{TB1} = \epsilon_{TE}\,(Q_{S0} - Q_{S1}). \quad [9]$$

We now assume that the first-order losses are sufficiently low so that

δQ_{TB} is essentially constant and independent of the number of transfers i following a signal-regeneration stage. Therefore, at the ith transfer, the difference in the level of the trailing bias charge Q_{TB0} and Q_{TB1} will be

$$Q_{TB0} - Q_{TB1} = i\delta Q_{TB} = i\epsilon_{TE}\,(Q_{S0} - Q_{S1}). \qquad [10]$$

By following an analysis similar to that used to derive Eq. [4], we find that the change in the sum charge packet $\Delta Q_{SUM} = \Delta Q_{S1} + Q_{TB1}$ for a single "one" following a string of "zeros" is

$$\Delta Q_{SUM} = \Delta Q_{S1} + \Delta Q_{TB1} = q_t^{S1}\,(\text{initial}) - q_t^{TB1}\,(\text{final}). \qquad [11]$$

Since the signal charge Q_{S1} is immediately preceded by a trailing bias charge Q_{TB0}, the trapped charge q_t^{S1} (initial) is the same as q_t^{TB0} (final). Thus, Eq. [11] may be written as

$$\Delta Q_{SUM} = q_t^{TB0}\,(\text{final}) - q_t^{TB1}\,(\text{final}). \qquad [12]$$

The charge loss ΔQ_{SUM} in Eq. [12] has the same form as in the case of a CCD with standard clocks having a string of Q_{TB0} bias charges followed by a single Q_{TB1} charge which is slightly larger. This allows us to write ΔQ_{SUM} in terms of the leading-edge loss ϵ_{LE} (measured from the decrease in the first "one" signal following a string of "zeros" when the CCD is operated with standard clocks and the "zero" signal bias level is on the order of Q_{TB0}):

$$\Delta Q_{SUM} = \epsilon_{LE}\,(Q_{TB0} - Q_{TB1}). \qquad [13]$$

Substituting Eq. [10] into Eq. [13], we find that the second-order loss for the sum-charge packet during the ith transfer following a signal-regeneration stage is

$$\Delta Q_{SUM}(i) = i\epsilon_{LE}\epsilon_{TE}\,(Q_{S0} - Q_{S1}). \qquad [14]$$

Therefore, the average second-order fractional transfer loss for n transfers is

$$\epsilon_2 = \frac{\sum_{i=1}^{n} |\Delta Q_{SUM}(i)|}{n(Q_{S1} - Q_{S0})} \qquad [15]$$

or

$$\epsilon_2 = \frac{n+1}{2}\,\epsilon_{LE}\epsilon_{TE}. \qquad [16]$$

2.4 Optimum Number of Transfers Between Regeneration Stages

Since the signal charge and trailing bias charge are combined at the signal-regeneration stage in the low-loss CCD, the combined charge sees a first-order loss due to bulk-trapping during two transfers at this point. For a device having n transfers between signal-regeneration stages, the average charge transfer loss due to the first-order losses at the signal-regeneration stage is

$$\epsilon_{1R} = 2\,\epsilon_{LE}/n. \tag{17}$$

Adding Eqs. [16] and [17], we find that the total second-order charge transfer loss $\epsilon_{TOT} = \epsilon_{1R} + \epsilon_2$ is a function of n:

$$\epsilon_{TOT}(n) = \epsilon_{LE}\left(\frac{2}{n} + \frac{n+1}{2}\,\epsilon_{TE}\right). \tag{18}$$

It is evident from Eq. [18] that there is an optimum value, n_{OPT}, for the number of transfers between regeneration stages that will minimize the total transfer loss. Setting the derivative $d\epsilon_{TOT}/dn$ equal to zero, we find

$$n_{OPT} = 2/\sqrt{\epsilon_{TE}} \tag{19}$$

and, for $n \gg 1$,

$$\epsilon_{TOT}(\min) = \epsilon_{LE}\,(\sqrt{\epsilon_{TE}} + 1/\sqrt{\epsilon_{TE}}). \tag{20}$$

Typical values for n_{OPT} as a function of ϵ_{TE} are as follows:

ϵ_{TE}	n_{OPT}
1×10^{-4}	200
5×10^{-5}	282
2×10^{-5}	447
1×10^{-5}	632

2.5 Effect of Signal-Regenerator Performance on Second-Order Charge Transfer Loss

Our study of the operation of the signal-regeneration stage[3] indicates that the incomplete (bucket-brigade mode) charge transfer taking place when the signal charge is skimmed from the trailing bias charge produces a first-order loss $\epsilon_{BB} \approx 7 \times 10^{-3}$ when we use a normal ϕ_{BC} clock pulse. The resulting modulation of the trailing-bias-charge level by the signal charge causes an average second-order fractional charge transfer loss per transfer of

$$\epsilon_{2R} = \epsilon_{LE}\epsilon_{BB}. \tag{21}$$

Therefore, the total second-order charge transfer loss in this case is

$$\epsilon_{TOT} = \epsilon_{LE}\left(\frac{2}{n} + \frac{n+1}{2}\epsilon_{TE} + \epsilon_{BB}\right). \quad [22]$$

2.6 Sample Calculation

The following first-order charge transfer losses were measured[1] on a 256-stage closed-loop CCD operating with standard 2ϕ clocks at a frequency of 1.1 MHz:

$$\epsilon_{LE} = 2.1 \times 10^{-5}$$

$$\epsilon_{TE} = 1.0 \times 10^{-5}$$

$$\epsilon_{BB} = 7 \times 10^{-3}.$$

Substituting the above values into Eq. [22] yields a calculated value for the effective second-order charge transfer loss of $\epsilon_{TOT} = 2.9 \times 10^{-7}$, which compares to a measured value of $\epsilon = 2.4 \times 10^{-7}$ for the same device operating in the low-loss mode.

3. Detailed Analysis of the Effective Transfer Loss in a Low-Loss BCCD Due to Bulk-Trapping States

In this analysis we assume that the low-loss BCCD is operated with a trailing bias charge Q_{TB} that is larger than the signal charge Q_S in order to obtain minimum effective transfer losses. We also assume that the clock frequency f_c is below the point where free-charge transfer is a limiting factor, so that transfer losses are dominated by the interaction of Q_S and Q_{TB} with the bulk traps in the buried-channel region. Section 3.1 provides a brief review of the Schottky-Read-Hall rate equation describing bulk-trapping states. In Section 3.2, we derive equations for the first-order transfer loss of ΔQ_S and ΔQ_{TB} and show that although charge is redistributed between Q_S and Q_{TB} due to bulk-trapping, to first order, there is no net transfer loss for the sum-charge packet $Q_{SUM} = Q_S + Q_{TB}$. The analysis of the effective transfer loss for Q_{SUM} due to second-order transfer losses is presented in Section 3.3. In Section 3.4 we consider the effect of the interaction of multiple bulk traps having different energy levels. An expression for the second-order transfer loss with closed-loop operation is derived in Section 3.5. In Section 3.6, the charge-transfer losses due to the signal-regeneration stage are discussed, and a sample calculation based on measured data is shown in Section 3.7. The following analysis is based on the bulk trapping model for buried-channel CCDs described by Mohsen and Tompsett.[4]

3.1 Bulk-Trap Occupancy

The interaction of minority carriers in the BCCD charge packet with bulk traps is described by the Schottky-Read-Hall rate equation:

$$\frac{dn_t}{dt} = \frac{(N_t - n_t)}{\tau_t} - \frac{n_t}{\tau_e}, \qquad [23]$$

where the trapping time constant τ_t is

$$\tau_t = (\sigma v_{th} n_e)^{-1} \qquad [24]$$

and the emission time constant τ_e is

$$\tau_e = \left[\sigma v_{th} N_c \exp\left\{\frac{E}{kT}\right\}\right]^{-1} \qquad [25]$$

The equilibrium charge density of filled traps may be determined from Eq. [23] by setting $dn_t/dt = 0$. Solving for n_t, we obtain

$$n_t = \frac{eN_t}{1 + \frac{\tau_t}{\tau_e}}. \qquad [26]$$

The total trapped charge q_t in a volume V_S is given by

$$q_t = \int_{V_S} n_t \, dV. \qquad [27]$$

For most traps of importance, $\tau_t \ll \tau_e$, and if we assume n_t is essentially constant over the volume V_S, Eq. [27] reduces to

$$q_t = n_t V_S \approx e N_t V_S. \qquad [28]$$

3.2 First-Order Charge Transfer Loss Analysis

In general, the change ΔQ_S in a signal charge Q_S due to interaction with bulk traps during a single transfer can be determined by comparing the initial state of the traps q_t (initial) in the CCD well before the signal charge enters with the final state of the traps q_t (final) after the signal charge has transferred out of that region of the CCD. Since charge must be conserved, we have:

$$Q_S \text{ (initial)} + q_t \text{ (initial)} = Q_S \text{ (final)} + q_t \text{ (final)} \qquad [29]$$

or

$$\Delta Q_S = -\Delta q_t = q_t \text{ (initial)} - q_t \text{ (final)}. \qquad [30]$$

During the storage time T_S while the signal Q_S (which occupies volume

V_S) is present in the CCD well, the bulk traps contained in that volume are filled to a level of $q_t = n_t V_S$. During the initial short transfer time t' (when most of the charge transfers out of the well), the traps remain filled. However, during the remaining transfer time $T'_T = T_T - t'$, the BCCD is essentially empty and the trapped charges, which are emitted with a time constant τ_e, can join the signal charge. At the end of the transfer time, the trapping states contain the net trapped charge

$$q_t = n_t V_S \exp\left\{\frac{-T'_T}{\tau_e}\right\}. \quad [31]$$

We now consider the case of a low-loss CCD with an input data pattern containing a single 'one' signal charge Q_{S1} that is preceded by a string of 'zero' signal charges Q_{S0}. A trailing bias charge Q_{TB0} follows each signal charge Q_{S0}, and a trailing bias charge Q_{TB1} follows the signal charge Q_{S1}. (This analysis also applies to the leading 'one' signal charge of a string of 'ones'.) We will now calculate the first-order transfer losses ΔQ_{S0} and ΔQ_{TB0} per transfer and show that their sum ΔQ_{SUM} is identically equal to zero. (In Sec. 3.3 we calculate the first-order losses ΔQ_{S1} and ΔQ_{TB1}, in which case the sum $\Delta Q_{SUM} = \Delta Q_{S1} + \Delta Q_{TB1}$ is not equal to zero and exhibits a net second-order transfer loss.)

We begin the calculation of ΔQ_{S0} as follows:

$$\Delta Q_{S0} = q_t^{S0}\,(\text{initial}) - q_t^{S0}\,(\text{final}); \quad [32]$$

$$q_t^{S0}(\text{initial}) = n_t V_{TB0} \exp\left\{\frac{-T'_T}{\tau_e}\right\}; \quad [33]$$

$$q_t^{S0}(\text{final}) = n_t V_{S0} \exp\left\{\frac{-T'_T}{\tau_e}\right\} + n_t(V_{TB0} - V_{S0}) \exp\left\{\frac{-T'_T}{\tau_e}\right\} \times \exp\left\{\frac{-(T_S + T_T)}{\tau_e}\right\} \quad [34]$$

Note that Eq. 34 contains two terms. The first term is due to traps located in the center volume V_{S0} which remain filled during the storage time T_S and emit trapped charge only during the final transfer time $T'_T = T_T - t'$. The second term is due to the edge volume $V_{TB0} - V_{S0}$ which has an initial trap occupancy of $n_t(V_{TB0} - V_{S0}) \exp\{-T'_T/\tau_e\}$ and emits trapped charge during the entire period $T_S + T_T$. For convenience, we define,

$$r_1 = T'_T/\tau_e \text{ and } r_2 = (T_T + T_S)/\tau_e.$$

Substituting Eqs. [33] and [34] into Eq. [32], we have

$$\Delta Q_{S0} = n_t(V_{TB0} - V_{S0})e^{-r_1}(1 - e^{-r_2}). \quad [35]$$

In a similar fashion, we calculate ΔQ_{TB0} as

$$\Delta Q_{TB0} = q_t^{TB0}\,(\text{initial}) - q_t^{TB0}\,(\text{final}) \qquad [36]$$

where

$$q_t^{TB0}\,(\text{initial}) = q_t^{S0}(\text{final}) \qquad [37]$$

and

$$q_t^{TB0}(\text{final}) = n_t V_{TB0} e^{-r_1}. \qquad [38]$$

Thus

$$\Delta Q_{TB0} = -n_t (V_{TB0} - V_{S0}) e^{-r_1} (1 - e^{-r_2}). \qquad [39]$$

Comparing Eqs. [39] and Eq. [35], we see that there is no net change in the sum charge packet Q_{SUM} during the transfer,

$$\Delta Q_{SUM} = \Delta Q_{S0} + \Delta Q_{TB0} = 0. \qquad [40]$$

Therefore, during the transfer operation in a low-loss CCD, the signal charge increases by a small amount ΔQ_{S0} due to charge trapped from the preceding trailing bias charge near the edges, which is re-emitted into the signal charge. The trailing bias charge Q_{TB0} that follows the signal charge decreases by exactly the same amount $(-\Delta Q_{S0})$ because it refills the edge traps that emitted charge into Q_{S0}.

3.3 Second-Order Charge-Transfer Loss Analysis

In this section we calculate the first-order losses ΔQ_{S1} and ΔQ_{TB1}, which leads to the result that the sum-charge packet in this case $Q_{SUM} = Q_{S1} + Q_{TB1}$ does see a net second-order loss:

$$\Delta Q_{S1} = q_t^{S1}(\text{initial}) - q_t^{S1}(\text{final}); \qquad [41]$$

$$q_t^{S1}(\text{initial}) = n_t V_{TB0} e^{-r_1}; \qquad [42]$$

$$q_t^{S1}(\text{final}) = n_t V_{S1} e^{-r_1} + n_t (V_{TB0} - V_{S1}) e^{-r_1} e^{-r_2}; \qquad [43]$$

$$\Delta Q_{S1} = n_t (V_{TB0} - V_{S1}) e^{-r_1} (1 - e^{-r_2}). \qquad [44]$$

ΔQ_{TB1} is calculated following an analysis similar to the calculation for ΔQ_{TB0} as follows:

$$\Delta Q_{TB1} = q_t^{TB1}(\text{initial}) - q_t^{TB1}(\text{final}); \qquad [45]$$

$$q_t^{TB1}(\text{initial}) = n_t V_{S1} e^{-r_1} + n_t (V_{TB0} - V_{S1}) e^{-r_1} e^{-r_2} \qquad [46]$$

$$q_t^{TB1}\,(\text{final}) = n_t V_{TB1} e^{-r_1} \qquad [47]$$

$$\Delta Q_{TB1} = n_t (V_{S1} - V_{TB1}) e^{-r_1} + n_t (V_{TB0} - V_{S1}) e^{-r_1} e^{-r_2}. \qquad [48]$$

The change in the sum charge packet Q_{SUM} in this case is found by adding Eqs. [44] and [48]:

$$\Delta Q_{SUM} = \Delta Q_{S1} + \Delta Q_{TB1} = n_t e^{-r_1}(V_{TB0} - V_{TB1}). \quad [49]$$

The expression for ΔQ_{SUM} in Eq. [49] may also be derived in a simpler manner by noting that

$$\Delta Q_{SUM} = [q_t^{S1}(\text{initial}) - q_t^{S1}(\text{final}] + [q_t^{TB1}(\text{initial}) - q_t^{TB1}(\text{final})], \quad [50]$$

and, since $q_t^{S1}(\text{final}) = q_t^{TB1}(\text{initial})$, this reduces to

$$\Delta Q_{SUM} = q_t^{S1}(\text{initial}) - q_t^{TB1}(\text{final}). \quad [51]$$

In other words, ΔQ_{SUM} depends only on the initial state of the bulk traps before Q_{S1} enters the CCD well and the final state of the bulk traps after Q_{TB1} transfers out of the CCD well.

Immediately following a signal-regeneration stage in the low-loss CCD, Q_{TB0} and Q_{TB1} are exactly equal so that the term $V_{TB0} - V_{TB1}$ in Eq. [49] is negligible. During each subsequent charge transfer down the CCD delay line, the volumes V_{TB0} and V_{TB1} both decrease due to the first-order charge-transfer losses ΔQ_{TB0} and ΔQ_{TB1}, respectively. However, since Q_{TB0} is decreasing faster than Q_{TB1}, a charge difference $Q_{TB1} - Q_{TB0}$ builds up on the trailing-bias-charge level that is proportional to the number of transfers i following the regeneration stage. It is this charge difference $Q_{TB1} - Q_{TB0}$ that causes the nonzero second-order transfer loss ΔQ_{SUM} in Eq. [49], since a corresponding volume difference $V_{TB0} - V_{TB1}$ is present in the buried channel well.

In order to evaluate the term $V_{TB0} - V_{TB1}$, we assume that the volume occupied by mobile charge carriers is linearly proportional to the size of the charge packet, which is a good approximation for relatively large signals in a BCCD. Thus,

$$V_{TB0} - V_{TB1} = \frac{\partial V}{\partial Q}(Q_{TB0} - Q_{TB1}), \quad [52]$$

where $\partial V/\partial Q$ is the proportionality constant relating the volume to charge.

In general, during the ith transfer following a signal-regeneration stage, the magnitude of Q_{TB0} and Q_{TB1} is given by

$$Q_{TB0}(i) = Q_{TB0}(0) + \sum_{j=1}^{i-1} \Delta Q_{TB0}(j) \quad [53]$$

$$Q_{TB1}(i) = Q_{TB1}(0) + \sum_{j=1}^{i-1} \Delta Q_{TB1}(j) \quad [54]$$

where $Q_{TB0}(0) = Q_{TB1}(0) = Q_{TB}$ is the initial value of the trailing bias charge established in the signal-regeneration stage. Combining Eqs. [53] and [54] gives

$$Q_{TB0}(i) - Q_{TB1}(i) = \sum_{j=1}^{i-1} [\Delta Q_{TB0}(j) - \Delta Q_{TB1}(j)]. \quad [55]$$

The term $\delta Q_{TB} \equiv \Delta Q_{TB0} - \Delta Q_{TB1}$ can be evaluated by substituting from Eqs. [39] and [48] and rearranging terms to obtain

$$\Delta Q_{TB0} - \Delta Q_{TB1} = n_t e^{-r_1} \times [(V_{S0} - V_{S1} + V_{TB1} - V_{TB0}) + (V_{S1} - V_{S0})e^{-r_2}]. \quad [56]$$

We now make the assumption that the first-order losses are sufficiently low so that, for the purpose of evaluating Eq. [56], $(V_{TB1} - V_{TB0}) \ll (V_{S0} - V_{S1})$ and $V_{S0} - V_{S1}$ is independent of the number of transfers i. With this assumption, Eq. [56] becomes

$$\delta Q_{TB} \equiv \Delta Q_{TB0} - \Delta Q_{TB1} = n_t (V_{S0} - V_{S1}) e^{-r_1}(1 - e^{-r_2}). \quad [57]$$

Combining Eqs. [49], [52], [55], and [57] we obtain an expression for the second-order trapping loss during the ith transfer:

$$\Delta Q_{SUM}(i) = i n_t e^{-r_1} \frac{\partial V}{\partial Q} \delta Q_{TB}. \quad [58]$$

For a low-loss CCD which has n transfers between regeneration stages, the total second-order trapping loss ΔQ_{SUM}(tot) following n transfers can be expressed as

$$\Delta Q_{SUM}(tot) = \sum_{i=1}^{n} \Delta Q_{SUM}(i) = (1 + 2 + \ldots + n) n_t e^{-r_1} \times \frac{\partial V}{\partial Q} \delta Q_{TB}, \quad [59]$$

or

$$\Delta Q_{SUM}(tot) = \frac{n(n+1)}{2} n_t e^{-r_1} \frac{\partial V}{\partial Q} \delta Q_{TB}. \quad [60]$$

Finally, the average second-order fractional transfer loss $\epsilon_2 = \Delta Q_{SUM}(tot)/n(Q_{S1} - Q_{S0})$ is given by

$$\epsilon_2 = \frac{n+1}{2(Q_{S1} - Q_{S0})} n_t e^{-r_1} \frac{\partial V}{\partial Q} \delta Q_{TB}. \quad [61]$$

In view of the number of assumptions that were made to simplify the foregoing analysis, some of the factors that limit the accuracy of Eq. [61] should be considered. We have implicitly assumed that the trap occupancy n_t given by Eq. [26] is constant throughout the volume occupied by the charge packet. Actually, the value of n_t near the edges is lower since the free charge density n_e is lower at these points, which increases the trapping time constant τ_t. In addition, in the transfer regions of the CCD as the free charge sweeps by, there is a filling probability F for the bulk traps that also reduces the value of n_t in these regions. As a result,

the second-order transfer loss ϵ_2 given by Eq. [61] using a value $n_t = eN_t$ represents a 'worst case' value, which we have found to be typically about 2 times higher than experimentally measured values.

3.4 Interaction of Multiple Bulk-Trapping States

The analysis in Sec. 3.3 for the second-order trapping loss was based on a single bulk-trapping state model. In a buried-channel device with multiple bulk-trapping states, the interaction of these states must be considered to determine the second-order losses. For a device having m bulk-trapping states with energy levels E_1 to E_m, we can modify the expression for δQ_{TB} in Eq. [57] to

$$\delta Q_{TB} = (V_{S0} - V_{S1}) \sum_{E=E_1}^{E_m} n_t(E) \exp\left\{\frac{-T_T'}{\tau_e(E)}\right\} \times \left[1 - \exp\left\{\frac{-(T_T + T_S)}{\tau_e(E)}\right\}\right] \quad [62]$$

The fractional transfer loss given by Eq. [61] is modified according to:

$$\epsilon_2 = \frac{n+1}{2(Q_{S1} - Q_{S0})} \sum_{E=E_1}^{E_m} n_t(E) \exp\left\{\frac{-T_T'}{\tau_e(E)}\right\} \frac{\partial V}{\partial Q} \delta Q_{TB}. \quad [63]$$

3.5 Second-Order Transfer Loss for Closed-Loop Operation

When the low loss CCD is recirculating with a loop cycle time (i.e., total time around the closed loop) T_L that is comparable to a bulk-trap emission time constant τ_e, then the bulk traps in the edge volume $(V_{TB1} - V_{TB0})$ do not completely empty in the time T_L. As a result, less charge is trapped, and Eq. [49] must be modified to

$$\Delta Q_{SUM} = n_t \left[\exp\left\{\frac{-T_T'}{\tau_e}\right\} - \exp\left\{\frac{-T_L}{\tau_e}\right\}\right] (V_{TB0} - V_{TB1}). \quad [64]$$

Using this result in combination with multiple bulk-trapping states results in a second-order fractional transfer loss of

$$\epsilon_2 = \frac{n+1}{2(Q_{S1} - Q_{S0})} \sum_{E=E_1}^{E_m} n_t(E) \left[\exp\left\{\frac{-T_T'}{\tau_e}\right\} - \exp\left\{\frac{-T_L}{\tau_e}\right\}\right] \times \frac{\partial V}{\partial Q} \delta Q_{TB} \quad [65]$$

where δQ_{TB} is given by Eq. [62].

3.6 Charge-Transfer Losses Due to Signal-Regeneration Stage

As discussed in Sections 2.4 and 2.5, the signal-regeneration stage introduces the additional transfer losses ϵ_{1R} and ϵ_{2R} (see Eqs. [17] and [21]) which must be added to ϵ_2 to obtain the total second-order loss ϵ_{TOT}. The leading-edge transfer loss ϵ_{LE} used to calculate ϵ_{1R} and ϵ_{2R} may be expressed in terms of the bulk-trapping states as

$$\epsilon_{LE} = \sum_{E=E_1}^{E_m} n_t(E) \left[\exp\left\{-\frac{T'_T}{\tau_e(E)}\right\} - \exp\left\{-\frac{T_L}{\tau_e(E)}\right\}\right] \frac{\partial V}{\partial Q}. \qquad [66]$$

The trailing-edge transfer loss ϵ_{TE} may also be expressed as:

$$\epsilon_{TE} = \frac{\delta Q_{TB}}{Q_{S1} - Q_{S0}}, \qquad [67]$$

where δQ_{TB} is given by Eq. [62]. Therefore the total second-order charge transfer loss is given by (*cf.* Eq. [22])

$$\epsilon_{TOT} = \epsilon_{LE}\left(\frac{2}{n} + \frac{n+1}{2}\epsilon_{TE} + \epsilon_{BB}\right) \qquad [68]$$

where ϵ_{LE} is defined by Eq. [66], ϵ_{TE} is defined by Eq. [67], and ϵ_{BB} is measured as discussed in Sec. 2.5.

3.7 Sample Calculation

Our data[1] indicated the presence of two bulk-trapping states in the BCCD with the following densities and emission times:

$$n_t(E_1) = 5.8 \times 10^{-8} \text{C/cm}^3$$

$$\tau_e(E_1) = 5.6 \mu s$$

$$n_t(E_2) = 5.8 \times 10^{-8} \text{C/cm}^3$$

$$\tau_e(E_2) = 750 \mu s$$

For the case of a 256-stage closed-loop CCD operating at 1.1 MHz, the following parameters were measured:

$$Q_{S0} = 3.6 \times 10^{-14} \text{C}$$

$$Q_{S1} = 9.6 \times 10^{-14} \text{C}$$

$$T'_T = T_S = 0.45 \mu s$$

$$\epsilon_{BB} = 7 \times 10^{-3}$$

A value for $\partial V/\partial Q$ of 5×10^2 cm^3/C was estimated based on a buried-channel layer depth of 0.5 μm and a storage area of 25 μm × 10 μm.

Substituting these numbers into Eqs. [66], [67], and [68], we obtain the calculated values of $\epsilon_{LE} = 3.45 \times 10^{-5}$, $\epsilon_{TE} = 0.4 \times 10^{-5}$, and $\epsilon_{TOT} = 4.1 \times 10^{-7}$. The measured transfer loss for this device operating in the low-loss mode was 2.4×10^{-7}.

4. Summary

A model for the transfer-loss mechanisms in a low-loss CCD has been developed that may be used to predict the transfer-loss performance of a low-loss CCD from measurements of the leading-edge and trailing-edge fractional charge-transfer losses made using standard CCD clocking. The model is based on the interaction of the signal charge and trailing-bias charge with bulk-trapping states in the CCD channel. For a BCCD device that has a measured charge-transfer loss of $\sim 2 \times 10^{-5}$ when it is operated with standard CCD clocking, the typical calculated and measured charge-transfer loss in the low-loss mode of operation is $\sim 2 \times 10^{-7}$.

Acknowledgments

The author wishes to thank W. F. Kosonocky for his stimulating review and comments on this analysis which helped to formulate a clear understanding of transfer loss mechanisms in a low-loss CCD delay line. The initial CCD device testing performed by P. A. Levine, which demonstrated the validity of the low-loss CCD concept, is also greatly appreciated.

References

[1] W. F. Kosonocky and D. J. Sauer, "Low-Loss Charge-Coupled Device," *RCA Review*, **40**, p. 241, Sept. 1979.

[2] W. F. Kosonocky, D. J. Sauer, C. Y. Tayag, and F. V. Shallcross, "Low-Loss Charge-Coupled Device," Air Force Systems Command Contract No. F19628-77-C-0176, Final Report, RADC-TR-78-F, Dec. 1978.

[3] Ibid, pp 34–37.

[4] A. M. Mohsen and M. F. Tompsett, "The Effects of Bulk Traps on the Performance of Bulk Channel Charge-Coupled Devices," *IEEE Trans. Elec. Dev.*, **ED-21**, p. 701, (1974).

Review and Analysis of Laser Annealing

A. E. Bell

RCA Laboratories, Princeton, N.J. 08540

Abstract—A review of the recently published literature indicates that laser annealing is a technique that is widely applicable to the thermal processes commonly required during semiconductor device fabrication. The experimental results for annealing with *Q*-switched ruby ($\lambda = 0.69\ \mu m$) and Nd:YAG ($\lambda = 1.06\ \mu m$) lasers as well as cw lasers are reviewed. Applications discussed include the annealing of implantation damage, annealing of electrically active defects in the surface regions of pure semiconductors, and laser-induced surface reactions leading to the formation of metal-silicide compositions at the surface of the silicon.

A one-dimensional thermal model for laser annealing is developed and used to model the thermal evolution of the silicon wafer over a very wide range of pulse durations and absorption coefficients, the latter being determined by the choice of laser wavelength. The model calculations are specifically used to predict threshold pulse energies, recrystallization velocities, melt depths, and the onset of surface boiling. The model is compared with experimental data and good agreement is found for a wide range of pulse times (2×10^{-8} - 2×10^{-4} sec) and absorption coefficients (10^2-10^6 cm^{-1}). In particular the effect of the increased optical coupling to an amorphous surface layer on a single-crystal wafer was computed and found to be in good agreement with experiments on the laser annealing of ion-implantation damage.

1. Introduction

High-power lasers have been utilized in the industrial processing of materials for many years now.[1] Such applications include the cutting and welding of metals, drilling of ceramics, surface hardening of metals and alloys, resistor trimming, and contact soldering. Despite the emergence of these applications, it is only relatively recently that high-power

pulsed and cw lasers have been applied to the various thermal annealing treatments required during the processing of silicon and other semiconductor materials for semiconductor device fabrication. The pioneering work in this area was done by Russian workers,[2-4] and a large and rapidly growing volume of published work has now appeared in the literature. In the first section of this report we briefly review this literature in order to assemble experimental data for comparison with a thermal model for laser annealing which will be developed in the second section. Many of the beneficial effects of laser annealing can be understood in terms of the formation of a thin molten or liquid layer of silicon on the incident surface of the laser-irradiated specimen. It is, therefore, important to have a thermal model of the process in order to predict and understand the experimental consequences of such parameters as the pulse duration, pulse energy density, and the wavelength of the radiation.

2. Review of Laser Annealing

The most commonly reported application for laser annealing is to recrystallize the heavily damaged (amorphized) surface layers that occur as a result of ion implantation doping.[5-15,29,30] Using conventional furnace annealing procedures, the entire wafer is heated to temperatures of 1000°C or higher for periods of about ½ hr. This process is not always able to restore crystal perfection in the implanted region and often leads to deleterious effects on both the crystalline perfection and the chemical purity of the silicon in the bulk of the wafer. Moreover, such thermal treatments often result in a high concentration of electrically inactive dopant atoms in the form of precipitates close to the surface of the wafer, leading in turn to short carrier lifetimes within this region.[16]

Several advantages are claimed for the laser annealing technique:

(1) Fine spatial control of the area that is recrystallized on the wafer is possible.

(2) Control of the dopant diffusion depth is possible by varying the conditions of pulse length and pulse intensity.

(3) Due to extremely high recrystallization velocities (10^2–10^3 cm/sec) of the melted surface layer, substitutional solid solutions are obtained with dopant impurity levels well in excess of conventionally observed values. Residual precipitates are almost entirely eliminated.[16]

(4) Only the surface region of the wafer is exposed to elevated temperatures, so that bulk crystallinity is not degraded.

(5) Since laser annealing is an extremely rapid event, there is no need for vacuum conditions or special inert atmospheres to prevent oxidation or contamination during the annealing procedure.

Laser annealing has been demonstrated using a variety of laser sources and a wide range of pulse-duration and pulse-energy conditions. In Table 1 we summarize the data reported for laser annealing of ion-implantation damage using Q-switched ruby lasers, which operate at $\lambda = 0.694$ μm.[6,10-12,16] For implanted silicon wafers, the various experimental data are fairly consistent and indicate a threshold for the onset of annealing of ~1-1.5 J/cm^2 pulse, and melted regions up to 0.5-μm deep are possible with pulse energies in the range 2-3 J/cm^2 for a 50 nsec duration pulse. Table 1 also includes reported data for ruby laser annealing of Te implanted GaAs wafers.[30] Traditional thermal annealing of GaAs in a furnace is particularly difficult due to the tendency of this material to decompose above relatively low temperatures of 200-300°C, so that special techniques of hot implantation or 'capped' annealing to 900°C with SiO_2 or Si_3N_4 layers are required. Laser annealing with an 18-nsec pulse of ~0.3 J/cm^2 resulted in recrystallization of the damaged region with a very high degree of substitutional location for the Te atoms. The local concentration of Te atoms (~10^{21} Te/cm^3) in the annealed region exceeds the conventional solubility limit by more than one order of magnitude.

Table 2 summarizes the reported data for Q-switched Nd:YAG lasers, which operate in the infrared at $\lambda = 1.06$ μm.[5,7,9] For 110-nsec FWHM pulses, the critical pulse energy to achieve melting of the ion-implanted

Table 1—Annealing Implantation Damage with Q-Switched Ruby Lasers ($\lambda = 0.694$ μm)

Pulse Conditions (nsec)	Wafer	Results	Ref.
$\tau_p = 60$	Si: 10^{16} B/cm^2 (35 KeV) 1.16×10^{16} P/cm^2 (80 KeV) 1.4×10^{16} As/cm^2 (100 KeV)	0.64 J/cm^2 no effect 1.1 J/cm^2 threshold 1.5-1.7 J/cm^2 activates implanted atoms	10
$\tau_{FWHM} = 50$	Si: 5×10^{15} As/cm^2 (400 KeV)	2.0 J/cm^2 0.3 μm melt 3.0 J/cm^2 0.5 μm melt 1.5 J/cm^2 threshold	6, 11
$\tau_p = 50$	Si: 2×10^{16} B/cm^2 3.2×10^{11} precipitates/cm^2 in 200 Å surface layer; precipitates ~100 Å diameter	1.5-1.8 J/cm^2 Pulse redistributes B to 0.45 μm and eliminates precipitates	16
$\tau_p = 30$-50	Si: 10^{14}-10^{17} B/cm^2 (35 KeV)	1.5-1.7 J/cm^2 provides dopant electrical activity and better minority carrier diffusion lengths than thermal anneal	12
$\tau_{FWHM} = 12$	GaAs with ~7×10^{15} Te/cm^2 (50 KeV)	0.3 J/cm^2 results in regrowth of implant layer with Te in substitutional locations at a local concentration ~10^{21} Te/cm^3	30

Table 2—Annealing Implantation Damage with Q-Switched Nd:YAG Lasers (λ = 1.06 μm).

Pulse Conditions (nsec)	Wafer	Results	Ref.
τ_{FWHM} = 110	Si: 2.5 × 10^{15} Sb/cm^2 (150 KeV), 8 × 10^{15} As/cm^2 (100 KeV)	Recrystallization for peak power ≥57 MW/cm^2 or pulse energies ≥6 J/cm^2	5
τ_p = 20	Si: 10^{16} B/cm^2 (20–80 KeV)	Pulse energy of 0.8 J/cm^2 gives sheet resistivity identical to thermal anneal	7
τ_p = 110	Si: 10^{15} As/cm^2, 10^{16} As/cm^2, 5 × 10^{16} As/cm^2 (60 KeV)	Peak pulse power 57 MW/cm^2 annealed only 10^{16} and 5 × 10^{16} As/cm^2 samples. Implies implantation atoms and degree of damage affects coupling of laser pulse.	9
τ_p = 10, Freq. Doubled λ = 0.5 μm	GaAs implanted with 5 × 10^{15} Te/cm^2 (200 KeV)	20 MW/cm^2 pulse power annealed implantation damage. Some As loss. E ≈ 0.2 J/cm^2	29

surface is about 6 J/cm^2. A much lower value of only 0.8 J/cm^2 was reported[7] for pulses of 20-nsec duration incident on very heavily B-implanted Si. In one experiment[29] a frequency-doubled Nd:YAG laser operating at λ = 0.5 μm and 10-nsec pulses was used to anneal Te-implanted GaAs. A pulse energy of only 0.2 J/cm^2 was sufficient to recrystallize the implanted layer and there was evidence that some loss of As (a few percent) occurred as a result of the annealing process.

CW gas laser sources have also been used to cause laser annealing of implantation damage[8,13,17] (Table 3). A scanning Ar^+ ion laser (λ = 0.515, 0.488 μm) focused to a 50-μm spot diameter moving with a velocity of 12.5 cm/sec (dwell time ≈410^{-4} sec) required a power of 14 W to anneal a sample maintained at 250°C.[17] In the case of a scanning (9.8 cm/sec) Kr^+ laser beam (λ = 0.647 μm, 0.676 μm) a laser power of 6 W was used to anneal a sample maintained at 178°C.[8]

Table 3—Annealing Implantation Damage with CW Lasers

Scan Conditions	Wafer	Results	Ref.
9.8 cm/sec scan Kr^+ ion laser λ = 0.647, 0.670 μm 3:1	2 × 10^{15} B/cm^2 (35 KeV)	6 W laser output increased electrical activity to that after thermal anneal *without* B diffusion	8
12.5 cm/sec scan 50 μm spot Ar^+ ion laser λ = 0.515, 0.488 μm	5 × 10^{14} B/cm^2 (60 KeV) CVD Si on Si_3N_4 layer on Si	Growth in crystallite size for laser powers 11–14 W when ambient held at 250–350°C	17

The evidence for recrystallization of the implanted surface layer presented in the references of Tables 1–3 is quite convincing and is mainly supported by two separate observations. The first indication of recrystallization comes from the observation[7,8,16,18] of a dramatic reduction in the sheet resistance after the exposure of the sample to laser pulse. The measured sheet resistance falls to a value close to that observed for implanted wafers annealed using the standard thermal technique. The sheet resistance drops from a typical value of 10^3–10^4 ohms/□ to a value 10–100 ohms/□ after laser annealing. This indicates that the implanted species is located substitutionally after the laser pulse, and this conclusion is further supported[16] by the disappearance of precipitate clusters of dopant atoms that were present close to the surface of the wafer prior to the laser pulse. The second indication in support of recrystallization is derived from backscattering and channeling spectra of 1–2 MeV $^4He^+$ ions from the ⟨100⟩ Si planes.[5-7,9,29,30] The backscattering yield, an indication of the degree of randomness of the Si atom sites in the vicinity of the surface, shows a drastic reduction after exposure of the sample to the laser pulse. As with the sheet-resistance measurement, the backscattering yield after laser annealing has a value similar to that observed for implanted wafers subject to standard thermal annealing.

Although most of the evidence supports a hypothesis that calls for recrystallization as a result of the formation of a thin molten layer (0–1.0 μm) on the surface of the silicon wafer, there are some arguments made for solid-state recrystallization of the implantation-damaged region.[8] The evidence supporting the melted-layer model is both experimental and theoretical in nature. The main experimental justification is that when the pulse energy exceeds the threshold value to cause annealing, the distribution of dopant atoms (as measured by SIMS for example) shows that these atoms have migrated several thousand angstroms from their distribution in the implanted sample before annealing.[5-7,9,10,19] Since the duration of the annealing pulse is very short ($\leq 10^{-7}$ sec), it is not possible, using the typical solid-state diffusion coefficient $D_S \approx 10^{-12}$–10^{-14} cm²/sec, to explain an impurity diffusion length greater than ~1 Å.[6,11] We can calculate the magnitude of the diffusion constant required to cause a diffusion length of l cm in a time τ by using the relationship

$$l = \sqrt{D\tau}$$

or

$$D \approx \frac{l^2}{\tau}. \qquad [1]$$

If we use typical experimental values of $l = 10^{-5}$ cm (0.1 μm) and $\tau \approx 10^{-7}$ sec, then $D \approx 10^{-3}$ cm^2/sec. This value is more typical of diffusion constants in liquid materials; furthermore, several calculations[6,14,20] that assume diffusion constants of this magnitude are able to predict quite well the dopant distribution that results after laser annealing.

One reference[8] found an increase in electrical activity of boron-implanted silicon after laser annealing with a scanning Ar^+ laser. In this case, *no* redistribution of the boron was observed and the authors claim this as evidence for recrystallization without melting. More recently an alternative mechanism referred to as Pulsed Plasma Annealing (PPA) has been proposed.[21] In this mechanism, the laser light generates a high density of electron–hole pairs (plasma) in the surface layer of the sample, and these diffuse more rapidly than standard thermal diffusion. It is argued that due to the formation of the plasma the Coulomb interaction is screened and vacancies are allowed to migrate out of the lattice. Since the quanta are absorbed to create electron–hole pairs over very short periods, (1 nsec) the lattice is not heated and melting need not take place.

Other experimental evidence that supports the melting hypothesis is the observation of ripples on the surface of the sample after irradiation.[22–26] The ripples have been attributed to intensity modulation of the pulse energy due to interference effects between the primary wave and waves scattered from surface disturbances [dust, etc.].[22–24] Alternatively it has been suggested that they are due to the generation of a standing surface-acoustic-wave pattern generated as a result of a non-linear interaction between the liquid layer and the axial modes present in the incident pulse.[25] The ripple patterns have also been attributed to anisotropic melting and epitaxial regrowth of silicon.[27] In the experiments cited in Ref. [27], the duration of the laser pulse was considerably longer (~100 μsec) than those more typically used (~20–100 nsec), and it is possible that the ripple mechanism may depend on the duration of the laser-melted surface layer. In either case, the observation of the ripple is evidence for the formation of a liquid layer and can be used[26] as an indication of the threshold pulse energy required to cause annealing of surface defects in implanted silicon.

Time-resolved reflectivity measurements[15] of the surface of an ion-implanted silicon wafer show an abrupt increase in the reflectivity during the initial portion of the annealing pulse. The reflectivity rises to a value consistent with the value for liquid silicon and again supports the melted layer hypothesis. The reflectivity remained high for about 300 nsec before returning to a value corresponding to solid silicon, indicating that the melted layer can persist for relatively long periods of time compared to the duration of the pulse (50 nsec FWHM in this case).

Several theoretical models for laser annealing have been presented in the literature.[6,14,20] In all cases, including the model that will be developed in the latter half of this report, the experimentally observed pulse energies that result in annealing do predict the formation of a thin liquid layer (0–1 μm) when applied in the model calculation. The theoretical models, therefore, are not inconsistent with the melting and subsequent epitaxial recrystallization view for the mechanism of laser annealing.

Laser annealing experiments have been reported on many other types of samples besides ion-implanted silicon and GaAs wafers. In Table 4 we summarize the major results reported for laser annealing of pure silicon and GaAs wafers. Here, particularly in the case of irradiation at $\lambda = 1.06$ μm from the Nd:YAG lasers,[28] the threshold pulse energies for annealing are larger than those observed for ion-implanted silicon. This result is reasonable since the amorphization of the surface layer, which results from the implantation process, leads to an increased optical coupling of the incident laser pulse energy into the surface layer, thus reducing the pulse energy required to initiate melting or other annealing mechanism. On the other hand, the energy required to epitaxially recrystallize 3000 Å of electron-beam evaporated amorphous silicon deposited on a single-crystal silicon substrate[19] (2 J/cm^2, $\tau_p = 25$ nsec) is comparable to the pulse energy required (for pulses of similar duration) to melt a depth of 3000 Å of the implanted and, therefore, amorphized silicon in Table I.[6,10-12,16]

Another interesting application of laser annealing is in the area of laser induced reactions of platinum,[31] palladium,[32] and other metals with silicon to form surface layers of metal silicides suitable for making ohmic contacts to the semiconductor device. As was the case for annealing of ion-implantation damage, the conventional method for the formation of the silicide layer is to heat the entire wafer in a furnace at about one-

Table 4—Laser Annealing of Pure Semiconductor Materials

Pulse Conditions	Sample	Results	Ref.
$\lambda = 0.694$ μm $\tau_p = 20$ nsec	GaAs	Pulse power 48 MW/cm^2 (1 J/cm^2) required to melt surface	25
$\lambda = 1.06$ μm $\tau_p = 200$ nsec	Single-Crystal Si	Pulse energy 60 J cause surface melting and ripples developing preferentially along crystalline axes	27
$\lambda = 1.06$ μm $\tau_{FWHM} = 110$ nsec	Thermally Damaged	Pulse energies 55–110 J/cm^2 anneal damage to depth of 10–25 μm	28
$\lambda = 0.694$ μm $\tau_p =$ 20–25 nsec	3000 Å evaporated amorphous Si on crystalline Si	Pulse energy ~2.0 J/cm^2 caused epitaxial recrystallization	19

half the melting temperature of the metal silicide, which causes the vacuum-deposited metal surface layer to react with and diffuse into the surface of the silicon wafer. The experiments reported in the literature are summarized in Table 5 and show that it is possible to use laser annealing to induce the silicide formation with very rapid pulse times (<100 nsec) and moderate pulse energies (1–6 J/cm^2). In the case of short laser pulses, the silicide is not formed by solid-state diffusion. A melted layer of metal and silicon is formed at the surface of the wafer thus permitting rapid diffusion in the liquid state of the metal atoms into the surface region of the wafer. As the recrystallization front proceeds back towards the wafer surface, a range of compounds are precipitated from the greatly supercooled eutectic liquid. An interesting feature of the laser-induced reaction is that, depending on the pulse energy used, the melting occurs to greater depths in the silicon wafer[31] and the metal film is diluted with more silicon. It is possible, therefore, to obtain a whole range of average concentrations of the metal atoms in the silicide layer (see Table 5). Further advantages of this technique in device processing are that the conductive paths may be 'scribed' by a small focused annealing beam and that, due to the very localized region in which the temperatures are elevated, the ohmic contacts can be formed close to heat sensitive structures that already exist on the wafer. As with annealing of implantation damage, the short duration of the laser pulse makes this a potentially rapid production-line process that does not require special inert atmospheres. If pulses of longer duration are used, e.g., those produced by scanning a focused cw laser beam, then it is possible to induce the conventional solid phase thin-film reaction between the metal layer and the silicon wafer without the occurrence of surface melting.[33] Uniform layers of Pd_2Si were formed by scanning a focused beam of 6×10^5 W/cm^2 power across a silicon wafer coated with 2000 Å of Pd. The dwell time of the beam in this case was 0.3 msec.[34]

In surveying the various reports that have been made on the subject

Table 5—Laser-Induced Thin-Film Reaction

Laser	Sample	Results	Ref.
NdYAG $\lambda = 1.06\ \mu m$ $\tau_p = 125$ nsec 35-μm focus-spot dia.	Electron-beam Pt 450-2100 Å on silicon. Also, Ni, Pd, Mo, Nb	45 Å Pt/Si Sample 18 MW/cm^2 $PtSi_{2.7}$ 1700 Å 28 MW/cm^2 $PtSi_{5.5}$ 2700 Å 37 MW/cm^2 $PtSi_{9.1}$ 3000 Å 46 MW/cm^2 $PtSi_{10.4}$ 4500 Å $E \sim 2$–6 J/cm^2	31
Nd:YAG $\lambda = 1.06\ \mu m$ $\tau_p = 18$ nsec	Electron-beam Pd on Silicon 2000 Å layer	1.2–1.6 J/cm^2 pulse gives $Pd_{0.6}$ Si average composition	32
Scanned CW Laser $\tau_p = 0.3$ nsec	1000 Å Pd on silicon	6×10^5 W/cm^2 gave Pd-silicide layers ~0.2 μm thick	33, 34

of laser annealing, it is clear that a major new processing tool is being developed that will have a considerable impact on the fabrication of semiconductor materials and devices. Surface annealing or reactions can be controlled with extreme spatial precision, and no bulk degradation occurs due to uniform heating. Furthermore, compositional variations are possible that cannot be obtained with conventional techniques. Laser annealing optics and mechanisms are readily placed under computer control so that this technique is exceptionally well suited for automated manufacturing processes.

3. Thermal Analysis of Laser Annealing

3.1 Description of Model

3.1.1 Numerical Solution of the Diffusion Equation

The relaxation time for the electronic excitations that result from the absorption of the incident laser pulse is of the order 10^{-12} sec. Therefore, if we wish to describe the thermal evolution of the irradiated sample for pulse durations of 0.1 nsec or larger, it is quite permissible to use the conventional heat diffusion equations.[35] In the typical experimental configuration, the diameter of the incident pulse is ~1 cm and its duration is <1 μsec. The diffusion length for heat is

$$l \approx \sqrt{\kappa \tau}, \qquad [2]$$

where κ is the thermal diffusivity and τ is the duration of the diffusion. It is, therefore, much less than the beam diameter, and radial diffusion in the plane of the incident surface may be neglected. The diffusion equation in this case reduces to a one-dimensional equation, the solution of which will describe the time-dependent temperature distribution $T(x,t)$ along the x-axis, i.e., orthogonal to the sample surface (see Fig. 1),

$$\frac{\partial T}{\partial t} = \frac{1}{\rho C}\left\{\frac{\partial}{\partial x}\left[\kappa(T)\frac{\partial T}{\partial x}\right] + A(x,t)\right\}. \qquad [3]$$

In the solution of the diffusion equation, we assume that the density, ρ, and the specific heat C, in J/gm, are temperature independent. However, the equation is nonlinear since the thermal conductivity of silicon is strongly temperature dependent[36] and its variation must be taken into account. The term $A(x,t)$ represents the spatially distributed (see Fig. 1) and time-dependent energy density absorbed from the incident laser pulse, and our solution is able to take into account the effect of the change in the optical properties of the sample that occurs when surface melting begins.

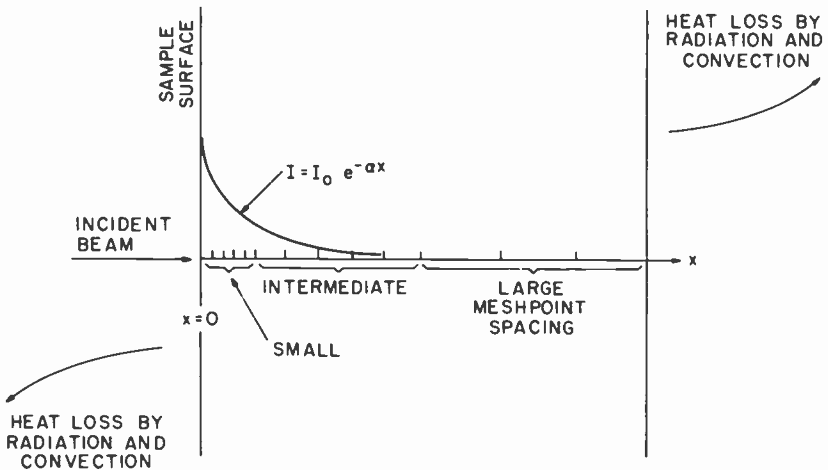

Fig. 1—Geometry, meshpoint spacing, and boundary conditions applied in the thermal model.

This nonlinear one-dimensional heat diffusion equation is solved using a finite-difference computer-based numerical procedure that uses the library subroutine TRIDAG. The solution is obtained in the form of the temperature distribution at the discrete meshpoints positioned along the x-axis of Fig. 1 given as a function of time. In order to minimize the total number of meshpoints, while still having adequate spatial resolution close to the sample surface ($x = 0$), the meshpoints are grouped into 3 sets, each with an increased value for the meshpoint spacing. The meshpoints with the smallest spacing begin at $x = 0$ where the temperature gradients are largest. Typically, at the surface the meshpoints are separated by 0.05 μm, and mesh expansion factors of 2 to 5 are used.

The boundary conditions applied at the first and last meshpoints, corresponding to the front and back surfaces of the sample, are that radiative and convective losses to the ambient T_A are permitted. These heat losses are of the form

$$\sigma\epsilon(T^4 - T_A^4) + G(T - T_A). \qquad [4]$$

where σ is Stefan's constant, ϵ is the emissivity, and G is the convective transfer coefficient. These heat losses are so small (~1 W/cm^2) compared to the input pulse energies (~10^6 W/cm^2) that the boundaries are, for all practical purposes, insulating during the laser pulse. However, if we wish to follow the thermal evolution of the wafer right through to the final cooldown to room temperature, these terms must be included since they represent the only cooling mechanism for the wafer.

Since surface melting plays an important role in laser annealing it is

necessary that the model be able to simulate the phase transition as it progresses inward from the surface, as well as during the recrystallization phase which generally occurs after the termination of the laser pulse. In the computer program, as soon as any meshpoint reaches the melting point (either during heating or cooling), the temperature of the meshpoint is held constant, and any energy absorbed from the laser or that diffuses into (or out of) the meshpoint is summed (or subtracted) from the latent energy that is necessary to melt (or freeze) the meshpoint. In this manner the output of the computer model includes the variation with time of the thickness of the melted layer. This feature of the solution is very important, since the melt depth, duration of melted layer, and the recrystallization velocity are all very important parameters that determine the physical effects of the laser annealing on the surface region of the sample.

For an independent check on the validity of the computed temperature distribution as a numerical solution to the diffusion equation, we invoke the principle of conservation of energy. At various prescribed times during the evolution of the solution, we take the temperature distribution as calculated and use it to compute the total heat energy distributed within the sample. This is compared to the total energy absorbed up to that time from the laser pulse, and we find that even with the strongly nonlinear thermal conductivity, this energy equation is balanced to better than 1% of the pulse energy.

3.1.2 Temperature Dependence of Thermal Properties

In the case of silicon, we solve the diffusion equation assuming constant values of density $\rho = 2.33$ gm/cm^3 and specific heat $C = 0.95$ J/gm/°C. The latent heat of fusion is taken to be 1660 J/gm. The thermal conductivity K of silicon is strongly temperature dependent falling from a value of 1.45 W/cm/°K at 300°K to a value of 0.25 W/cm/°K at the melting point, $T_M = 1683$°K (see Fig. 2). When melting occurs, the thermal conductivity of liquid silicon changes discontinuously to a value of 0.64 W/cm/°K. We approximate the temperature dependence of the conductivity of silicon by the following function:

$$\begin{aligned} &300°\text{K} < T < 1200°\text{K} && K = \frac{1521}{T^{1.226}} \\ &1200°\text{K} < T < 1683°\text{K} && K = \frac{8.97}{T^{0.502}} \\ &1683°\text{K} < T && K = 0.64 \text{ W/cm/°K} \end{aligned} \quad [5]$$

The experimental data[36] is compared to our function for the thermal conductivity in Fig. 2.

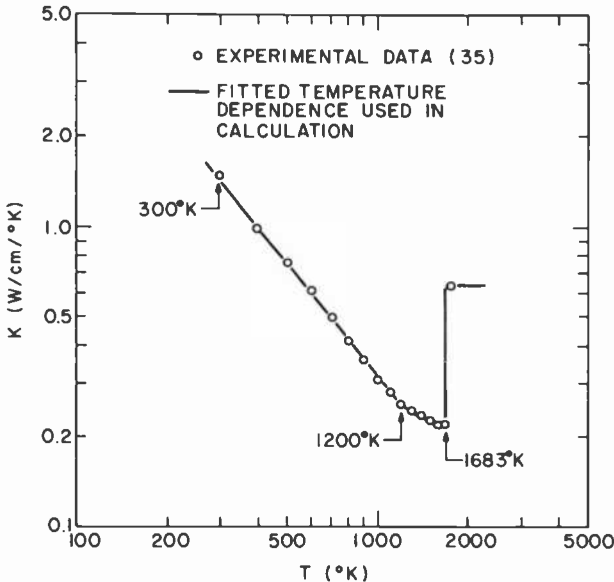

Fig. 2—Temperature dependence of the thermal conductivity of silicon: experimental and fitted values.

Rewriting Eq. [3] in numerical form, if we define the heat flux at the ith meshpoint as $\phi_i = K(T_i)(dT_i/dx)$, then

$$\left(\frac{\partial T}{\partial t}\right)_i = \frac{1}{\rho C}\left\{\frac{\partial \phi_i}{\partial x} + A_i(x_i,t)\right\}$$

$$= \frac{1}{\rho C}\left\{\frac{(\phi_{i+1/2} - \phi_{i-1/2}}{\Delta X} + A_i(x_i,t)\right\}, \qquad [6]$$

where $\phi_{i\pm 1/2}$ is the heat flux at the boundaries, $x_i \pm (\Delta X/2)$, of the ith meshpoint

$$\phi_{i+1/2} = K_{i+1/2}\frac{(T_{i+1} - T_i)}{\Delta X}, \; \phi_{i-1/2} = K_{i-1/2}\frac{(T_i - T_{i-1})}{\Delta X}. \qquad [7]$$

In these equations $K_{i\pm 1/2}$ is the thermal conductivity of the silicon at a temperature midway between that on the ith and $(i \pm 1)$th meshpoints.[37] The importance of including the temperature dependence of the thermal conductivity is demonstrated by Fig. 3 where we plot the surface temperature of the silicon calculated as a function of time including (curve I) and not including (curve II) the temperature dependence of the thermal conductivity. The temperature-independent conductivity was assigned a value of 1.45 W/cm/°C corresponding to T = 300°K. The incident power density used in both the calculations was 10^7 W/cm^2, and

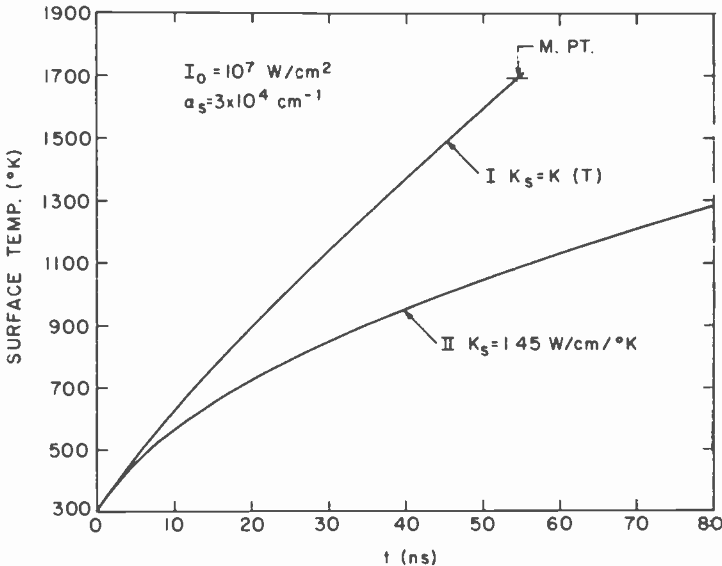

Fig. 3—Comparison of the surface temperature rise when the temperature dependence of the thermal conductivity of silicon is included (I) with that computed when K_S = 1.45 W/cm/°K is used as a temperature independent value (II).

it is apparent that when the temperature dependent conductivity is used the surface temperature increases more rapidly. This is because the reduction of the thermal conductivity with increasing temperature helps to reduce the heat conducted into the bulk of the wafer from the region of absorption close to the silicon surface. As a result of this reduced heat leak, the surface temperature increases more rapidly for a given pulse power density.

3.1.3 Optical Properties of Silicon

The optical properties of silicon[38–40] and liquid silicon[41] are summarized in Table 6 for the two wavelengths most commonly used for laser annealing, $\lambda = 0.69\ \mu m$ (ruby) and $\lambda = 1.06\ \mu m$ (Nd:YAG).

The values for the absorption coefficient shown for solid silicon are

Table 6—Optical Properties of Silicon

Ref.	α_s cm^{-1} $\lambda = 0.69\ \mu m$	α_s cm^{-1} $\lambda = 1.06\ \mu m$	Comment
40	2.5×10^3	50	Single crystal Si
39	4×10^3	100	Epitaxial Si
38	3×10^4	3×10^3	Amorphous Si (sputtered)
41	10^6	7×10^5	Liquid Si

measured at room temperature and, because of the unavailability of high temperature optical constants for most semiconductor materials, we have assumed that the room temperature values for the absorption coefficient remain constant up to the melting point. In fact, due to the generation of nonequilibrium free carriers[42] as well as the increased temperature at the surface region, we expect that the absorption coefficient would be larger for the material within ~1 μm of the surface. In the case of ion-implanted single-crystal silicon, the absorption coefficient of the implanted surface region will be more characteristic of amorphous silicon than of the original single crystal due to the large amount of damage caused by the implantation process.

In the calculation, when the surface temperature is below the melting point and no liquid layer exists, the absorption term $A(x,t)$ of Eq. [3] is given as

$$A(x,t) = (1 - R_S)\alpha_S I_0 e^{-\alpha_s x} \text{ W/cm}^3, \quad [8]$$

where R_S is the reflectivity of solid silicon, which is 0.35 for $\lambda = 0.69$ μm and 0.32 for $\lambda = 1.06$ μm.[43] When the surface begins to melt, the distribution of absorbed energy becomes more complex due to the very high absorption coefficient of the liquid. For example, in Fig. 4 we plot the reflectivity, absorption, and transmittance of a thin layer of liquid silicon on a substrate of solid silicon for $\lambda = 0.69$ μm. This calculation[44] shows that as the liquid layer thickness increases from zero to about 300 Å the reflectivity of the sample increases from 0.35 to 0.73, and the region of absorption is transferred progressively to the liquid layer. In the thermal calculation when the liquid layer exceeds 300 Å in thickness, we assume that all of the incident light that is not reflected is absorbed within the first 500 Å thick meshpoint, i.e.,

$$\begin{aligned} A(x,t) &= (1 - R_L)I_0, & x &= x_1 \\ &= 0, & x &\neq x_1 \end{aligned} \quad [9]$$

where R_L is the reflectivity of the liquid. For intermediate liquid-layer thicknesses $0 < d_M < 300$ Å, the calculation shown in Fig. 4 is used to determine what fraction of the incident beam is absorbed by the liquid layer and what function is transmitted through the liquid layer to be absorbed in the underlying solid region. This somewhat complicated procedure, which is used as the melted layer initiates, does not have a large effect on the results of the computation, but it does make the solution more stable. This is basically because we have eliminated the otherwise discontinuous change in the reflectivity from the solid value, R_S, to the value for the liquid, R_L, which would otherwise occur at the threshold of melting.

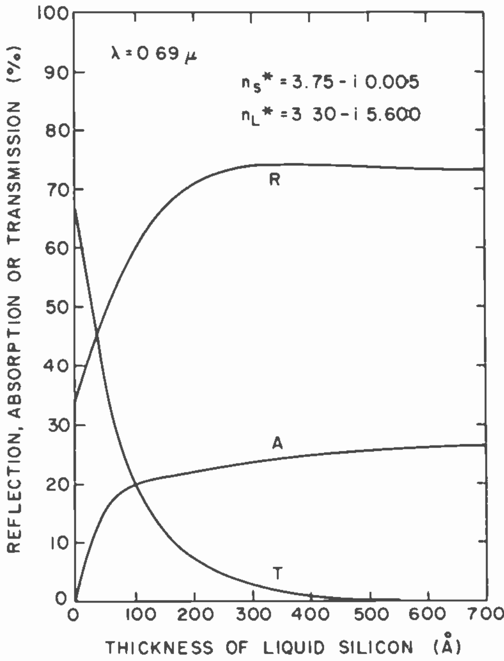

Fig. 4—Computed values for the reflectivity (*R*), transmittance (*T*), and absorption (*A*) of a layer of liquid silicon of variable thickness on a substrate of solid silicon, $\lambda = 0.69\ \mu m$.

3.2 General Results of the Calculation

3.2.1 Behavior of Model for Limiting Conditions

The general behavior of the solution to the computer model can be understood quite well by considering the relative values of the absorption length, α_S^{-1} cm, of the laser light within the sample surface, and the thermal diffusion length for heat during the pulse, Eq. [2]. Two regimes can be identified.

Regime (1): $l = \sqrt{\kappa_S \tau_p} \ll \alpha_S^{-1}$

In this limit, the temperature distribution in the silicon wafer is determined predominantly by the initial distribution of the energy absorbed from the laser beam. Thermal diffusion has minor impact on the thermal evolution during the pulse, and the solution tends towards the adiabatic solution in which the thermal diffusion can be neglected. The distribution of light intensity in the silicon is given by

$$I = (1 - R_S) I_o e^{-\alpha_s x}\ \mathrm{W/cm^2}, \qquad [10]$$

so that the rate of generation of heat is

$$A = -\frac{dI}{dx} = \alpha_S(1 - R_S)I_o e^{-\alpha_S x} \text{ W/cm}^3, \quad [11]$$

which is proportional to the absorption coefficient at any given value of x.

Regime (2): $l = \sqrt{\kappa_S \tau_p} \gg \alpha_S^{-1}$

In this limit, the temperature distribution in the silicon wafer is determined predominantly by diffusion of the heat absorbed from the laser beam further into the bulk of the irradiated samples. When the thermal diffusivity, κ_S, is temperature independent, this problem can be solved exactly and is well approximated by the analytical solution to the problem of a semi-infinite solid heated by a flux of energy absorbed at the surface.[35] That is, we can neglect the exponential spatial distribution of the energy flux given in Eq. [10], since the spatial profile is entirely washed out by the subsequent diffusion of the thermal energy on the time scale of the pulse. The temperature distribution is given by the expression

$$T(x,t) = \frac{2(1 - R_S)I_0}{K_S}\left\{\sqrt{\frac{\kappa_S t}{\pi}} \exp\left(\frac{-x^2}{4\kappa_S t}\right) - \frac{x}{2}\operatorname{erfc}\left(\frac{x}{2\sqrt{\kappa_S t}}\right)\right\}, \quad [12]$$

so that the temperature rise of the surface, $x = 0$ reduces to

$$T(0,t) = \frac{2(1 - R_S)I_0}{K_S}\left(\frac{\kappa_S t}{\pi}\right)^{1/2}. \quad [13]$$

Eq. [13] indicates that the surface temperature rise in the strong diffusion limit depends only on the total absorbed flux, $(1 - R_S)I_0$, and has no dependence on the spatial distribution of the absorption which is determined by α_S.

Having established the behavior of the laser annealing model for the two extreme limits of adiabatic ($\sqrt{\kappa_S \tau_p} \ll \alpha_S^{-1}$) and strong diffusion ($\sqrt{\kappa_S \tau_p} \gg \alpha_S^{-1}$), we will now review the details of the general model solution with reference to these two limiting behaviors.

3.2.2 Dependence of Threshold Pulse Energy on Absorption Coefficient, α_S

In Fig. 5 we present the incident threshold power density, I_0^T, required to just cause melting as a function of the absorption coefficient of the solid. Three cases are shown, corresponding to square intensity profile pulses of 25 nsec, 50 nsec, and 110 nsec duration. If we consider the data for the τ_p = 50 nsec pulse, then we see that as the absorption coefficient is reduced the threshold power required increases slowly at first, and for $\alpha_S \lesssim 5 \times 10^3$ cm^{-1} the solution shows that

$$I_0^T \propto \frac{1}{\alpha_S}. \quad [14]$$

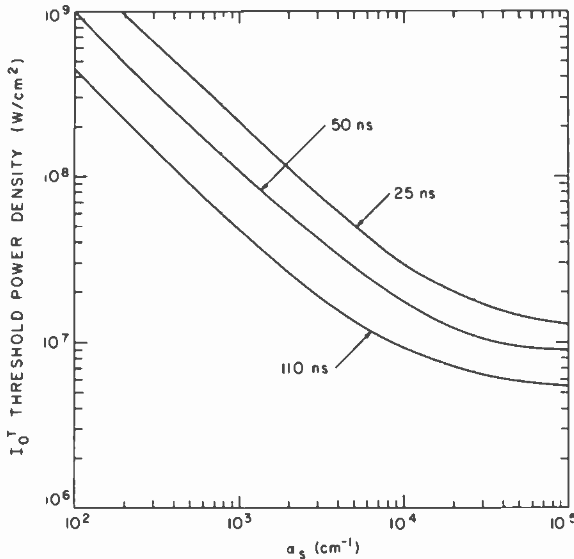

Fig. 5—Dependence of the threshold pulse incident power density on the absorption coefficient, α_S, and pulse duration, τ_p.

In the case of a 50-nsec pulse, the characteristic absorption length, which separates the adiabatic region from the strong diffusion region, is given by

$$\alpha_S^{-1} \approx \sqrt{\kappa_S \tau_p}\,. \qquad [15]$$

Thus, if we take $\kappa \approx 0.34$ W/cm/°K and $\tau_p = 50 \times 10^{-9}$ sec,

$$\alpha_S^{-1} \approx 1.3 \times 10^{-4} \text{ cm}$$

$$\alpha_S \approx 8 \times 10^3 \text{ cm}^{-1}.$$

Therefore, for $\alpha_S \ll 8 \times 10^3$ cm^{-1}, diffusion becomes less and less important and the power absorbed at the surface layer δx thick is given by Eq. [11] as

$$A = \alpha_S(1 - R_S)I_0\delta x. \qquad [16]$$

The energy required to elevate this layer to the melting point T_M is $C_p\delta x T_M$, which must be supplied in time τ_p. Thus the condition for just reaching the melting threshold is

$$A\tau_p = \tau_p\alpha_S(1 - R_S)I_0^T\delta x = C\rho\delta x T_M, \qquad [17]$$

so that the threshold incident power density is given by

$$I_0^T = \frac{C\rho T_M}{(1 - R_S)\tau_p}\frac{1}{\alpha_S}\,. \qquad [18]$$

Eq. 18 agrees with the observed linear dependence of Fig. 5 noted in Eq. [14].

For $\alpha_S \gg 8 \times 10^3$ cm the solution becomes diffusion limited and the surface temperature is given by Eq. [13]. If the surface is to just reach the melting point at the termination of the pulse, Eq. [13] can be re-written as

$$T_M = \frac{2(1 - R_S)I_0}{K_S}\left(\frac{\kappa_S \tau_p}{\pi}\right)^{1/2}, \qquad [19]$$

so that in this limit of large τ_p

$$I_0^T = \frac{K_S T_M}{2(1 - R_S)}\left(\frac{\pi}{\kappa_S \tau_p}\right)^{1/2}. \qquad [20]$$

Eq. [20] is independent of the absorption coefficient, and this behavior is apparent in Fig. 5 for $\alpha_S \gtrsim 3 \times 10^4$ cm^{-1}.

The two equations that represent the limiting thermal behavior for threshold power density, Eqs. [18] and [20], both have a dependence on the pulse length τ_p for fixed α_S. In the adiabatic limit of small α_S (weak absorption), the threshold power is inversely proportional to the pulse length; whereas in the strong diffusion limit (strong absorption), the threshold power is proportional to the inverse of the square root of the pulse duration. The threshold powers predicted by the computer solution of Fig. 5 are plotted as a function of pulse length for $\alpha = 2 \times 10^2$ cm^{-1} (adiabatic) and $\alpha_S = 10^5$ (strong diffusion) in Figs. 6 and 7, respectively. The computer solution is consistent with the predicted limiting behavior of the analytical solution.

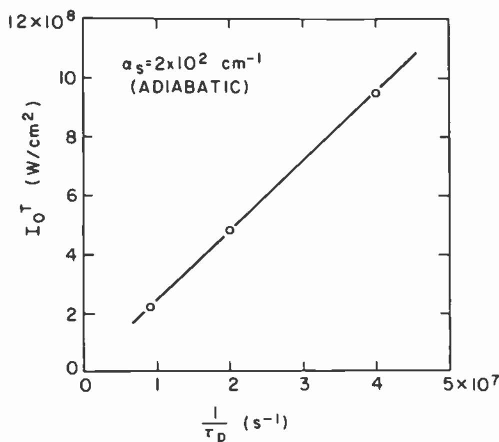

Fig. 6—Dependence of the threshold pulse power density on the pulse duration in the adiabatic limit when $\alpha_S^{-1} \gg \sqrt{\kappa_S \tau_p}$.

The experimental results on laser annealing are often reported in terms of pulse energy and pulse duration. In Fig. 8 we have replotted the computed data presented in Fig. 5 in the form of pulse energy versus absorption coefficient. For low values of α_S, the pulse energy required in the adiabatic limit is independent of the pulse duration, and this is a direct consequence of Eq. [18], which can be rewritten

$$E^T = I_0^T \tau_p = \frac{C\rho T}{(1 - R_S)} \frac{1}{\alpha_S}. \quad [21]$$

The threshold energy is thus independent of τ_p and proportional to the inverse of the absorption coefficient. In the strong diffusion limit we can rewrite Eq. [20] in the form

$$E^T = I_0^T \tau_p = \frac{K_S T_M}{2(1 - R_S)} \left(\frac{\pi}{\kappa_S}\right)^{1/2} \sqrt{\tau_p}, \quad [22]$$

so that $E^T \propto \sqrt{\tau_p}$ and less energy is required for pulses of shorter duration. This is a direct result of the dominant role of the thermal diffusion. The absorbed energy does not diffuse as far into the sample, so that the surface can reach the melting point with less of the material in the subsurface region being heated.

3.2.3 Dependence of Threshold Pulse Energy on Pulse Duration, τ_p

In this section, we consider the impact of the pulse duration on the threshold pulse energies for conditions of constant absorption coefficient. As discussed in the previous section, the character of the solution depends on the relative values of the absorption depth and the diffusion length. For a given value of absorption coefficient, a characteristic time

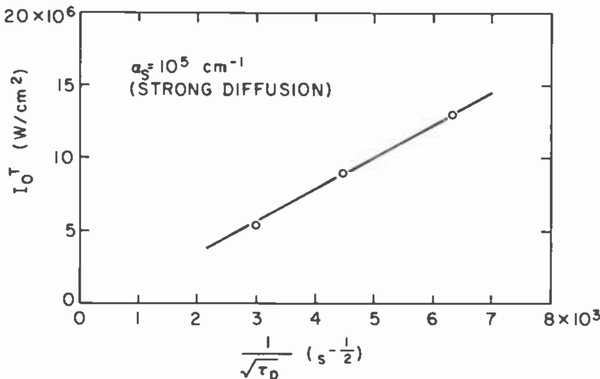

Fig. 7—Dependence of the threshold pulse power density on the pulse duration in the strong diffusion limit when $\alpha_S^{-1} \ll \sqrt{\kappa_S \tau_p}$.

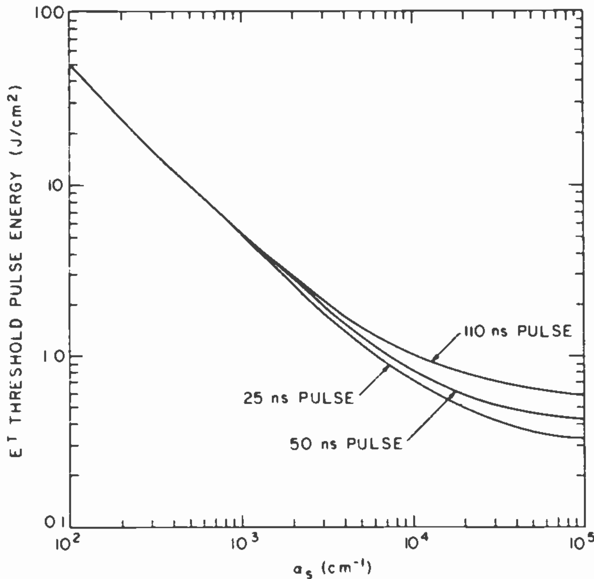

Fig. 8—Dependence of the threshold pulse energy density on the absorption coefficient and the pulse duration, τ_p.

can be defined:

$$\tau_c = \frac{(\alpha_S{}^{-1})^2}{\kappa_S} = \frac{1}{\kappa_S \alpha_S{}^2}. \quad [23]$$

When $\tau_p \ll \tau_c$, negligible diffusion takes place and the solution is essentially adiabatic. When $\tau_p \gg \tau_c$, the solution is dominated by thermal diffusion into the bulk of the silicon of the energy absorbed near the surface. As an example we take the case when $\alpha_S = 3 \times 10^4$ cm^{-1}, which corresponds (Table 6) to the value for amorphous silicon at $\lambda = 0.69$ μm. In this case, from Eq. [23], $\tau_c \approx 3$ nsec.

In Fig. 9 we present the computed incident power density required to reach melting threshold and also that required to produce a melted surface layer 0.5 μm thick, both as a function of the pulse duration, assuming a square intensity profile for the pulse. The same data is replotted in terms of the pulse energy in Fig. 10. It is worth noting that for strong absorption in the adiabatic limit, a large increase in the incident pulse energy is required beyond threshold to cause a 0.5-μm melt depth. The relative increase becomes less as the pulse length increases, a direct result of the reduction of the surface temperature gradient at threshold due to the increased thermal diffusion (this will be discussed in detail later). When $\tau_p \ll \tau_c$, the annealing process is adiabatic and the pulse energy required becomes progressively more independent of the pulse

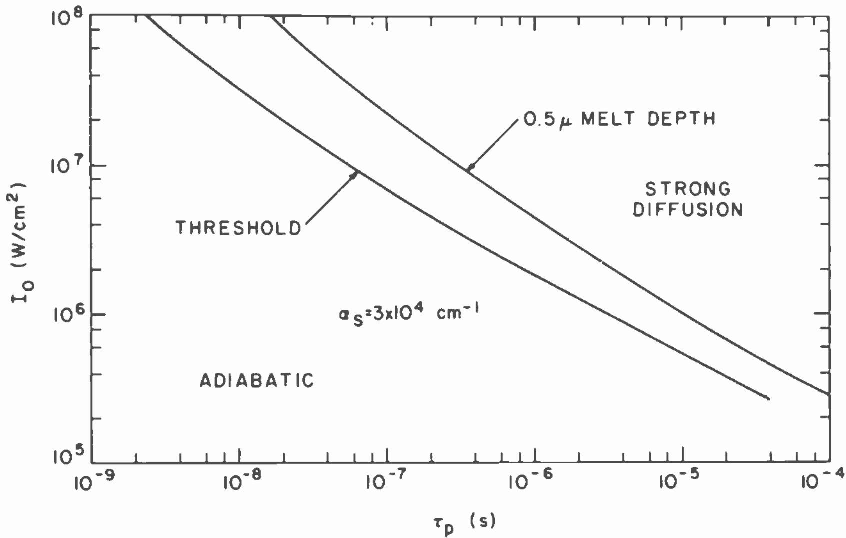

Fig. 9—Dependence of the melting threshold pulse power density and the power density required to melt 0.5-μm deep on the pulse duration when $\alpha_S = 3 \times 10^4$ cm^{-1}.

duration (Fig. 10). This is consistent with Eq. [21]. For longer pulse times, $\tau_p \gg \tau_c$, thermal diffusion results in a significant loss of the energy absorbed in the surface region ($\approx$1 μm in this case) to the bulk of the silicon wafer. This heat loss from the surface results in a progressively higher requirement for threshold and melting pulse energies as the pulse du-

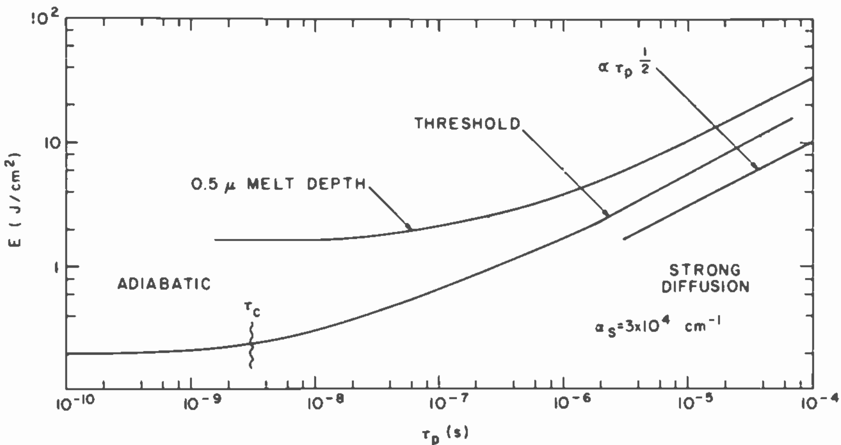

Fig. 10—Dependence of the melting threshold pulse energy density and the energy density required to melt 0.5-μm deep on the pulse duration when $\alpha_S = 3 \times 10^4$ cm^{-1}.

ration is increased and, eventually, $E^T \propto \sqrt{\tau_p}$, as dictated by Eq. [20] and demonstrated in Fig. 10.

The same analysis of threshold pulse energy dependence on pulse length was performed for $\alpha_S = 3 \times 10^3\ cm^{-1}$ and $\alpha_S = 100\ cm^{-1}$. These two values are consistent with the absorption of amorphous silicon and epitaxial single-crystal silicon at $\lambda = 1.06\ \mu m$, respectively (Table 6). This data is compared with that for $\alpha_S = 3 \times 10^4\ cm^{-1}$ in Fig. 11. When $\alpha_S = 3 \times 10^3\ cm^{-1}$ and $100\ cm^{-1}$, Eq. [23] gives the characteristic time constant separating the adiabatic and strong diffusion limits of the solution as $\tau_c \approx 3 \times 10^{-7}$ sec and $\tau_c \approx 3 \times 10^{-4}$ sec, respectively. Fig. 11 demonstrates that in the adiabatic $\tau_p \ll \tau_c$ limit, the minimum value of the threshold pulse energy increases in inverse proportion to the value of the absorption coefficient. Also, when $\tau_p \gg \tau_c$, the strong diffusion limit, all of the curves lead to a single asymptote where $E^T \propto \sqrt{\tau_p}$, regardless of the value of the absorption coefficient, α_S. For small values of the absorption coefficient, the temperature gradient at the surface is small compared to the case for large absorption coefficients and short pulse duration. Therefore, the additional pulse energy to cause a 0.5-μm melted layer is only slightly greater than that required to achieve the threshold of melting.

Fig. 11 shows that the threshold pulse energy density for annealing processes where the radiation is only weakly absorbed can be almost independent (within a factor of two) of the pulse duration over a broad range of practically accessible values. However, for strongly absorbed radiation, the pulse energy varies by a few orders of magnitude in the same range of pulse duration.

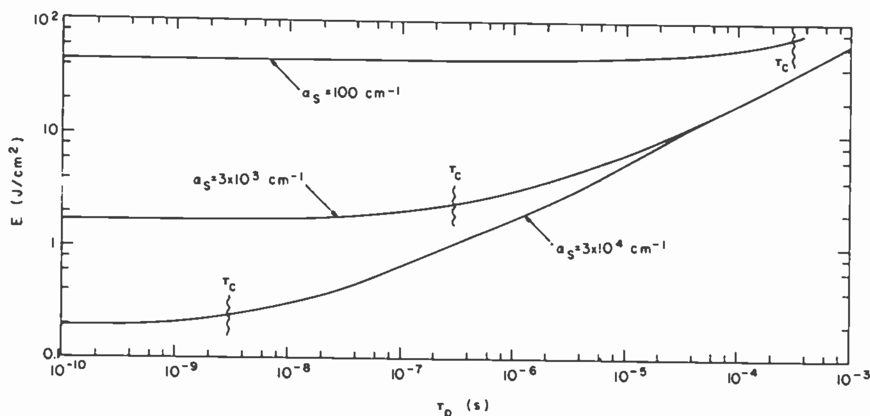

Fig. 11—Dependence of the melting threshold pulse energy density on the pulse duration, compared for $\alpha_S = 100\ cm^{-1}$, $3 \times 10^3\ cm^{-1}$, and $3 \times 10^4\ cm^{-1}$.

Despite the nonlinearity introduced by the temperature dependence of the thermal conductivity of silicon, it is possible to construct a "universal" curve for use with silicon-based samples. This curve describes the general behavior of the threshold pulse energy density as a function of both the absorption coefficient and the pulse duration by using the normalized coordinates of $E^T \alpha_S$ and $\tau_p \alpha_S{}^2$. The curve is shown in Fig. 12 and it provides a useful general guide for predicting the threshold energy density for any given combination of pulse duration and absorption coefficient.

3.2.4 Predictions of the Model for Pulse Energy Densities Above Melting Threshold

The most important feature of the laser annealing process once the liquid surface layer begins to form is that the absorption coefficient in the liquid silicon is much greater than that in the solid, and it is much less dependent on the wavelength of the incident radiation.[41] As a consequence, the reflectivity increases, reducing the fraction of the incident radiation absorbed. Moreover, the radiation that does enter the sample generates thermal energy only within the first ~0.05 μm of the melted region. The temperature distribution within the irradiated sample at the onset of melting depends strongly on the pulse duration and the wavelength of the radiation used (i.e., the magnitude of the absorption coefficient). The subsequent evolution of the melted layer then depends on this temperature distribution, since it will determine the heat loss to the bulk from the liquid/solid surface, and also on the incident power density, which will provide additional energy to the interface, increasing further the depth of the melted layer.

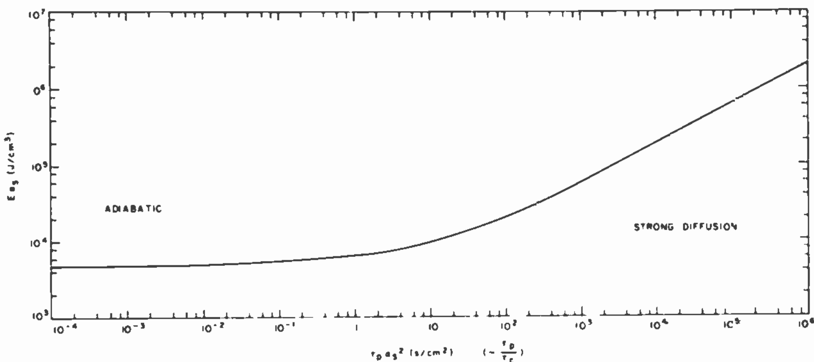

Fig. 12—"Universal curve," applicable to silicon-based samples, which allows the melting threshold pulse energy density to be estimated for a wide range of pulse duration and absorption coefficients.

In Fig. 13 we show the temperature distribution in the silicon at $t \approx 10^{-6}$ sec for incident power densities of 48×10^6, 3.2×10^6, and 1.8×10^6 W/cm^2, which are required to just reach melting threshold in this time period for absorption coefficients of 3×10^4, 3×10^3 and 100 cm^{-1}, respectively. In the case of $\alpha_S = 100$ cm^{-1}, $\tau_p = 1$ μsec is much less than the characteristic time constant $\tau_c \approx 3 \times 10^{-4}$, and therefore the very extended temperature distribution into the sample at the onset of melting is due to the large absorption depth of $\alpha_S^{-1} = 100$ μm, with thermal diffusion playing an insignificant role during this time period. The temperature distribution for the case when $\alpha_S = 3 \times 10^3$ cm^{-1} does not extend as far into the sample and, since $\tau_c \approx 3 \times 10^{-7}$ sec, thermal diffusion plays a more significant role in the development of the computed temperature profile at this time. The temperature gradient in the distribution computed for $\alpha_S = 3 \times 10^3$ cm^{-1} is lower in the region $x \lesssim 1 \mu$m than at larger depths. This is a result of the still moderately large penetration of the absorption profile of the incident beam, $\alpha_S^{-1} \approx 3$ μm in this case. The computed solution at melting threshold for $\alpha_S = 3 \times 10^4$ cm^{-1} shows the steepest temperature gradient with very little flattening in the surface region. In this case, the characteristic time $\tau_c \approx 3 \times 10^{-9}$ sec, which is much less than the pulse duration in Fig. 13; therefore, the extended temperature profile is due mainly to the diffusion of

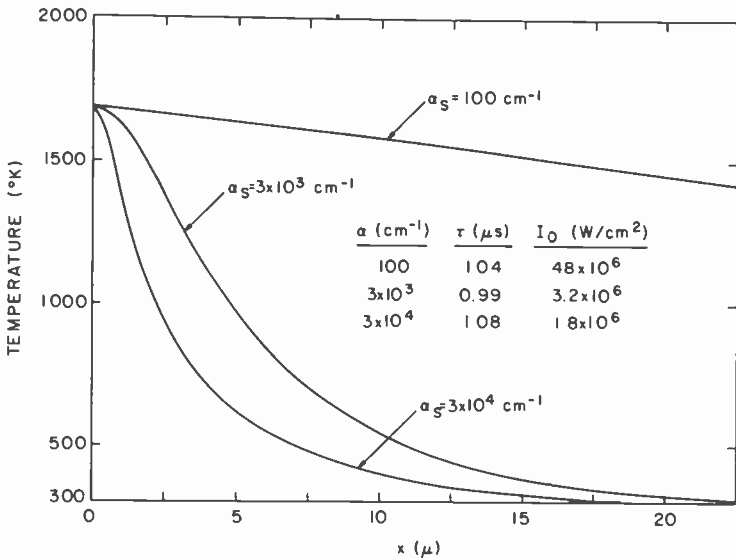

Fig. 13—Temperature distributions at melting threshold ($d_M = 0.0$ μm, $T(0) = T_m$) for $\alpha_S = 100$ cm^{-1}, 3×10^3 cm^{-1}, and 3×10^4 cm^{-1}. The power density is chosen in each case to result in the melting threshold occurring at $t \approx 10^{-6}$ sec.

the heat into the silicon from the relatively limited region of absorption, which extends only about $\alpha_S^{-1} = 0.3\ \mu m$ below the incident surface.

The time dependence of the depth of the melted silicon layer d_M is shown in Fig. 14 for the low, moderate, and high absorption coefficient cases. In order for the velocity of the melting front to have a value of V cm/sec, it is necessary to supply latent energy at a rate $V\rho L$ J/sec/cm^2 to the liquid solid boundary (L is the latent heat of melting in J/gm). Once the liquid layer thickness is greater than ~0.05 μm (Fig. 4), the nonreflected portion of the incident energy is entirely absorbed in the first 0.05 μm of the liquid layer and then is conducted to the liquid/solid interface. Energy is lost by conduction from the liquid/solid interface into the bulk of the sample by conduction down the temperature gradient in the solid immediately adjacent to the interface. The velocity of melting is determined by the balance between the energy conducted through the liquid layer from the surface region of absorption of the laser beam and that which diffuses into the solid region, i.e.,

$$-K_L\left(\frac{\partial T}{\partial x}\right)_{X_l-\delta x} = -K_S\left(\frac{\partial T}{\partial x}\right)_{X_l+\delta x} + V\rho L. \quad [24]$$

Here K_L is the thermal conductivity of liquid silicon and K_S is that of solid silicon measured at the melting point, X_l is the instantaneous position of the liquid/solid boundary, and $V = \partial X_l/\partial t$ is the velocity of propagation of the melt front. The LHS of Eq. [24] is approximately equal to the total energy flux absorbed in the liquid from the laser beam, $(1 - R_L)I_0$, so that

$$V \approx \frac{1}{\rho L}\left\{(1 - R_L)I_0 + K_S\left(\frac{\partial T}{\partial x}\right)_{X_l+\delta x}\right\}. \quad [25]$$

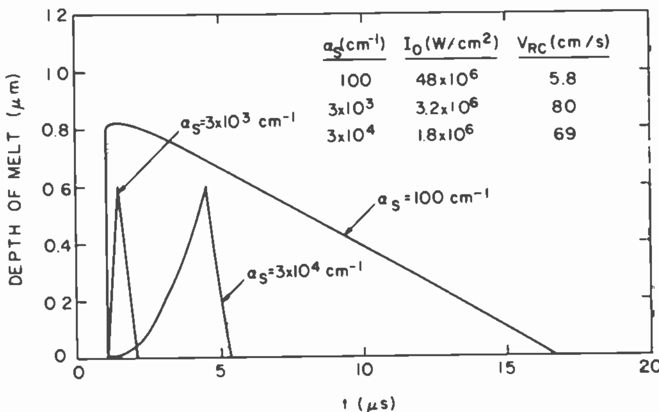

Fig. 14—Time dependence of the melt depth for the model solution of Fig. 13.

Eq. [25] allows us to understand the behavior shown in Fig. 14. When $\alpha_S = 100\ cm^{-1}$, a high value of $I_0 = 4.8 \times 10^6\ W/cm^2$ is required to reach threshold in 1 μsec; furthermore, as Fig. 13 shows, $(\partial T/\partial x)_{X_l+\delta x}$ is very low and these two factors lead to a very rapid rate of melting once threshold is reached. The reduced value of $I_0 = 3.2 \times 10^6\ W/cm^2$ coupled with the increased thermal gradient into the solid reduces the melt rate when $\alpha_S = 3 \times 10^3\ cm^{-1}$. For the large absorption coefficient, $\alpha_S = 3 \times 10^4\ cm^{-1}$, the velocity of melting is even further reduced, especially in the initial stages where the liquid thickness is inadequate to absorb all of the incident radiation ($d_M \lesssim 0.05\ \mu m$) further limiting the heat input that drives the progressive melting of the surface.

In each of the calculations of Figs. 13 and 14, the pulse was terminated when the surface was melted to a depth of 0.6 μm, and the temperature distribution at pulse termination is presented in Fig. 15. The distribution in the $\alpha_S = 100\ cm^{-1}$ case shows that the high incident pulse power has caused considerable temperature rise in the melted layer, and the surface temperature exceeds 2500°K (the boiling point of silicon is 2953°K). Another interesting feature of the temperature distribution is that the computed temperature in the solid close to the melt interface is several degrees above the melting point, even though the melt front has not penetrated to that region. This does not appear to be an artifact of the

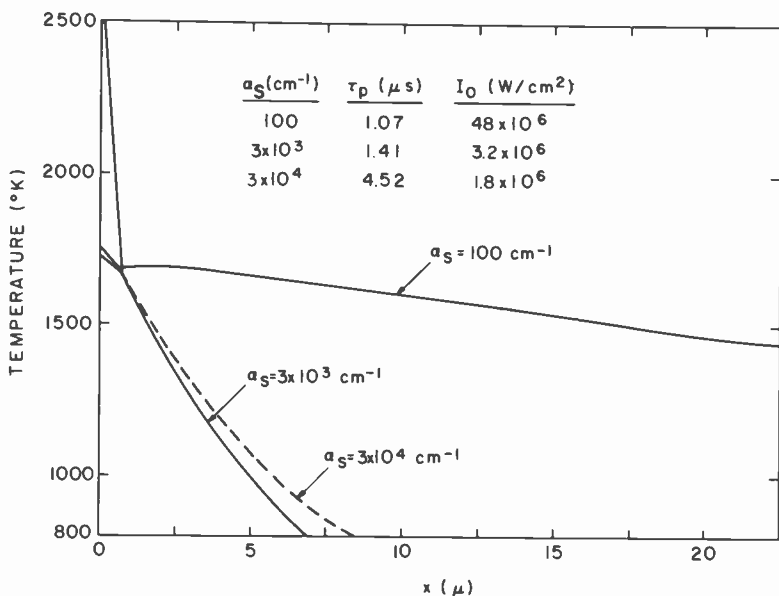

Fig. 15—Temperature distribution at pulse termination (d_M = 0.6 μm) for the model solutions of Fig. 13.

computation and is a result of the relatively uniform distribution of power absorption when the absorption coefficient is very low. During the initial stages of melting ($d_M \lesssim 0.05\ \mu m$), some of the incident radiation penetrates the liquid layer (this has partial transmission as shown in Fig. 4) and continues to be absorbed to great depths in the solid. Since the temperature profile at threshold is relatively flat (Fig. 13), enough energy is absorbed to elevate the solid region closest to the melt front beyond the melting temperature. Under these conditions, a very high stress could be developed in this superheated solid region; however, no experimental evidence has been reported thus far describing such an effect.

One consequence of the elevated temperatures reached in the liquid layer and the low thermal gradient in the solid at pulse termination for $\alpha_S = 100\ cm^{-1}$, is that a significant overshoot of the melt depth occurs after the laser pulse has ended. This is a direct result of the heat energy stored in the hot liquid being transported to the liquid/solid interface to supply more latent heat of melting after pulse termination. The overshoot is shown in Fig. 14. As can be seen the final melt depth is 0.8 μm when the pulse is terminated at $d_M = 0.6\ \mu m$.

The temperature rise in the melted layer is much less for the reduced incident pulse powers required when $\alpha_S = 3 \times 10^3$ and $3 \times 10^4\ cm^{-1}$. Consequently, there is a negligible overshoot, and the maximum melt penetration occurs at the end of the laser pulses (Fig. 14).

The maximum depth of melt penetration possible before surface boiling occurs is of some practical interest, especially when laser annealing is applied to the recrystallization of surface implanted samples. A simple relationship that will serve as a practical guide can be developed to relate the maximum melt depth to the incident power density of the annealing pulse. Since the absorption index of radiation in the liquid layer is very high for all of the currently used laser wavelengths, the relationship is essentially independent of the wavelength used. Assuming that the temperature gradient between the liquid surface and the liquid/solid interface is linear (justified when $\sqrt{\kappa_L \tau} > d_M$), the temperature drop across the liquid layer is $\Delta T = d_M(\partial T/\partial x)_L$ and the maximum depth of melt before surface boiling, D_M, is then given simply as

$$\Delta T = D_M \left(\frac{\partial T}{\partial x}\right)_L = -(T_B - T_M). \qquad [26]$$

Since the temperature gradient in the liquid is due to the transport of the absorbed energy to the liquid/solid interface

$$-K_L \left(\frac{\partial T}{\partial x}\right)_L \approx (1 - R_L)I_0, \qquad [27]$$

where K_L is the thermal conductivity of the liquid. Substituting into Eq. (24) gives

$$D_M \frac{(1 - R_L)I_0}{K_L} \approx T_B - T_M, \qquad [28]$$

or

$$D_M \approx \frac{(T_B - T_M)K_L}{(1 - R_L)} \frac{1}{I_0}. \qquad [29]$$

That is, the maximum melt depth before boiling is inversely proportional to the incident pulse power density. If the values $T_B = 2953°K$, $T_M = 1683°K$, $K_L = 0.64$ W/cm/°K, and $R_L = 0.73$ are used, Eq. [29] results in the relationship between D_M and I_0 presented in Fig. 16. Fig. 16 also contains the data computed by the thermal model for the two extremes of $\alpha_S = 3 \times 10^4$ and $\alpha_S = 100$ cm^{-1}, and good agreement with the simple expression derived above is seen for 0.3 μm $< D_M <$ 3μm, which is the region of most practical interest. The power density to produce melting is decreased as the pulse length is increased (Fig. 9); therefore, in order to melt to greater depths without causing surface boiling, it is more desirable to use longer pulse durations, and the choice of laser wavelength will have very little effect.

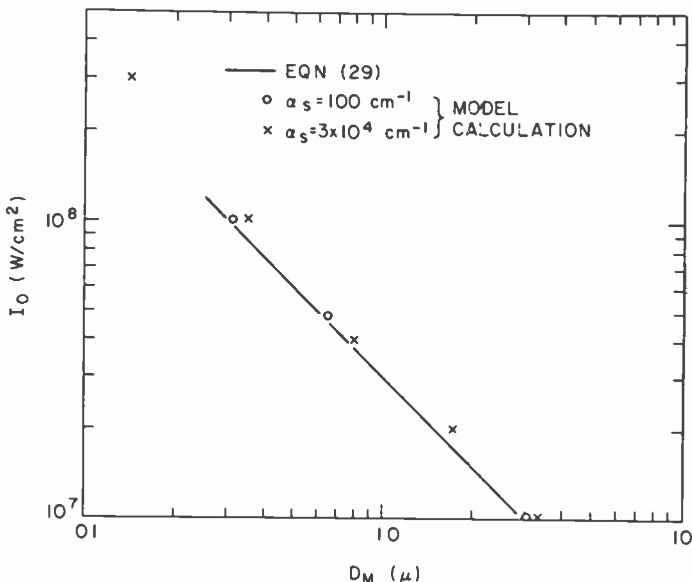

Fig. 16—Melt depth at which surface boiling first occurs as a function of the incident pulse power density. A comparison of the model solutions with the simplified Eq. [29].

The analysis also shows that for the longer, more weakly absorbed wavelengths, the velocity of melting above threshold is much greater than for strongly absorbed wavelengths. In addition, some overshoot occurs after pulse termination. The analysis shows that if very precise control of melt depth is necessary, it is more easily accomplished when the laser wavelength is strongly absorbed in the sample.

3.2.5 Dependence of Rate of Recrystallization on Absorption Coefficient and Pulse Duration

The rate of recrystallization is an important parameter in determining the effect of laser annealing on the sample. The velocity of the recrystallization front will determine the crystal quality of the annealed surface region and will also affect the distribution and solubility of any dopant atoms present in the surface layer. In those experiments (Table 5) where the laser pulse is used to induce alloying of a surface layer with the silicon, the velocity of recrystallization may also affect the compositional range of intermetallic compounds that are formed in the annealed region.

The data presented in Fig. 14 indicates that the velocity of recrystallization, V_{RC}, is strongly dependent on the coefficient of absorption of the radiation in the solid silicon and can vary by orders of magnitude depending on this parameter. V_{RC} will also depend on the pulse duration for any given wavelength.

The velocity of the freezing solid/liquid interface is determined by the temperature gradient in the solid immediately adjacent to the interface, $(\partial T/\partial x)_{X_l+\delta x}$. This temperature gradient determines the rate at which the latent heat of fusion liberated at the freezing front is transported away into the bulk of the sample. It is interesting to note that during the early portion of the recrystallization phase of laser annealing, the temperature of the remaining liquid layer drops to the melting point (but remains liquid) and the crystal growth occurs from an essentially isothermal ($T = T_M$) liquid layer. This is shown in Fig. 17 where the temperature distributions for $\alpha_S = 100$, 3×10^3, and 3×10^4 cm^{-1} are shown shortly after pulse termination, when the liquid layer thickness is still very close to its value at pulse termination.

The temperature gradient in the solid immediately adjacent to the freezing interface, $(\partial T/\partial x)_{X_l+\delta x}$, is related to the freezing velocity, V_{RC}, by the relationship

$$V_{RC} L\rho \approx -K_S \left(\frac{\partial T}{\partial x}\right)_{X_l+\delta x}, \qquad [30]$$

where K_S is the thermal conductivity of the solid at the melting point (0.25 W/cm/°K). Since the temperature gradient in the liquid is very small, we neglect the term in Eq. [30] that would correspond to heat diffusing to the interface from the liquid layer. Rearranging Eq. [30],

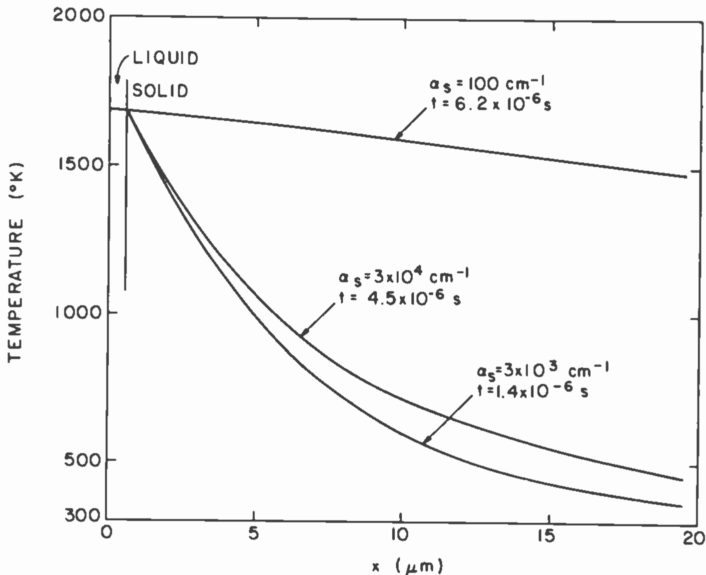

Fig. 17—Temperature distribution during cooling when $d_M = 0.6\ \mu m$ for the model solutions of Fig. 13.

$$V_{RC} \approx -\frac{K_S}{L\rho}\left(\frac{\partial T}{\partial x}\right)_{X_l+\delta x}. \qquad [31]$$

From this equation, it is clear that the much reduced value of V_{RC} computed for the $\alpha_S = 100\ \text{cm}^{-1}$ case (Fig. 14) is a direct result of the much lower thermal gradient extracting the latent heat of fusion from the freezing interface (Fig. 17).

For a given pulse power density the recrystallization velocity depends on the depth to which melting occurs. This is demonstrated in Fig. 18 where a pulse power density of $I_0 = 4 \times 10^7\ \text{W/cm}^2$ is used to produce melting to a depth of 0.1 μm, 0.3 μm, and 0.8 μm with $\alpha_S = 3 \times 10^4\ \text{cm}^{-1}$. The recrystallization velocity, measured during the final 0.1 μm of freezing falls from a value of 840 cm/sec to 560 cm/sec and 260 cm/sec as the melt depth is increased. This is a direct result of the increased duration of the pulse for deeper melts, permitting increased thermal diffusion, which in turn leads to a reduced temperature gradient $(\partial T/\partial x)_{X_l+\delta x}$ in the solid during the final phases of the recrystallization.

If we consider the case where surface melting occurs to only a limited depth, say, 0.1 μm, then when the recrystallization occurs the temperature distribution is essentially that which was developed at the threshold of melting. Some insight into the dependence of the recrystallization velocity on both absorption coefficient and pulse duration

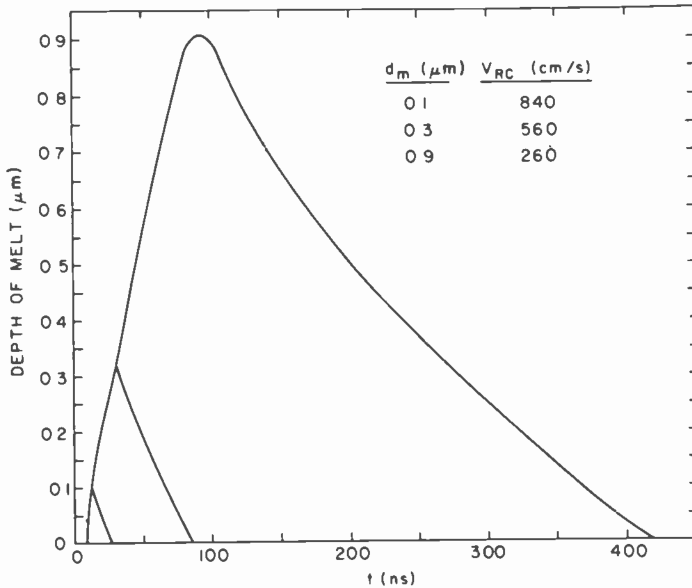

Fig. 18—Dependence of the recrystallization velocity on the depth of melt penetration for $\alpha_S = 3 \times 10^4$ cm^{-1} and $I_o = 4 \times 10^7$ W/cm^2.

is possible by considering the two limits of adiabatic and strong diffusion. Figs. 19 and 20 show the computed recrystallization velocity for a 0.1-μm melt depth as a function of incident pulse power density and pulse duration, respectively. In each case, the solutions were made for $\alpha_S = 100$, 3×10^3 and 3×10^4 cm^{-1}. As was the case with the threshold pulse parameters (Fig. 11), the adiabatic and strong diffusion limits are governed by the value of the characteristic time constant, τ_c, given by Eq. [23].

When $\tau_p \ll \tau_c$, the temperature gradient at the surface at the threshold of melting depends only on the spatial distribution of the energy absorbed from the laser pulse

$$A(x) = \frac{-dI}{dx} = \alpha_S(1 - R_S)I_0 e^{-\alpha_s x}. \quad [32]$$

Since no diffusion occurs in this adiabatic limit, the temperature distribution is given by

$$T(x) = \frac{A(x)\tau_p}{\rho C}, \quad [33]$$

so that the temperature gradient becomes

$$\frac{\partial T}{\partial x} = \frac{-\alpha_S^2 (1 - R_S)\tau_p I_0 e^{-\alpha_s x}}{\rho C}. \quad [34]$$

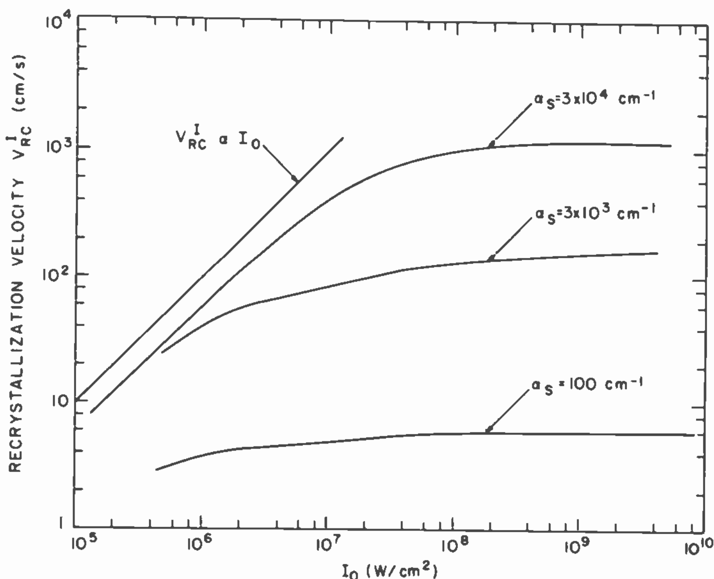

Fig. 19—Dependence of the initial recrystallization velocity V^I_{RC} from melt depths of 0.1 μm on the pulse power density for α_S = 100 cm^{-1}, 3 × 10^3 cm^{-1}, and 3 × 10^4 cm^{-1}.

However, since I_0 is just sufficient to cause melting in time τ_p, we can substitute from Eq. [18] into Eq. [34] to derive

$$\left(\frac{\partial T}{\partial x}\right) = -\frac{\alpha_S^2(1-R_S)\tau_p}{\rho C}\,\frac{C\rho T_M}{(1-R_S)\tau_p\alpha_S}\,e^{-\alpha_s x}. \quad [35]$$

Therefore,

$$\left(\frac{\partial T}{\partial x}\right)_{x=0} = \alpha_S T_M. \quad [36]$$

The initial recrystallization velocity for freezing as $d_M \to 0$ is then, from Eqs. [31] and [36],

$$\lim_{d_M \to 0} V_{RC} = V^I_{RC} = \frac{K_S \alpha_S T_M}{\rho L}. \quad [37]$$

If T_A is the ambient temperature (e.g., room temperature) Eq. [37] becomes

$$V^I_{RC} = \frac{K_S \alpha_S}{\rho L}(T_M - T_A) \text{ for } (\tau_p \ll \tau_c). \quad [38]$$

Eq. [38] predicts maximum recrystallization velocities for the three example values of α_S as shown by the asterisks in Fig. 20. The asymptotic

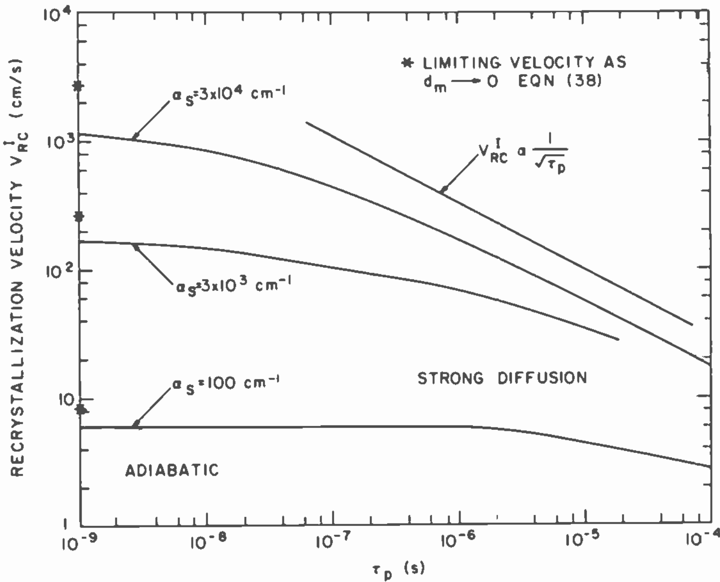

Fig. 20—Dependence of the initial recrystallization velocity V^{I}_{RC} from melt depths of 0.1 μm on the pulse duration time for α_S = 100 cm^{-1}, 3 × 10^{3} cm^{-1}, and 3 × 10^{4} cm^{-1}. The asterisks are the values computed from Eq. [38] as $V^{I}_{RC} = \lim_{d_M \to 0} V_{RC}$.

values ($\tau_p \ll \tau_c$) derived from the computer solution are somewhat smaller because the calculation is made for finite $d_M = 0.1$ μm. It is interesting to note that in the adiabatic limit, Eq. [38] predicts that the use of an elevated ambient temperature can be used to reduce the otherwise large values of the recrystallization velocity that occur for short pulses of strongly absorbed radiations.

When $\tau_p \gg \tau_c$, the strong diffusion limit is approached and the analytical solution derived in Ref. [35] can be used to determine the temperature gradient at the surface. From Eq. [12],

$$\left(\frac{\partial T}{\partial x}\right) = \frac{2(1-R_S)}{K_S} I_0 \left[\frac{-x}{2\kappa_S t}\left(\frac{\kappa_S t}{\pi}\right)^{1/2} \exp\left\{-\frac{x^2}{4\kappa_s t}\right\} - \tfrac{1}{2}\,\mathrm{erfc}\left(\frac{x}{2\sqrt{\kappa_S t}}\right) - \frac{x}{\sqrt{\pi}} \exp\left\{-\frac{x^2}{4\kappa_s t}\right\}\right], \quad [39]$$

i.e.,

$$\left(\frac{\partial T}{\partial x}\right)_{x=0} = \frac{-(1-R_s)I_0}{K_S}. \quad [40]$$

Substituting for I_0 from Eq. [20],

$$\left(\frac{\partial T}{\partial x}\right)_{x=0} = -\frac{1}{2}\left(\frac{\pi}{\kappa_S \tau_p}\right)^{1/2} (T_M - T_A), \quad [41]$$

so that

$$V^{l}_{RC} = \frac{K_S}{2\rho L}(T_M - T_A)\left(\frac{\pi}{\kappa_S \tau_p}\right)^{1/2}; \quad [42]$$

i.e.,

$$V^{l}_{RC} \propto \frac{1}{\sqrt{\tau_p}} \text{ for } (\tau_p \gg \tau_c), \quad [43]$$

which is the asymptotic behavior presented in Fig. 20 for the model solution.

It is interesting to note that in both limiting cases, and therefore throughout the entire range of the solutions, Eqs. [38] and [42] both indicate that, for any given conditions of absorption coefficient and pulse duration, the velocity of recrystallization can be reduced by performing the laser annealing at an elevated ambient temperature. This could provide a relatively straight-forward fine control of the recrystallization velocity to examine its impact on the physical properties of the annealed region.

3.2.6 Thermal Behavior During Final Cooldown

After the melted layer has completely recrystallized, the surface temperature continues to drop and the diffusion of energy away from the hotter surface region results in an essentially isothermal distribution through the thickness of the silicon wafer. The time constant for the leveling of the temperature distribution depends on the effective thermal diffusivity of the silicon during this cooldown period and on the thickness of the wafer. Taking a typical wafer thickness of 400 μm (~15 mil) the wafer will be isothermal for times in excess of a few msec after pulse termination. During this brief initial cooldown period, very little of the energy absorbed from the laser pulse will be lost from the wafer by radiation or convection. Thus, the isothermal temperature rise in the bulk of the wafer is given approximately by

$$\Delta T_{ISO} \approx \frac{E_{ABS}}{d_W \rho C} \lesssim \frac{E(1 - R_S)}{d_W \rho C}, \quad [44]$$

where d_W is the wafer thickness and E_{ABS} is the energy actually absorbed from the incident laser pulse of energy density E. The estimate given by Eq. [44] is an upper limit, because $E_A \lesssim (1 - R_S)E$ as a result of the increased reflectivity of the sample once surface melting occurs. In addition, if the laser beam is focused to dimensions comparable to the wafer thickness, radial diffusion will also limit the bulk temperature rise. Eq. [44] yields $\Delta T_{ISO} \leq 7$, 70, and 700°C for incident pulse energy densities

of 1, 10, and 100 J/cm^2, respectively. Thus, in the case of strongly absorbed radiation where experimental pulse energies are typically $\lesssim 10$ J/cm^2, the temperature rise in the bulk of the wafer after the pulse is negligible. On the other hand, when $\lambda = 1.06$-μm radiation is used to anneal pure silicon specimens, the pulse energy density can reach[27,28] 50–100 J/cm^2, so that a higher isothermal temperature may be reached, ~350–700°C. After the initial redistribution of the absorbed laser energy, which results in the isothermal temperature profile throughout the sample, the final cooldown to the ambient temperature proceeds via radiative and convective heat loss at the front and back surfaces of the wafer (to an essentially equal extent). In the computation we have used an emissivity of $\epsilon = 0.6$ and a convective transfer coefficient $G = 10^{-3}$ W/cm^2/°C (Eq. [4]). In Fig. 21 we show the time dependence of the surface temperature for the solution computed with $\alpha_S = 100$ cm^{-1} (see Figs. 13–15). In this case the wafer thickness was 212 μm (~7.5 mils) and the surface was completely refrozen at $t \approx 1.65 \times 10^{-5}$ sec (Fig. 14). Fig. 21 shows the initial energy redistribution phase taking place during $t \lesssim 10^{-3}$ sec. This is followed by the isothermal plateau region, which persists to $t \lesssim 1$ sec due to the limited surface heat losses. The final cooldown to ambient is completed after $t \lesssim 60$ sec. Of course, this final cooldown can be accelerated by using one of several practical techniques

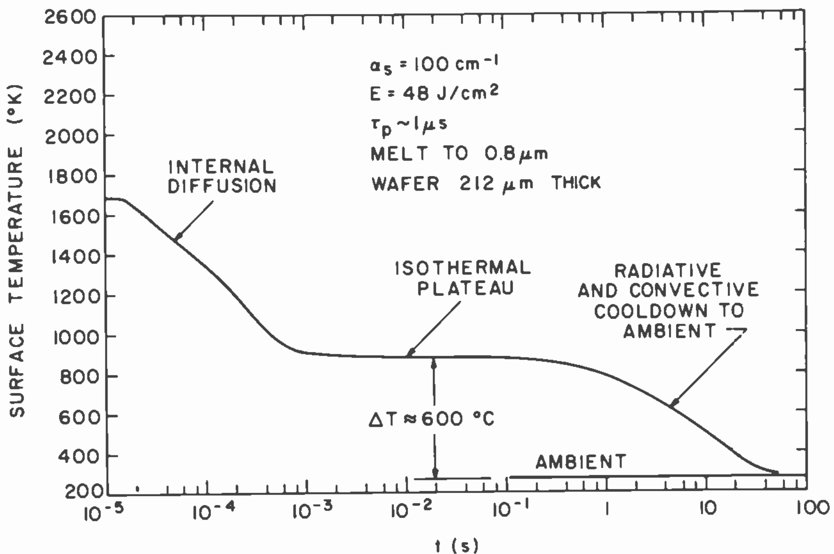

Fig. 21—Time dependence of the surface temperature after recrystallization showing the three phases of internal redistribution leading to the isothermal plateau and the final cooldown through radiative and convective heat loss from the surface.

to increase the convective heat losses (e.g., forced gas or liquid convection).

3.3 Comparison of Model with Experimental Results

In the model as described so far, the absorption coefficient of the solid is assumed to be constant throughout the sample. For pure semiconductor samples this is appropriate. When the sample has been ion-implanted, however, the bombardment results in the formation of a heavily damaged amorphous-like surface layer with correspondingly increased absorption coefficient (Table 6). Similarly the presence of a metallic surface layer on the sample requires careful treatment of the spatial dependence of the absorption coefficient.

3.3.1 Pure Semiconductor Materials (Table 6)

Experimental data[27,28] indicates that for $\lambda = 1.06\ \mu m$, the threshold pulse energy is nearly independent of pulse duration over the range $\tau_p = 110 \times 10^{-9}$ to 200×10^{-6} sec. The computed data from Fig. 11 ($\alpha_S = 100\ cm^{-1}$) indicates that $E^T = 45\ J/cm^2$ and $68\ J/cm^2$ for $\tau_p = 10^{-7}$ and 2×10^{-4} sec, respectively. These values are in good agreement with the experimental pulse energies[28] of $<55\ J/cm^2$ and[27] $60\ J/cm^2$ for $\tau_p = 10^{-7}$ and 2×10^{-4} sec, respectively.

For $\tau_p = 110$ nsec, Refs. [27], [28] reported annealing of damage to 10–25 μm depth when $E \approx 55$–$110\ J/cm^2$, corresponding to $I_0 = 5 \times 10^8$–$10^9\ W/cm^2$. According to our thermal model, although this power level and pulse duration can lead to melt depths of this magnitude, there will be a considerable amount of boiling at the surface of the specimen.

We have used a pulsed ruby laser ($\tau_p = 25$–30 nsec) to anneal electrically active recombination centers in the surface regions of silicon samples.[26] The distribution of defects causing recombination centers was examined before and after laser annealing using the electron beam induced current technique (EBIC). For pulse energy densities in excess of about $1\ J/cm^2$, the EBIC data showed that annihilation of the electrically active defects has occurred; in addition, surface ripples were observed using the Nomarski microscope. Using $\alpha_S = 4 \times 10^3\ cm^{-1}$ for the absorption coefficient at $\lambda = 0.69\ \mu m$ (Table 6), the computed threshold energy density when $\tau_p = 25$ nsec is $\sim 1.4\ J/cm^2$ (see Fig. 8). This is somewhat higher than the experimental value. The difference can be explained by the fact that the model does not include any increase of the absorption coefficient due to either the increased temperatures or the increase in the number of free carriers generated by the laser pulse

Table 7—Annealing of Electrically Active Defects in Pure Si Using a *Q*-Switched Ruby Laser[26] τ_{FWHM} = 25–30 nsec

Energy Density (J/cm²)	Exptl. Depth of Annealing (μm)	Computed Melt Depth (μm) (Fig. 21)
1.0	0	0.00
1.2	0.1–0.2	0.11
1.4	0.25–0.3	0.22
1.6	0.4–0.5	0.34
1.8	0.7	0.46

itself. If the experimental threshold of 1 J/cm² is used to 'calibrate' the thermal model, then a value of $\alpha_S = 7 \times 10^3$ cm^{-1} is necessary to reduce the computed threshold to the experimental value. Using the EBIC technique, it is possible to determine the depth to which annihilation of defects has occurred as a function of the above-threshold pulse energy density. Due to the nature of the EBIC technique, these experimental melt depths are systematically somewhat larger than the true depth of the melt. In Table 7, the experimental melt depths for a range of pulse energy densities are compared with the computed melt depth from the model, assuming a gaussian shaped pulse with FWHM = 27.5 nsec, and the agreement is reasonably good. The behavior of the melt front is shown in Fig. 22, where it is apparent that as the pulse energy increases, melting occurs at progressively earlier points in the pulse, penetrating to progressively greater depths.

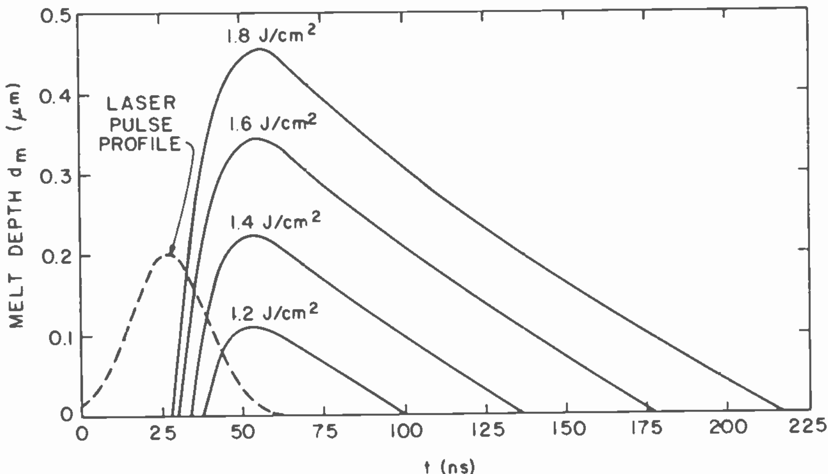

Fig. 22—Time dependence of the melt depth for gaussian pulses $\tau_{FWHM} = 27.5 \times 10^{-9}$ sec applied to pure silicon with $\alpha_S = 7 \times 10^3$ cm^{-1} (see text). The evolution of the melted region is shown for pulse energy densities of 1.2, 1.4, 1.6, and 1.8 J/cm².

The velocity of recrystallization from Fig. 22 is not very dependent on the energy density and is computed to be ~300 cm/sec. Since the estimated dislocation climb velocity is at least two or three orders of magnitude smaller than this value,[26] the defects are simply unable to keep up with the freezing front during recrystallization and are therefore absent from the recrystallized surface region.

3.3.2 Ion-Implanted Silicon Samples (Tables 1–3)

As we discussed above, the ion implantation process results in a surface layer that is essentially amorphous and that is therefore more strongly light absorbing than the rest of the wafer. The thickness of the amorphized layer depends on the energy of bombardment of the implanted ion, but typically is a few tenths of one micron ($<0.5\ \mu m$).

The computed pulse energy density thresholds for τ_P = 25, 50, and 110 nsec are summarized in Table 8 at $\lambda = 0.69\ \mu m$ and $\lambda = 1.06\ \mu m$ for spatially uniform amorphous and single-crystal values of the absorption coefficient (Table 6).

The experimental values for threshold pulse energy density at $\lambda = 0.69\ \mu m$ (Table 1) and $\lambda = 1.06\ \mu m$ (Table 2) are 1 J/cm^2 (τ_p ~50 nsec) and ~6 J/cm^2 (τ_p ~110 nsec). As would be expected these values are intermediate between those computed for the amorphous and the crystalline values of absorption coefficient. When $\lambda = 0.69\ \mu m$ and τ_p = 50 nsec, the computed values are 1.5 and 0.53 J/cm^2, respectively, and when $\lambda = 1.06\ \mu m$ and τ_p = 110 nsec, the computed values are 2.1 and 50 J/cm^2, respectively.

To demonstrate the effect of the higher optical coupling to the amorphized surface layer, the thermal model was modified to permit a surface region of specified thickness to have an increased absorption coefficient compared to the bulk of the sample.[11] In Fig. 23, the threshold pulse energy density (τ_p = 50 nsec) is shown as a function of the thickness of the amorphous layer ($\alpha_S = 3 \times 10^4\ cm^{-1}$) for $\lambda = 0.69\ \mu m$ ($\alpha_S = 3 \times 10^3\ cm^{-1}$ for single crystal). The threshold pulse energy is rapidly reduced towards the value for an entirely amorphous sample. This is due to the very small absorption depth in the amorphous silicon at this wavelength ($\alpha^{-1}_{amorphous}$ ~0.3 μm), so that only a relatively thin amor-

Table 8—Summary of Computed Threshold Pulse Energy Densities

	$\lambda = 0.69\ \mu m$		$\lambda = 1.06\ \mu m$	
τ_p nsec	single crystal J/cm^2	amorphous J/cm^2	single crystal J/cm^2	amorphous J/cm^2
25	1.4	0.42	50	1.8
50	1.5	0.53	50	2.0
110	1.8	0.71	50	2.1

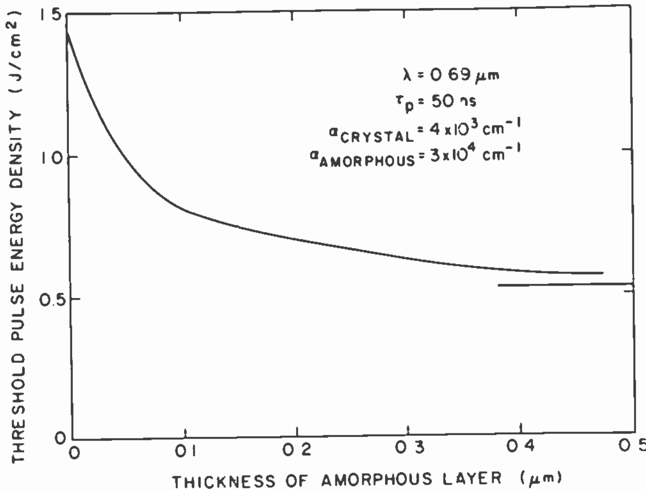

Fig. 23—Dependence of the melting-threshold pulse energy density on the thickness of an amorphous layer on otherwise single-crystal silicon. The absorption coefficient of the amorphous material was taken as 3×10^4 cm^{-1} and the crystalline material as 4×10^3 cm^{-1}, appropriate for $\lambda = 0.69$ μm. $\tau_p = 50$ nsec.

phized layer is needed for all of the nonreflected incident laser energy to be absorbed, leading to a thermal behavior equivalent to an arbitrarily thick and wholly amorphous sample.

In Fig. 24, similar data computed for $\lambda = 1.06$ μm is presented for a pulse duration $\tau_p = 110$ nsec. It is apparent that only a few tenths of a micron of amorphized silicon is required to reduce the threshold pulse density from a value of ~50 J/cm^2 for single-crystal silicon to ~6 J/cm^2, which is the experimentally determined threshold (Table 2).

Although it is consistent with the experimental data, this result is at first rather surprising, since the absorption length for amorphous silicon at this wavelength is $\alpha_S^{-1} \approx 3$ μm. The reason for the very large effect, even for thicknesses much less than α_S^{-1}, is that for this pulse length the thermal diffusion length in the silicon is limited to only about 2 μm and the absorbed energy density at the surface is proportional to the absorption coefficient of the material at the surface. The absorption coefficient of the amorphous material at $\lambda = 1.06$ μm is 300× greater than that of the single crystal, and, due to the limited diffusion lengths, the heating process is nearly adiabatic, so that the pulse energy density required is also reduced by very large factors, even for thin amorphized surface layers. The temperature distribution at threshold for various amorphous layer thicknesses are compared in Fig. 25 for $\lambda = 1.06$ μm. Due to the relatively limited diffusion length during this pulse time (τ_p

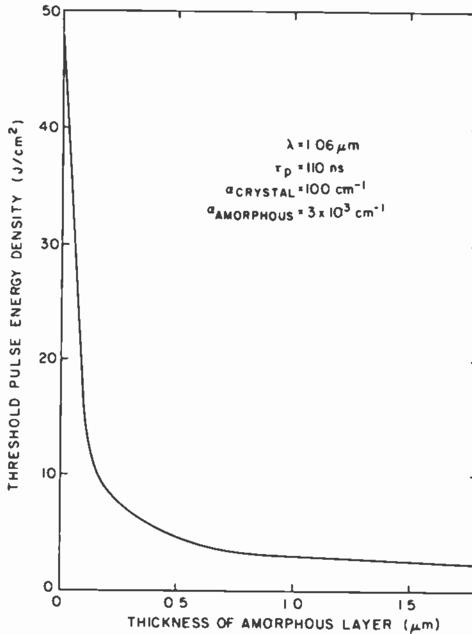

Fig. 24—Dependence of the melting-threshold pulse energy density on the thickness of an amorphous layer on otherwise single-crystal silicon. The absorption coefficient of the amorphous material was taken as 4×10^3 cm^{-1} and the crystalline material as 100 cm^{-1}, appropriate for $\lambda = 1.06$ μm, $\tau_p = 110$ nsec.

= 110 nsec), the temperature distribution strongly reflects the absorption intensity distribution within the sample, which is heavily weighted towards the surface of the sample.

3.3.3 Laser Induced Thin-Film Reactions (Table 5)

The thickness of the metal surface layers deposited on the sample generally ranges from 500 to 2000 Å, and, for metals such as Pt and Pd, this thickness is sufficient for the film to be essentially opaque at $\lambda = 1.06$ μm or less. For example, the absorption coefficient of Pt[45] at $\lambda = 1$ μm is $\sim 8 \times 10^5$ cm^{-1} and the reflectivity is 0.77. Allowing for the increased reflectivity of the Pt-coated specimen, the threshold pulse energy density to reach the melting point of silicon for $\tau_p = 110$ nsec can be deduced from Fig. 8 to be about 1.4 J/cm^2. This value compares well with the experimental figure of $\sim$2 J/cm^2 reported in Ref. [31].

The reflectivity of Pd at $\lambda = 1.06$ μm[46] is 0.83, so the fraction of the incident pulse energy absorbed is reduced still further. Applying the appropriate correction factor for the reduced absorption (Fig. 11) for

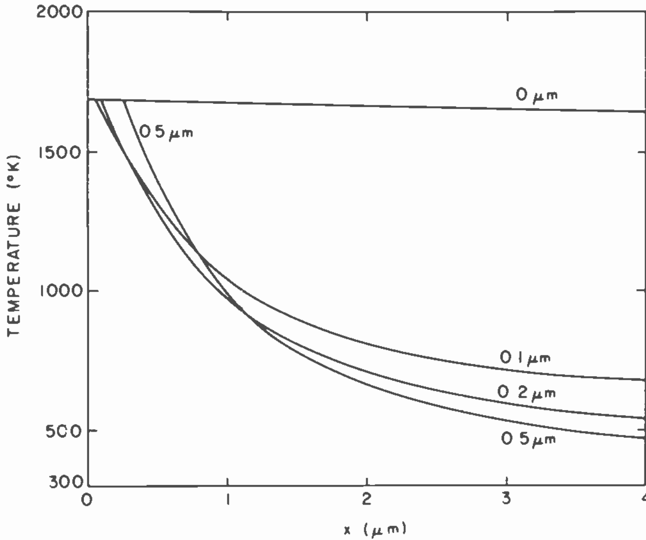

Fig. 25—Temperature distribution at the melting threshold when τ_p = 110 nsec and λ = 1.06 μm for various thicknesses of amorphous silicon at the surface of otherwise single-crystal silicon.

τ_p = 25 nsec indicates that the threshold pulse energy density to reach the melting point of silicon is ~1.2 J/cm^2. This figure is consistent with the experimental value reported in Ref. [32] of 1.2–1.6 J/cm^2. If the temperature at which the reaction occurs is less than that of the melting point of silicon, the estimated threshold pulse energy density from the model will be reduced. However, as was discussed earlier, since the reaction times are so short (comparable to the pulse duration), melting of the surface is probably required in order to achieve significant interdiffusion of the surface metal layer with the surface regions of the silicon.

4. Summary and Conclusions

A review of the published literature of laser annealing has shown that this technique is widely applicable to various thermal processes necessary in semiconductor device manufacture. Surface annealing of implantation damage or defect annealing in pure materials can be performed with extreme spatial precision, no special atmospheres, and no bulk degradation due to uniform heating of the specimen. The implanted impurity concentration in substitutional solid solution can be far in excess of that traditionally obtained using furnace annealing techniques. When laser

annealing is used to promote surface reactions between the semiconductor and a metal layer deposited on its surface, compositional variations are possible that could not be obtained by furnace-based processes. The apparatus of the laser annealing process is readily placed under automated control, so that this procedure represents an attractive possibility for high-speed computer-controlled device fabrication.

By developing a one-dimensional thermal diffusion model of the laser annealing process, we obtain a clarification in a general way of the effects of absorption coefficient (determined by the choice of laser wavelength) and pulse duration on the threshold pulse energy for melting, depth of melt, and recrystallization velocity. The thermal evolution of the irradiated specimen during the annealing pulse can be understood simply in terms of the characteristic time constant τ_c that separates the adiabatic ($\tau_p \ll \tau_c$) and the strong diffusion ($\tau_p \gg \tau_c$) regimes of the model behavior. When $\tau_p \ll \tau_c$, the threshold pulse energy density (Fig. 11) becomes independent of the pulse duration but increases proportionately as the absorption coefficient is decreased. The recrystallization velocity from $d_M \rightarrow 0$ thickness melts reaches a maximum value that is again independent of τ_p but that increases proportionately as the absorption coefficient increases. When $\tau_p \gg \tau_c$, the threshold energy density eventually becomes independent of α_S and increases as the square root of the pulse duration (Fig. 11). Similarly, the recrystallization velocities become independent of the absorption coefficient in this limit and decrease in inverse proportion to the square root of the pulse duration (Fig. 20). For any given set of τ_p and α_S the recrystallization velocity and threshold pulse energy densities can be reduced by performing the annealing at an elevated ambient temperature. Even at room-temperature ambient, the recrystallization velocity can be varied over a range of a few orders of magnitude (1–10^3 cm/sec) by appropriate choice of the annealing conditions.

The thermal model was compared to experimental results over a wide range of experimental conditions, including $\lambda = 0.69\ \mu m$ (ruby laser) and $\lambda = 1.06\ \mu m$ (Nd:YAG laser), with ion-implanted samples, pure samples, and samples coated with thin opaque metallic films. In all cases ($\alpha_S \approx 10^6 \rightarrow 10^2\ cm^{-1}$, $\tau_p = 20 \times 10^{-9} - 2 \times 10^{-4}$ sec) a reasonable agreement was found between reported experimental behavior and the prediction of the model. In particular, the model was able to predict the very strong reduction of the threshold energy density due to very thin (~0.3 μm) amorphous layers present at the surface of ion-implanted specimen.

Acknowledgments

During the course of this work, the author has benefited from discussions with L. L. Jastrzebski and C. P. Wu. The author would like to thank C. P. Wu for bringing this field of research to his attention.

References

[1] J. F. Ready, *Effects of High Power Laser Radiation*, Academic Press, New York, (1971).

[2] I. B. Khaibullin, E. I. Shtyrkov, M. M. Zaripov, M. F. Galyantdinov, and G. G. Zakirov, *Sov. Phys. Semiconductor*, **11**, p. 190 (1977).

[3] A. Kh. Antonenko, N. N. Gerasimenko, A. V. Bvurechenskii, L. A. Smirnov, and G. M. Tseitlin, *Sov. Phys. Semiconductor*, **10**, p. 81 (1976).

[4] G. A. Kachurin, E. V. Nidaev, A. V. Khodyachikh, and L. A. Kovaleva, *Sov. Phys. Semiconductor*, **10**, p. 1128 (1976).

[5] G. K. Celler, J. M. Poate, and L. C. Kimerling, "Spatially Controlled Crystal Growth Regrowth of Ion-Implanted Silicon by Laser Irradiation," *Appl. Phys. Lett.*, **32**, No. 8, p. 464 (1978).

[6] P. Baeri, S. U. Campisano, G. Foti, and E. Rimini, "Arsenic Diffusion in Silicon Melted by High-Power Nanosecond Laser Pulsing," *Appl. Phys. Lett.*, **33**, No. 2, p. 137 (1978).

[7] J. C. Muller, A. Grob, R. Stuck, and P. Siffert, "Laser-Beam Annealing of Heavily Damaged Implanted Layers on Silicon," *Appl. Phys. Lett.*, **33**, No. 4, p. 287 (1978).

[8] A. Gat, J. F. Gibbons, T. J. Magee, J. Peng, P. Williams, V. Deline, and C. A. Evans, Jr., "Use of a Scanning CW Kr Laser to Obtain Diffusion-Free Annealing of B-Implanted Silicon," *Appl. Phys. Lett.*, **33**, No. 5, p. 389 (1978).

[9] T. N. C. Venkatesan, J. A. Golovchenko, J. M. Poate, P. Cowan, and G. K. Celler, "Dose Dependence in the Laser Annealing of Arsenic-Implanted Silicon," *Appl. Phys. Lett.*, **33**, No. 5, p. 429 (1978).

[10] C. W. White, W. H. Christie, B. R. Appleton, S. R. Wilson, P. P. Pronko, and C. W. Magee, "Redistribution of Dopants in Ion-Implanted Silicon by Pulsed-Laser Annealing," *Appl. Phys. Lett.*. **33**, No. 7, p. 662 (1978).

[11] P. Baeri, S. U. Campisano, G. Foti, and E. Rimini, "A Melting Model for Pulsing-Laser Annealing of Implanted Semiconductors," *J. Appl. Phys.*, **50**, No. 2, p. 788 (1979).

[12] R. T. Young, C. W. White, G. J. Clark, J. Narayan, W. H. Christie, M. Murakami, P. W. King, and S. D. Kramer, "Laser Annealing of Boron-Implanted Silicon," *Appl. Phys. Lett.*, **32**, No 3, p. 139 (1978).

[13] A. Gat and J. F. Gibbons, "A Laser-Scanning Apparatus for Annealing of Ion-Implantation Damage in Semiconductors," *Appl. Phys. Lett.*, **32**, No. 3, p. 142 (1978).

[14] J. C. Shultz and R. J. Collins, "A Computer Simulation of Laser Annealing Silicon at 1.06 μm," *Appl. Phys. Lett.*, **34**, No. 1, p. 84 (1979).

[15] D. H. Auston, C. M. Surko, T. N. C. Venkatesan, R. E. Slusher, and J. A. Golovchenko, "Time-Resolving Reflectivity of Ion-Implanted Silicon During Laser Annealing," *Appl. Phys. Lett.*, **33**, No. 5, p. 437 (1978).

[16] R. T. Young and J. Narayan, "Laser-Annealing of Diffusion-Induced Imperfections in Silicon," *Appl. Phys. Lett.*, **33**, No. 1, p. 14 (1978).

[17] A. Gat, L. Gerzberg, J. F. Gibbons, T. J. Magee, J. Peng, and J. D. Hong, "CW Laser Anneal of Polycrystalline Silicon: Crystalline Structure. Electrical Properties," *Appl. Phys. Lett.*, **33**, No. 8, p. 775 (1978).

[18] K. Affolter, W. Luthy, and M. von Allmen, "Properties of Laser-Assisted Doping in Silicon," *Appl. Phys. Lett.*, **33**, No. 2, p. 185 (1978).

[19] P. Revesz, G. Farkas, G. Mezey, and J. Gyulai, "Epitaxial Regrowth of Evaporated Amorphous Silicon by a Pulsed Laser Beam," *Appl. Phys. Lett.*, **33**, No. 5, p. 431 (1978).

[20] J. C. Wang, R. F. Wood, and P. P. Pronko, "Theoretical Analysis of Thermal and Mass Transport in Ion-Implanted Laser-Annealed Silicon," *Appl. Phys. Lett.*, **33**, No. 5, p. 455 (1978).

[21] Various papers presented at the APS Meeting, March 1979. *Bull. Amer. Phys. Assoc.*, **24**, p. 315 (1979).

[22] H. J. Leamy, G. A. Rozgonyi, T. T. Sheng, and G. K. Celler, *Appl. Phys. Lett.*, **32**, p. 535, (1978).

[23] N. R. Iseno, "CO_2 Laser-Produced Ripple Patterns on Ni_xP_{1-x} Surfaces," *Appl. Phys. Lett.*, **31**, p. 148 (1977).

[24] J. C. Koo and R. E. Slusher, "Diffraction from Laser-Induced Deformation on Reflective Surfaces," *Appl. Phys. Lett.*, **28**, p. 614 (1976).

[25] G. N. Maracas, G. L. Harris, C. A. Lee, and R. A. McFarlane, "On the Origin of Periodic Surface Structure of Laser Annealed Semiconductors," *Appl. Phys. Lett.*, **33**, No. 5, p. 453 (1978).

[26] L. Jastrzebski, A. E. Bell, and C. P. Wu, to be published in *Appl. Phys. Lett.*

[27] M. von Allmen, W. Luthy, and K. Affolter, "Anisotropic Melting and Epitaxial Regrowth of Laser-Irradiated Silicon," *Appl. Phys. Lett.*, **33**, No. 9, p. 824 (1978).

[28] W. A. Porter, D. L. Parker, T. Wm. Richardson, and E. J. Swenson, "The Influence of Laser Annealing on Lattice Damage in Single-Crystal Silicon," *Appl. Phys. Lett.*, **33**, No. 10, p. 886 (1978).

[29] R. Tsu, J. E. Baglin, G. J. Lasher, and J. C. Tsang, "Laser-Induced Recrystallization and Damage in GaAs," *Appl. Phys. Lett.*, **34**, No. 2, p. 153 (1979).

[30] J. A. Golovchenko and T. N. C. Venkatesan, "Annealing of Te-Implanted GaAs by Ruby Laser Irradiation," *Appl. Phys. Lett.*, **32**, No. 3, p. 147 (1978).

[31] J. M. Poate, H. J. Leamy, T. T. Sheng, and G. K. Celler, "Laser-Induced Reactions of Platinum and Other Metal Films with Silicon," *Appl. Phys. Lett.*, **33**, No. 11, p. 918 (1978).

[32] M. von Allmen and M. Wittmer, "Dynamics of Laser-Induced Formation of Palladium Silicide," *Appl. Phys. Lett.*, **34**, No. 1, p. 68 (1979).

[33] Z. L. Liau, B. Y. Tsaur, and J. W. Mayer, "Laser Annealing for Solid-Phase Thin-Film Reactions," *Appl. Phys. Lett.*, **34**, No. 3, p. 221 (1979).

[34] A. Gat, J. F. Gibbons, T. T. Magee, J. Peng, V. R. Deline, P. Williams, and C. A. Evans, Jr., "Physical and Electrical Properties of Laser-Annealed Ion-Implanted Silicon," *Appl. Phys. Lett.*, **32**, p. 276 (1978).

[35] H. S. Carslaw and J. C. Jaeger, *Conduction of Heat in Solids*, Oxford, Clarendon Press, Second Edition, (1959).

[36] *Thermophysical Properties of Matter*, Volume 1, TPRC Data Series, IF, Plenum, New York (1970).

[37] A. E. Bell, "Thermal Analysis of Single-Crystal Silicon Ribbon Growth Processes," *RCA Review*, **38**, p. 109 (1977).

[38] M. H. Brodsky, R. S. Title, K. Weiser, and G. D. Pettit, "Structural, Optical, and Electrical Properties of Amorphous Silicon Films," *Phys. Rev.*, **B1**, No. 6, p. 2632 (1970).

[39] R. Hulthen, "Optical Constants of Epitaxial Silicon in the Region 1-3.3 eV," *Physica Scripta*, **12**, p. 342 (1975).

[40] W. C. Dash and R. Newman, "Intrinsic Optical Absorption in Single-Crystal Germanium and Silicon at 77°K and 300°K," *Phys. Rev.*, **99**, No. 4, p. 1151 (1955).

[41] K. M. Shvarev, B. A. Baum, and P. V. Gel'd, "Optical Properties of Liquid Silicon," *Sov. Phys. Sol. Stat.*, **16**, No. 11, p. 2111 (1975).

[42] A. A. Grinberg, R. F. Mekhtiev, S. M. Ryvkin, V. M. Salmanov, and I. D. Yaroshetski, "Absorption of Laser Radiation and Damage in Semiconductors," *Sov. Phys. Sol. Stat.*, **9**, No. 5, p. 1085 (1967).

[43] H. R. Philipp and E. A. Taft, "Optical Constants of Silicon in the Region 1 to 10 ev," *Phys. Rev.*, **120**, No. 1, p. 37 (1960).

[44] O. S. Heavens, *Optics of Thin Films*, Dover Press, New York (1965).

[45] *American Institute of Physics Handbook*, McGraw-Hill Book Co., Inc. New York (1963).

[46] P. B. Johnson and R. W. Christy, "Optical Constants of Transition Metals: Ti, V, Cr, Mn, Fe, Co, Ni, and Pd," *Phys. Rev.*, **B9**, No. 12, p. 5056 (1974).

Laser Annealing to Round the Edges of Silicon Structures*

C. P. Wu and G. L. Schnable

RCA Laboratories, Princeton, N.J. 08540

Abstract—Pulsed ruby laser annealing is shown to be capable of rounding the edges and corners of silicon islands on sapphire, of polysilicon interconnect lines used in double-level poly-Si devices, and of spikes and hillocks on epitaxial Si layers. It is thus expected to result in improved yield and dielectric integrity of integrated circuits.

In some cases the integrity of the thermally-grown oxide between the polycrystalline silicon gate areas and underlying islands of single-crystal silicon in SOS integrated circuits is not always as good as might be desired. Specific locations that are believed to be especially susceptible to localized dielectric breakdown include the edges (where the ⟨100⟩ surface intersects the ⟨111⟩ edges of the photolithographically delineated epitaxial silicon island) and the corners of the epi islands.

Laser annealing experiments were performed on an SOS sample in which the epitaxial silicon was patterned into small islands using a crystallographically preferential etchant of the type typically used for SOS IC production. Fig. 1(a) shows a scanning electron micrograph (SEM) of the area that was not pulse-laser annealed, and Figs. 1(b), 1(c), and 1(d) show similar areas that were annealed with ruby laser pulse power densities of 7.5 MW/cm^2, 15 MW/cm^2, and 20 MW/cm^2, respectively. The pulse width of the ruby laser was 25 nanoseconds. It can be seen from the SEM results that the edges of silicon islands on sapphire started to melt at ~7.5 MW/cm^2. Satisfactory rounded edges of the sil-

* The material in this paper was part of a presentation given at the 21st Electronic Materials Conference, Boulder, Colorado, June 27–29, 1979.

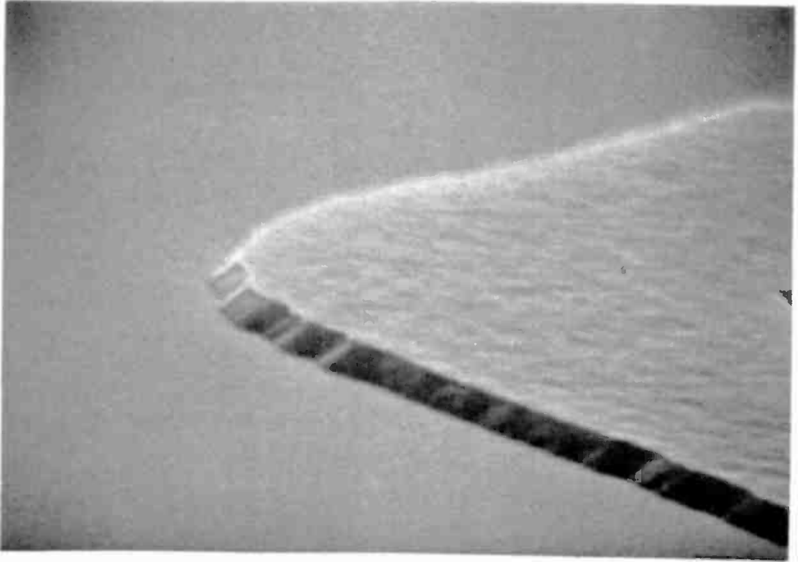

Fig. 1(a)—SEM picture of silicon island before pulsed laser irradiation (magnification 10K).

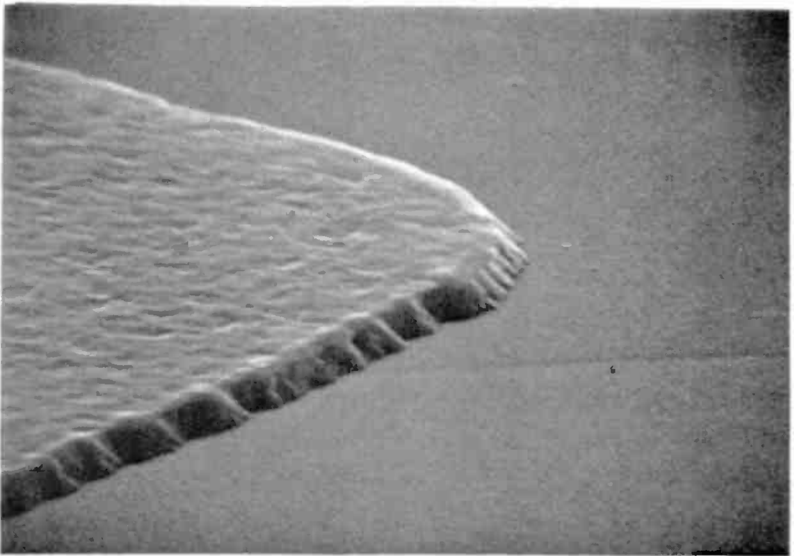

Fig. 1(b)—SEM picture of silicon island after pulsed ruby laser irradiation at 7.5 MW/cm^2 (magnification 10K).

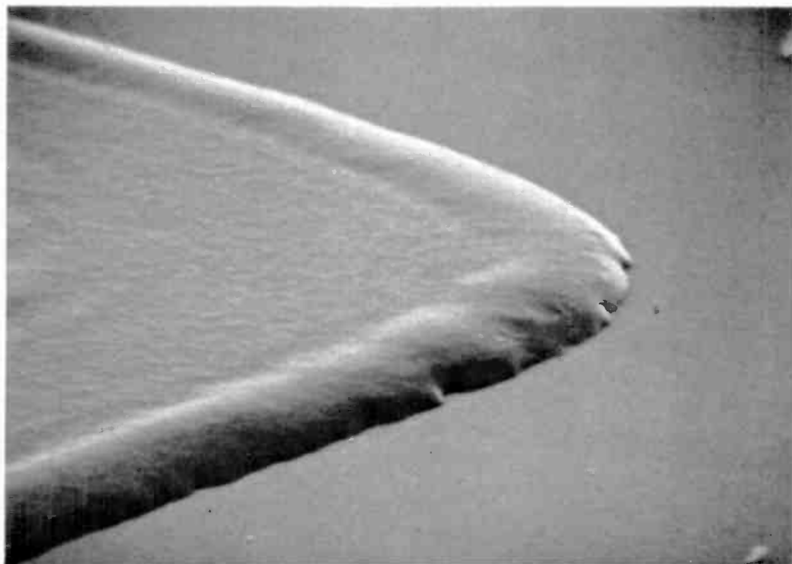

Fig. 1(c)—SEM picture of silicon island after pulsed ruby laser irradiation at 15 MW/cm^2 magnification 10K).

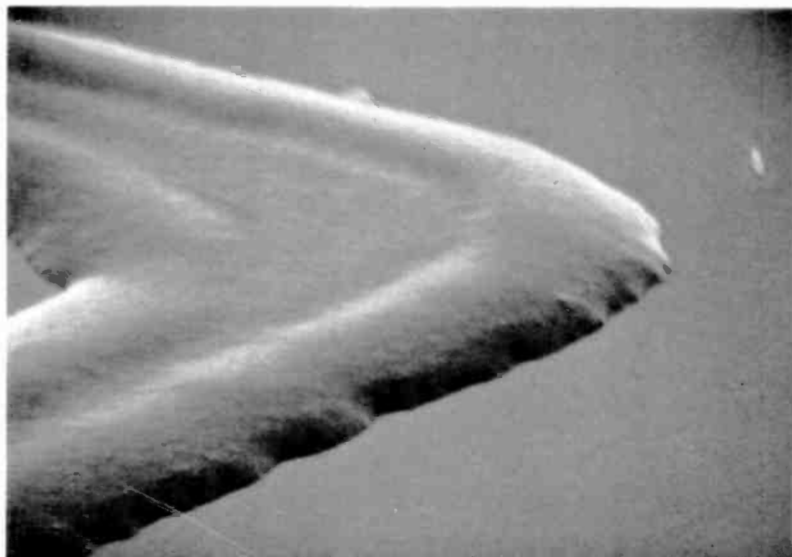

Fig. 1(d)—SEM picture of silicon island after pulsed ruby laser irradiation at 20 MW/cm^2 magnification 10K).

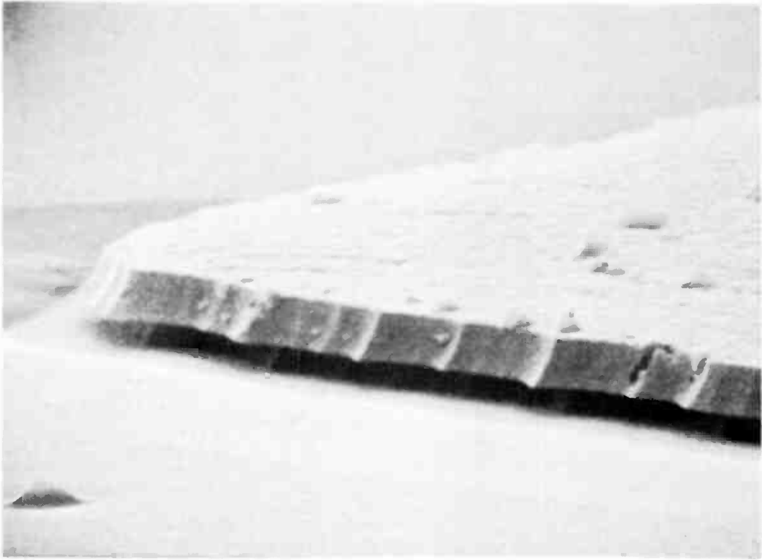

Fig. 2(a)—SEM picture of polysilicon island on oxide before laser irradiation (magnification 10K).

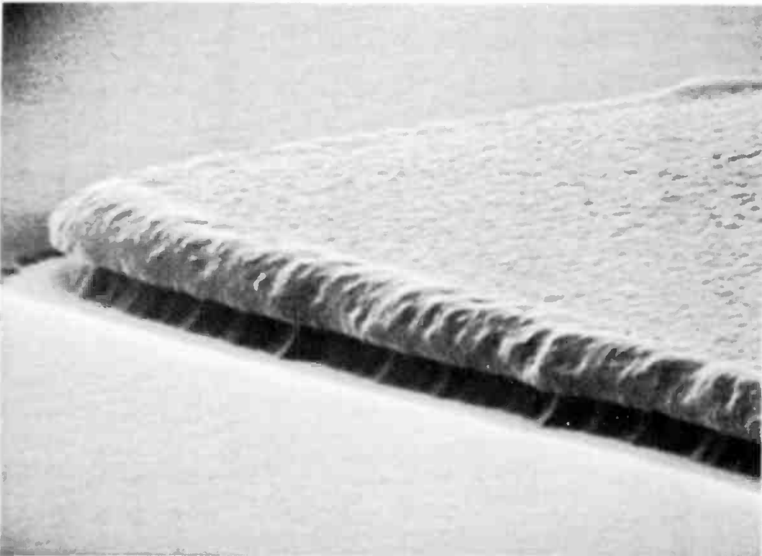

Fig. 2(b)—SEM picture of polysilicon island on oxide after pulsed ruby laser irradiation at 20 MW/cm^2 (magnification 10K).

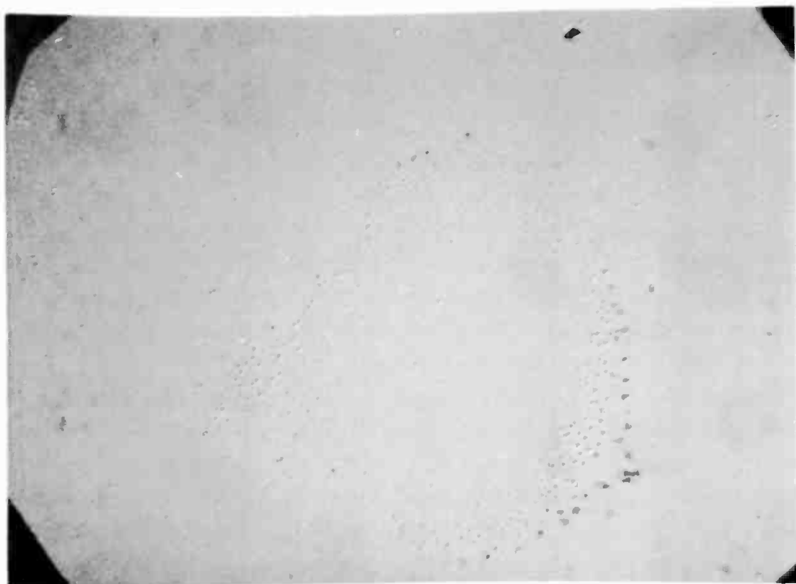

Fig. 3(a)—Nomarski photomicrograph of pits and hillocks on epi wafer before laser irradiation (magnification 500×).

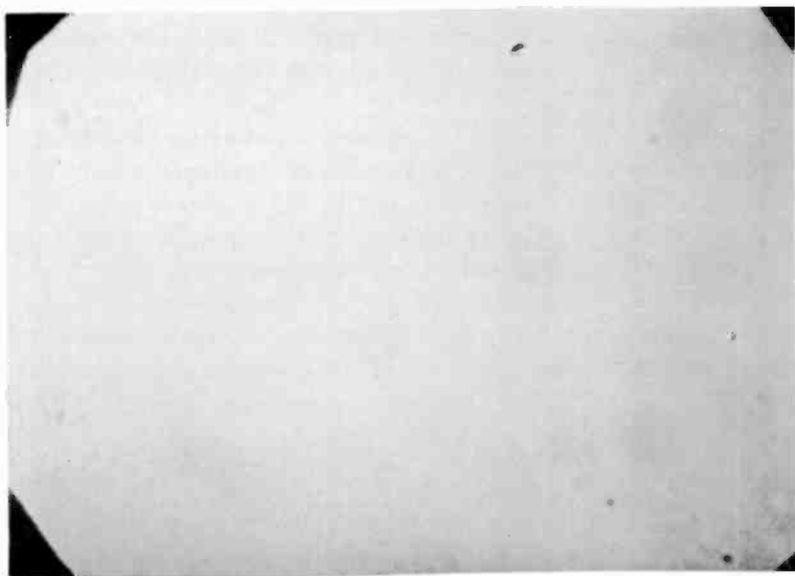

Fig. 3(b)—Nomarski photomicrograph of the same area as shown in Fig. 3(a) after pulsed ruby laser irradiation at 20 MW/cm^2 (magnification 500×).

icon islands on sapphire were obtained for ruby laser power density from 10 to 25 MW/cm^2, with the optimum ruby laser power density at ~15 MW/cm^2. Also, the surface of the silicon islands melted and re-froze to a more smooth surface, which would be beneficial in subsequent processing steps, such as photolithography, and would result in less pinholes in the grown oxide. Above 25 MW/cm^2 ruby-laser power density, the silicon island surface started to develop pits.

Edge-rounding by pulsed ruby laser beam can also be applied to double-level polysilicon devices. The polysilicon layers used for MOS gates or interconnects can be doped either *in-situ* during the polysilicon deposition, by ion-implantation, or by conventional diffusion, and then patterned into fine lines or islands using conventional photolithographic techniques. Pulsed laser annealing can then be carried out both to achieve lower polysilicon sheet resistivity[1] and to round the sharp edges and corners to improve oxide and/or metal coverage. Figs. 2(a) and 2(b) show the scanning electron micrographs of a patterned polysilicon layer before and after pulsed laser annealing, respectively. The power density of the ruby laser pulse was 20 MW/cm^2. It can be seen that pulsed-ruby-laser annealing can effectively round the edges and the corners in the fine patterns used in integrated circuits with relatively low power, and the process is expected to improve both the yield and the reliability.

Comparison of Figs. 1(a) and 1(c) shows that pulse laser annealing can also be used to improve the surface roughness of epitaxial wafers. This is demonstrated more dramatically in Fig. 3. Fig. 3(a) is a Nomarski photograph at 500× magnification of a "rough" spot on an epi wafer showing a collection of pits and hillocks. Fig. 3(b) shows the same area after a single ruby laser pulse at ~20 MW/cm^2 irradiation power density. Most of the pits and hillocks have disappeared due to melting of the surface layer during laser irradiation. Thus, it may be advantageous to laser anneal epi wafers before any other processing steps.

Reference:

[1] C. P. Wu and C. W. Magee, "Pulsed Laser Annealing of Ion-Implanted Polycrystalline Silicon Films", *Appl. Phys. Letts.*, **34**, p. 737 (1979).

Optical Recording With The Encapsulated Titanium Trilayer*

A. E. Bell, R. A. Bartolini, and F. W. Spong

RCA Laboratories, Princeton, NJ 08540

Abstract—There is an ever-increasing need to store and rapidly retrieve large quantities of information for such applications as TV broadcast studios and computers. These applications require: (1) recording as well as playback capability, (2) rapid random access of the stored information, and (3) playback with extremely high SNR (>50 dB) and/or low BER (10^{-9}). One particularly attractive technique for these applications is optical recording on a disc. The recording of information optically (laser recording) is attractive because it allows not only the instantaneous readout and very fast random access, but also a high recording density and an archival storage capability. Obtaining these features requires a laser, a modulator, a precision turntable and disc drive, computer controlled rapid (<1 sec) random-access mechanism, and as many as three servo mechanisms, all of which from a system-cost point of view make this system unattractive for consumer applications but extremely attractive for industrial applications. In this paper we discuss the encapsulated titanium trilayer optical recording structure, which has been designed for such industrial applications.

1. Introduction

We have previously reported[1] the design and optimization of two new antireflection designs for optical discs. This paper presents the results of further development of the titanium trilayer structure, specifically in the areas of encapsulation and substrate preparation.

There are several features of optical recording[2-4] that make this ap-

* Portions of this work were presented at the OSA/IEEE Conference on Laser and Electrooptical Systems, Feb. 1978, San Diego, CA.

proach highly suitable for the real-time recording of FM video or digital information for industrial applications. The packing density is limited only by the finite wavelength of the recording beam, so that up to one hour of video, or in excess of 10^{10} bits of digital information, may be recorded onto one side of a 12-inch-diameter disc. Programmable random access permits rapid readout of any segment of this store of information. For video applications, continuous playback of a single frame and fast, slow, or reverse motion effects are readily incorporated into the recorder/playback system. The recording characteristics of the encapsulated titanium trilayer disc will be discussed in terms of FM video-signal recording where the requirements on playback SNR are more stringent than for digitized information.

Fig. 1 shows a schematic of the optical video disc recorder/playback system used to evaluate the recording characteristics of the trilayer discs. The recording source is an argon laser operating at λ = 488 nm wavelength. For recording, the output of the laser is directed through an electro-optic modulator that intensity modulates the light in response to the input FM video signal. The modulated beam is expanded by the recording optics, and reflected by the polarizing beam splitter via a quarter-wave plate to fill the rear aperture of the recording lens. The objective lens focusses the beam to a recording spot with a diameter $<1 \mu m$ at the surface of the spinning disc. The disc rotation rate is 1800 rpm, so that a single recorded track corresponds to one video frame. For playback, an unmodulated beam of reduced intensity is directed onto the recorded track. The reflected light is intensity modulated due to the presence of the recorded pits and passes back through the objective lens and the quarter-wave plate. This beam, now rotated 90° in polarization by the two passages through the quarter-wave plate, is transmitted by

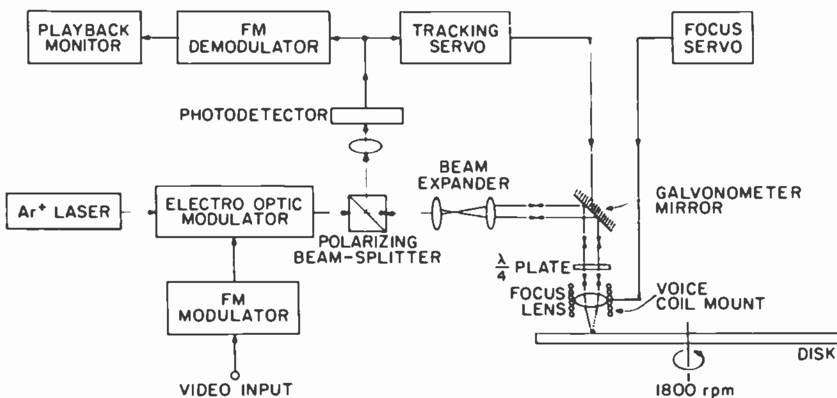

Fig. 1—Schematic of optical video disc recorder and playback system.

the polarizing beam splitter and is directed by the playback optics to the photodetector. The photodetector output corresponds to the original FM video signal recorded on the track. During both recording and playback, a capacitive focus servo maintains the focused spot in the plane of the recording medium by controlling the position of the objective lens within its voice-coil mounting. During playback a galvanometer mirror and tracking servo ensures that the playback spot is centered on the recorded information track.

2. Trilayer Design

The basic configuration of the trilayer structure is shown in Fig. 2. The structure consists of a reflecting layer of aluminum upon which is deposited a transparent dielectric layer followed by a relatively thin layer of strongly light absorbing recording medium. The optical properties of this structure have been discussed in detail in Ref. [1], and we note here that by choosing the appropriate thicknesses for the dielectric and absorbing layers, a strongly antireflecting condition can be obtained.

A computer calculation is performed to determine the optimum thicknesses for the dielectric phase layer and the absorber layer in the trilayer structure. Fig. 3 illustrates this procedure for the case of titanium trilayer, which has a silicon dioxide phase layer. The optical constants of titanium were determined by measuring the reflection and transmission of λ = 488-nm light through a vacuum-deposited layer of titanium of known thickness. As is often the case, the optical constants of the thin film, $n^* = 3.1 - i1.7$, differ somewhat from those of the bulk material.[5] For a selected thickness of the silicon dioxide layer, a calculation is made to determine that thickness of the titanium layer required to produce a minimum value of the reflectivity (which corresonds to maximum absorption in the titanium absorber layer). This computation is repeated for a range of silicon dioxide thicknesses, and the results are

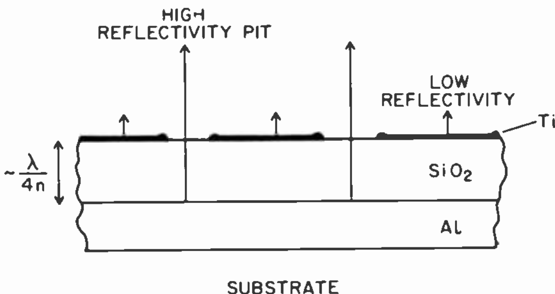

Fig. 2—The trilayer antireflection structure.

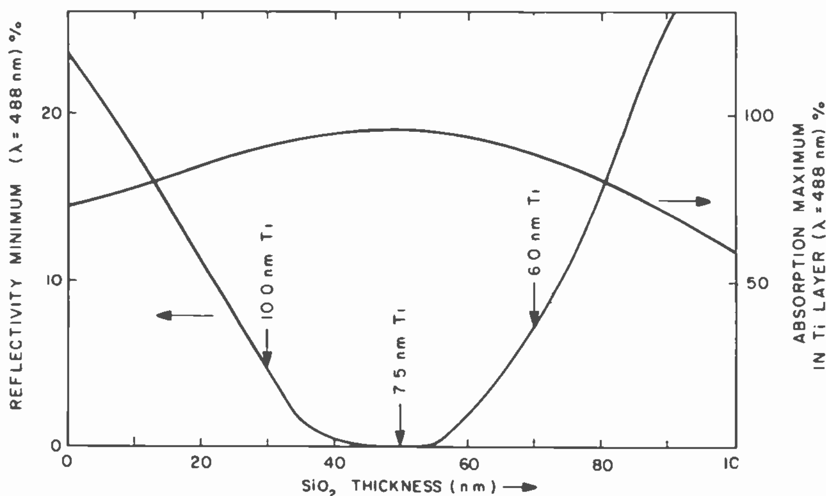

Fig. 3—Optimization for the titanium trilayer at λ = 488 nm.

plotted as a function of the silicon-dioxide-layer thickness in Fig. 3. This procedure permits the selection of the combination of dielectric absorbing layer thicknesses that leads to the trilayer structure having the lowest minimum reflectivity and, therefore, the highest optical coupling to the recording medium. In those recording systems where optical focusing is implemented, however, the structure with the lowest value of reflectivity may not provide sufficient return light for adequate focus control. In this case, a combination of layer thicknesses may be selected that lead to a detuned reflection minimum having increased reflectivity (~10%), with a corresponding reduction in the optical absorption in the recording medium.

The first step in the fabrication of the trilayer is to coat the substrate with about 40 nm of aluminum using standard resistive-boat high-vacuum deposition. The disc rotates at about 60 rpm during evaporation to ensure circumferential uniformity. The silicon dioxide layer is deposited using an electron-beam-heated source, and the thickness is monitored using a quartz crystal oscillator. The quartz oscillator is calibrated by using ellipsometry to measure the thickness of silicon dioxide deposited on a silicon wafer attached to the rotating disc. It is possible to control the silicon dioxide thickness to within 10% of the desired computed value. The final absorber layer of titanium recording medium is deposited using an electron beam vacuum system, and the evaporation is controlled and terminated by continuously monitoring the reflectivity of the disc surface at the recording wavelength. During evaporation, the reflectivity drops continuously from a value close to that of the aluminum

reflector layer, and the evaporation is terminated when the reflection minimum is reached. The light source for the optical monitor consists of a microscope illuminator whose output is chopped and directed via a lens and a mirror inside the bell jar to the disc surface. The reflected beam is directed via a 488-nm transmission filter to a photodetector, the output of which is input to the phase sensitive amplifier. Use of a chart recorder displaying the output of the phase-sensitive amplifier is a convenient method for observing the reflection minimum.

3. High Quality Plastic Substrates

The high cost of precision ground glass discs, as well as their bulk, makes them quite unsuitable for any practical application of the optical disc system. There are a number of plastic materials that are relatively inexpensive to produce and that may be suitable for use as the optical disc substrate medium, e.g., poly(vinylchloride) (PVC), poly(methylmethacrylate) (PMMA), and Mylar.* Disc substrates made from any of these materials suffer from two basic problems, which are illustrated in Fig. 4. The first problem is that of surface runout, which can easily be an order of magnitude more severe than specially polished plate glass. This problem is overcome by careful design of the focus servo,[2] the details of which will not be addressed here. The second problem concerns the quality of the plastic surface on a microscopic scale. Microscopic pits and surface roughness on the scale of one micron will severely degrade the quality of the playback signal from the disc. This is demonstrated in Fig. 5(a) which shows a playback video frame from a plastic substrate disc (PVC). Besides the numerous signal dropouts, the presence of observable texture in the image indicates a relatively low (<40 dB) SNR† due to materials associated noise sources. One solution to these problems is to

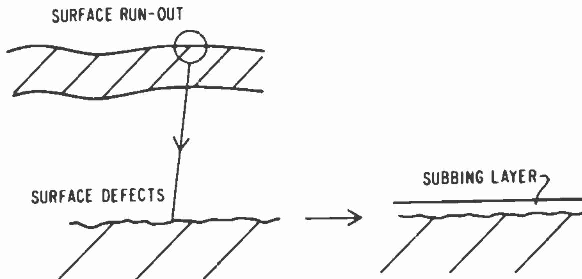

Fig. 4—Plastic substrates having both gross vertical run-out and microscopic surface defects.

* Registered trade name Dupont De Nemours, Inc.
† We measure SNR as peak-to-peak video signal divided by rms noise in 4.2 MHz video bandwidth.

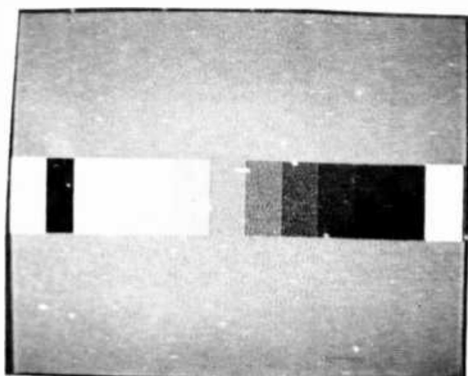

(a)

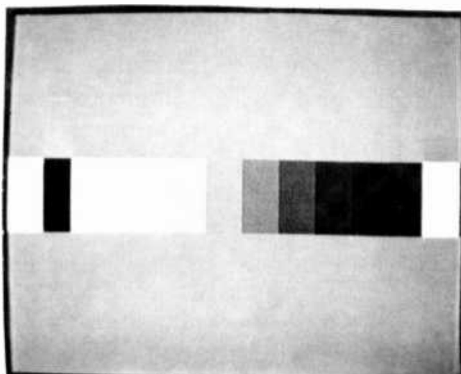

(b)

Fig. 5—Video playback from recordings made on discs having a PVC substrate (a) with no subbing layer and (b) pre-coated with subbing layer.

pre-coat the plastic substrate disc with a thin subbing layer of plastic material, which is applied by spinning techniques to a thickness of about 25 μm. On curing, the free boundary of this subbing layer hardens to form a high quality surface free from the microscopic defects that existed in the original substrate. Fig. 5(b) shows a playback video frame from a recording made on a PVC disc preconditioned with a subbing layer. We observe a high SNR (50 dB) and low dropout count equivalent to that obtained on specially prepared glass-substrate discs.

4. Trilayer Encapsulation

Precipitated dust particles that adhere to the surface of the recording

medium cause signal dropouts and are the most important source of deterioration of an optical video disc after fabrication. Due to the extremely high density of recorded information on the disc surface dust particles as small as one micron in size can result in a perceptible loss of video signal information on playback. In an experiment we exposed a trilayer video disc to the atmosphere of a typically dusty room environment and counted the number of detected playback signal dropouts in recordings made during successive days of dust exposure. We found that an average of about twenty additional dropouts occurred per frame of video information per day of exposure. Clearly such rapid degradation of the disc is unacceptable, and these results demonstrate the need for an effective protection mechanism against precipitated dust contamination.

The basic approach to this problem is to interpose a relatively thick layer of transparent material between the sensitive recording layer and the environment of the disc. The precipitated dust particles still accumulate on the surface of the encapsulating material, but they are so far

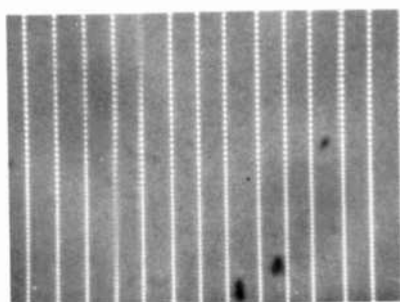

(a)

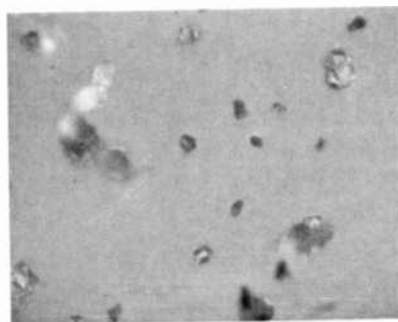

(b)

Fig. 6—Photomicrographs of encapsulated video disc (X500): (a) microscope focused on tracks recorded directly beneath the dusty region and (b) microscope focused on dust particles collected on surface of the overcoat layer.

removed from the plane of focus at the recording medium that their effect on either the recording beam or the reflected playback beam is insignificant. Of course, an encapsulating layer of a given thickness will provide immunity from dust only up to some particular limiting particle size. In general, therefore, the encapsulating layer should be as thick as possible and perhaps be used in conjunction with air filtering within the recorder/playback system in order to eliminate the larger dust particles ($\gtrsim 10$ μm). The effectiveness of the transparent encapsulating layer is shown in Fig. 6, which is a photomicrograph (500×) of a portion of an encapsulated disc (encapsulating layer 75-μm-thick) that has a number of particles up to 10 μm in diameter on the surface. In Fig. 6(b) the microscope is focused on the surface of the encapsulating layer, showing the presence of the dust particles. In Fig. 6(a), the plane of focus is changed to the tracks in the recording medium directly below the area shown in Fig. 6(b). As can be seen the visibility of dust particles is substantially reduced.

We have examined a number of materials for their suitability as an encapsulating medium, and our best results are obtained using a silicon rubber formulation (GE RTV615B). This material is most conveniently applied to the optical disc by the technique of spin-coating, with a subsequent heating cycle (24 hrs at 40°C) during which curing occurs. The resulting film is durable and of high optical quality. By choosing the appropriate spin-speed during the initial application, coatings with thickness of 50–150 μm are readily obtained.

To determine the effectiveness of the present thickness (75 μm) of overcoat layer in eliminating signal defects due to dust particles, we have exposed both overcoated and nonovercoated titanium trilayer discs to controlled quantities of alumina particles of various graded diameters (5, 11, and 22 μm). The results of this dusting experiment are shown in Table 1. Initially, 25 labeled tracks were recorded on both the overcoated

Table 1—Effect of Dust Particles in Increasing the Average Number of Detected Dropouts Per Recording (Track) for Nonencapsulated and Encapsulated Trilayers

Test Conditions	Number of Recordings	Average Defect Count Per Recording: Trilayer Disc	Average Defect Count Per Recording: Trilayer + RTV615B Disc
Readout Through 5-μ dust particles	25	+210	+2
Readout Through 5- and 11-μm Dust Particles	25	+550	+32
Readout Through 5-, 11-, and 22-μm Dust Particles	25	not measured	+114
Readout After Washing Disc	25	+9	—
Record and Readout Through Dust	10	+310	+474
Readout After Washing Disc	10	+310	—

and the nonovercoated discs and the average number of defects per track was measured. Each disc was then subjected to the identical controlled dusting with the graded particles, and the set of 25 tracks was relocated and the new average number of defects per track after exposure to the dust was measured.

As shown in the Table, in the case of the nonovercoated disc, both the 5-μm and the 11-μm particle exposure resulted in an average increase of about 200 and 300 defects per track, respectively. When the overcoated disc was subjected to the same level of 5-μm dust particles, no significant increase in defect count was observed, and even the 11-μm particle dusting was limited to producing an average increase of only 32 defects per track. The 22-μm particles resulted in a fairly substantial increase in the average defect count, even for the overcoated disc. We therefore conclude that a 75-μm overcoat is sufficient to eliminate playback defects due to particles of sizes 10 μm or less. Of course, a large number of particles larger than 10 μm are present in the typical environment, so that some additional precautions would be required to exclude such particles from the recording system and disc storage areas. Alternatively, the thickness of the overcoat layer may be increased and, aside from the cover glass correction necessary to the focusing objective, the recording characteristics of the disc would be expected to remain unchanged.

Table 1 also shows the average defect count per track when both recording and readout are performed through the dust layer. The figures given are average values for 10 recorded tracks. In the case of the nonovercoated disc, the defect count is reduced by almost a factor of two compared to the value for the prerecorded tracks read out through 5- and 11-μm dust particles. This may indicate that some of the smaller particles are removed or displaced by the action of recording. When this nonovercoated disc was washed to remove the dust particles and the same ten tracks re-examined, the average defect count (+310) remained unchanged. Microscopic examination showed portions of the track with some signal elements missing, presumably due to shadowing during recording by a dust particle that was subsequently washed away. On the other hand, the average defect count after washing for the 25 recordings made prior to the dusting returned almost to the level prior to dusting.

When recordings were both made and read out through the dust on an overcoated disc, the average defect count over 10 tracks (+474) showed a substantial increase compared to the average for recording without dust and readout through a dust layer (+114). This implies that when both record *and* readout beams intercept the dust, the degradation is compounded compared to playback only through a dust layer of tracks recorded in the absence of the dust.

5. Encapsulated Titanium Trilayer Recording Characteristics

The melting point of titanium (1668°C) far exceeds the temperature at which organic materials will melt or decompose. As a result, if we apply the RTV silicon rubber encapsulating layer direct to the top (titanium) surface of the trilayer structure, we must expect that the heat that diffuses into the overcoat layer (and also into the substrate) during the recording process will cause some thermal degradation of these layers. This localized disruption of the overcoat and substrate layers can only result in an increase in the materials noise associated with signal playback and is therefore quite undesirable.

To prevent thermal degradation of the plastic materials adjacent to the titanium trilayer structure, it is necessary to thermally isolate the latter by using a thermal barrier layer to prevent heat generated during recording from reaching the plastic materials. We have found that a layer of silicon dioxide of appropriate thickness provides adequate protection of both substrate and overcoat materials during recording. The thermal diffusion length through silicon dioxide during the ~50-ns duration of the pit-formation process is about 150 nm. Therefore, effective thermal

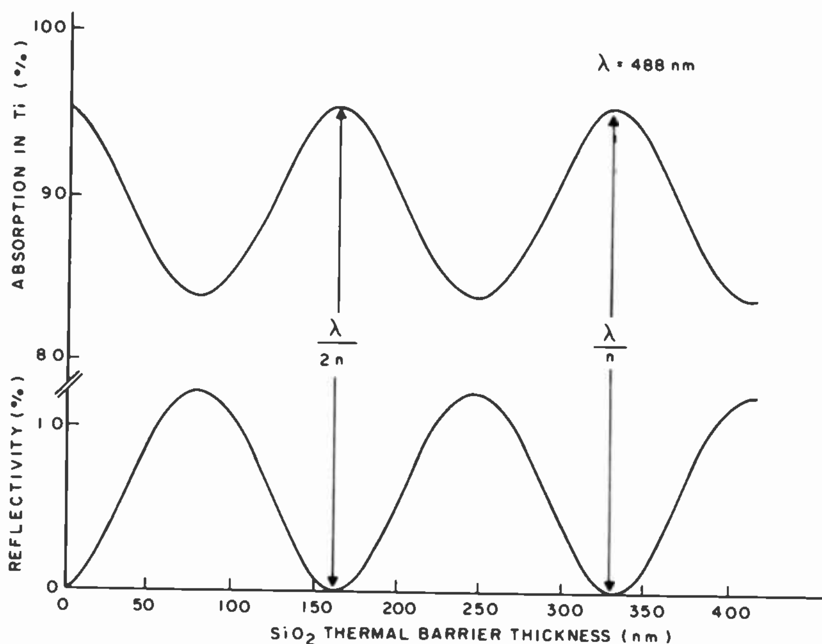

Fig. 7—Effect of a silicon dioxide overcoat thermal barrier on the optical characteristics of the titanium trilayer structure as a function of the barrier thickness.

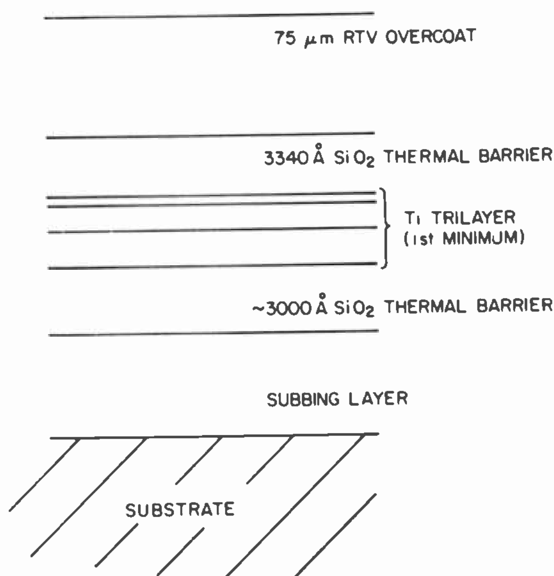

Fig. 8—Cross-section of the structure of a fully encapsulated first-minimum titanium trilayer disc.

isolation of the trilayer from the subbing layer and substrate is achieved by coating the subbing layer with about 300 nm of silicon dioxide. In this way, negligible temperature rise will occur in the subbing layer during recording, and thermal degradation will be avoided.

The thermal barrier layer protecting the overcoat material is an active component in the interference conditions of the trilayer itself. Fig. 7 shows the calculated reflectivity of an optimized trilayer structure ($\lambda = 488$ nm) as a function of the thickness of a silicon dioxide layer evaporated onto the surface of the structure. We observe that, provided the thickness of the silicon dioxide layer is an integral number of half wavelengths, i.e., $m\lambda/2n$, the optical properties of the combined structure are identical to those of the simple trilayer. For silicon dioxide at $\lambda = 488$ nm the refractive index, $n = 1.46$, so that a full-wave coating has a thickness of 334 nm. At this thickness the silicon dioxide provides an optically inert thermal barrier between the trilayer structure and the encapsulating medium of silicon rubber.

Fig. 8 shows the complete encapsulated titanium trilayer structure coated onto the plastic substrate, including a subbing layer and the two thermal barrier layers of silicon dioxide discussed above. Fig. 9 shows the recording characteristics of an optical video disc having the design shown in Fig. 8. The threshold for recording of the video signals occurs

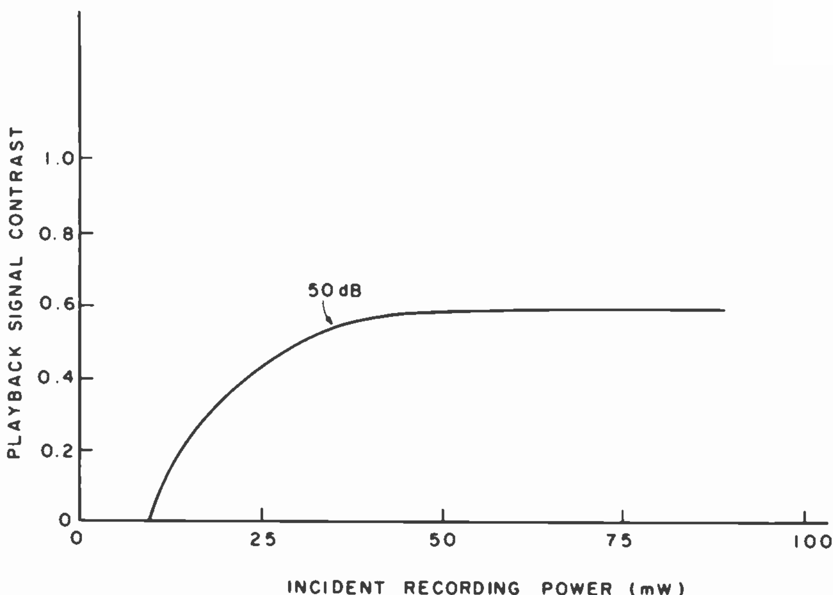

Fig. 9—Video signal recording characteristics for a fully encapsulated titanium trilayer disc with a plastic substrate (Fig. 8).

at about 12 mW incident recording power, and a playback SNR of 50 dB or greater is typically obtained for incident recording power levels in the range 25–40 mW.

A further refinement of the trilayer structure enables the thermal barrier between the aluminum reflecting layer and the subbing layer to be eliminated. As shown in Fig. 10, the reflectivity of the trilayer structure and also the absorption in the titanium layer are periodic functions of the silicon dioxide thickness. The antireflection condition is achieved when the silicon dioxide phase layer has any of the thicknesses given by

$$d_m = d_1 + (m - 1)\frac{\lambda}{2n}, m = 2, 3 \ldots,$$

where d_1 is the silicon dioxide thickness required to achieve the first reflection minimum condition. If the second-minimum thickness is chosen for silicon dioxide, d_2 = 217 nm, this is already sufficient to minimize the diffusion of heat from the titanium layer to the subbing layer, and a separate thermal barrier deposited beneath the aluminum layer is no longer required. A cross-section of a fully encapsulated second-minimum trilayer disc is shown in Fig. 11, and the recording characteristics of such a disc are shown in Fig. 12.

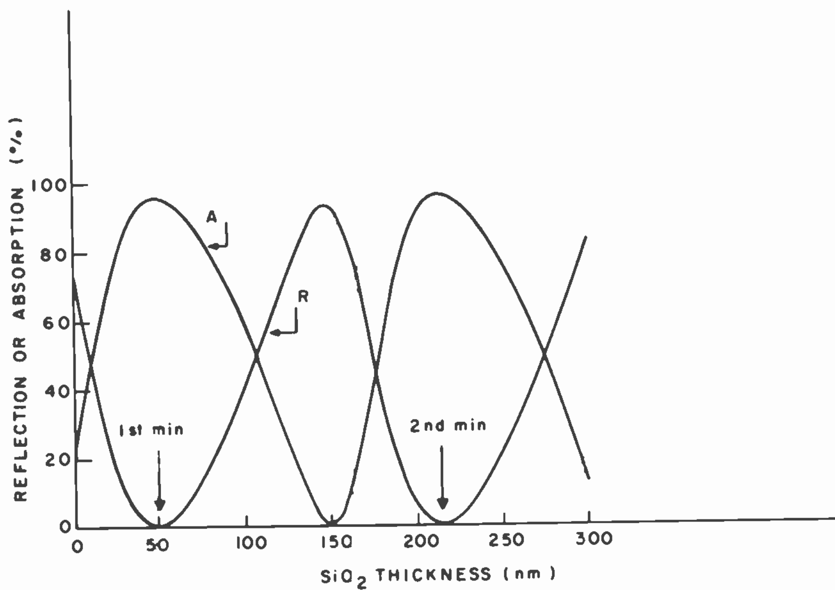

Fig. 10—Periodicity of the optical characteristics of a titanium trilayer structure as a function of the silicon dioxide phase-layer thickness.

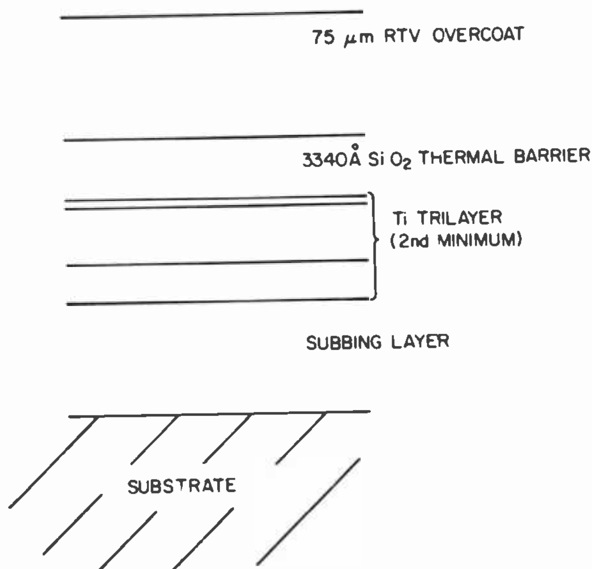

Fig. 11—Cross-section of the structure of a fully encapsulated second-minimum titanium trilayer disc.

Fig. 13 is a photograph of the photodetector output during playback from the fully encapsulated trilayer disc. Despite the fact that the thin recording layer of titanium is now sandwiched between the silicon

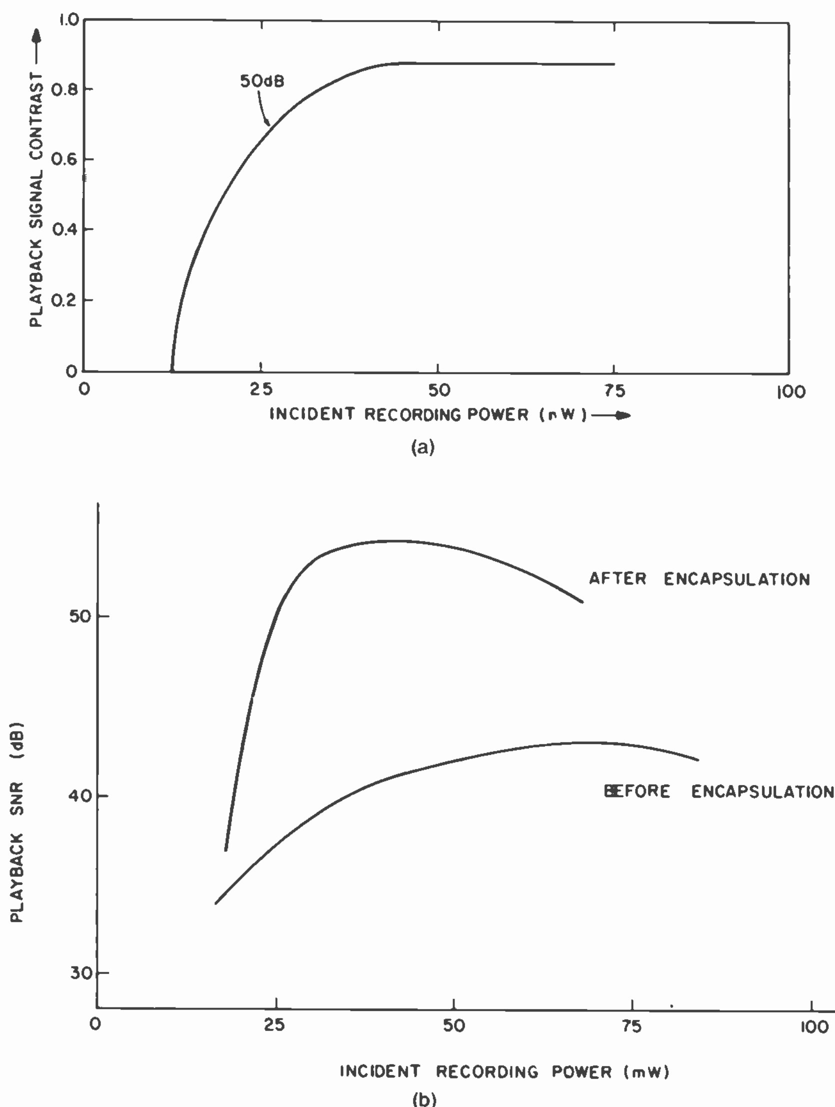

Fig. 12—Video signal recording characteristics of a second-minimum titanium trilayer disc: (a) playback signal contrast and (b) playback SNR as a function of incident recording beam power.

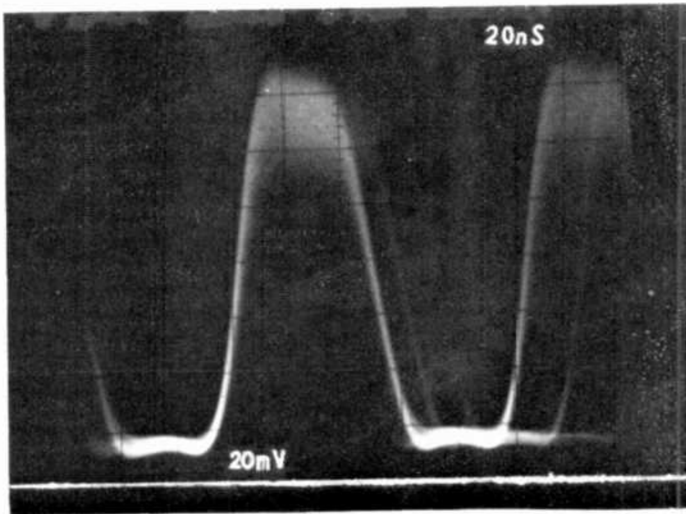

Fig. 13—Photograph of CRT displaying reflected light signal (photodetector output) during playback of encapsulated titanium trilayer.

dioxide layers of the phase layer and the encapsulating layers, the playback signal is well formed and the rise time is limited only by the finite diameter of the playback beam. The presence of the encapsulation layers does not degrade the recording characteristics of the trilayer disc. Indeed, as shown in Fig. 12(b), the playback SNR is generally improved by several dB as a consequence of the encapsulation procedure. Part of this improvement occurs because all recordings are made using a system that has a recording objective lens corrected for the spherical aberration that would otherwise be introduced by the thick encapsulation layer. This means that the optimum diffraction limited recording spot is only formed at the plane of the trilayer when the encapsulation is in place. However, we also find that the presence of the λ/n silicon dioxide thermal barrier improves the process of pit formation in the titanium layer, since the playback SNR increases typically by a few dB after deposition of this layer but prior to the spin-coating of the RTV.

To investigate the recording mechanism of the encapsulated titanium trilayer further, recordings were made after deposition of the λ/n silicon dioxide overcoat thermal barrier layer, but prior to application of the RTV coating. The SEM photograph of the recorded tracks (Fig. 14) demonstrates that some distortion of the silicon dioxide layer has occurred, resulting in the formation of raised bubbles in the regions where the titanium layer has been melted. This deformation of the silicon dioxide layer is more than sufficient to allow the melted titanium to draw

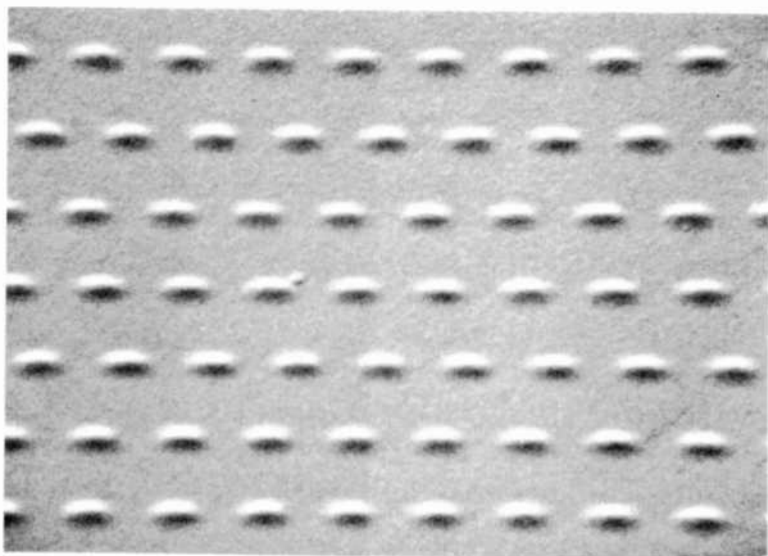

Fig. 14—SEM photographs of the bubble-like deformation that occurs on recording through the silicon dioxide thermal barrier.

back and form the recorded pit in the same fashion as is observed for the nonencapsulated trilayer.

Despite the similarity of recording characteristics of the first- and second-minimum titanium trilayer discs, their visual appearance is quite different. Although both designs have a low reflectivity at the recording wavelength (488 nm), the second-minimum design corresponds to an antireflection filter of a higher order. Thus, the reflectivity is much more sensitive to wavelength than the first-minimum design and increases rapidly for wavelengths other than the design optimum. The computed reflectivity of first- and second-minimum titanium trilayers is shown in Fig. 15, together with the corresponding absorption in the titanium layer. The low reflectivity across most of the visible spectrum gives the first-minimum design an overall blue-black appearance, whereas the second-minimum design leads to a magenta coloration.

5. Summary and Conclusions

Using the titanium trilayer approach, we have demonstrated the feasibility of obtaining extremely high quality (SNR $\gtrsim$ 50 dB) playback signals from a fully encapsulated recording medium deposited on an inexpensive plastic substrate. This performance is achieved with a recording beam power of 25 mW incident on the disc surface. The subb-

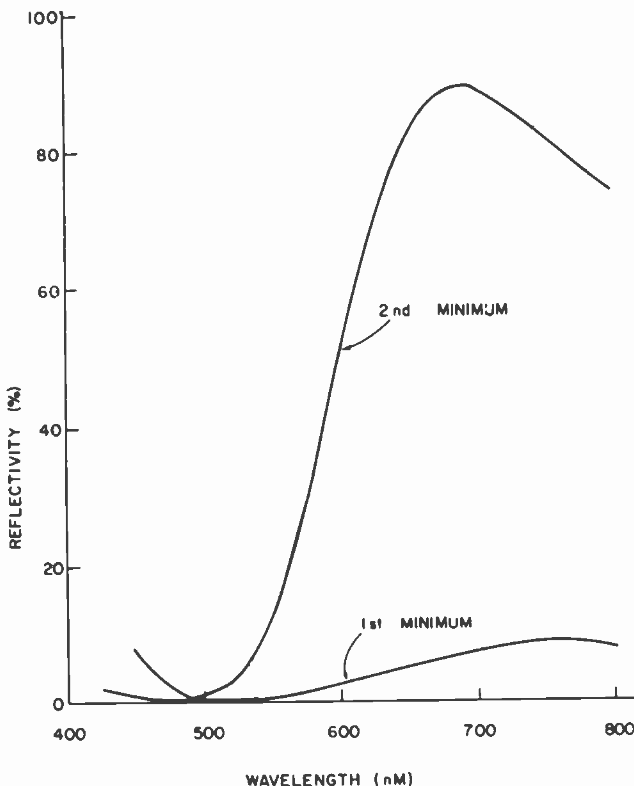

Fig. 15—Reflectivity of first- and second-minimum titanium trilayers as a function of wavelength.

ing-layer approach provides a simple and inexpensive technique for improving the surface quality of plastic substrates to a level comparable with that of an optically polished glass disc. We have shown that an overcoat layer of 75-μm thickness is sufficient to protect against signal defects due to dust particles of 10 μm or less diameter. We expect that increasing the overcoat-layer thickness will eliminate signal defects due to even larger particles and, in principle, we would expect the recording characteristics of such a disc to be otherwise unchanged. The titanium trilayer structure is thus most suitable for industrial applications such as high quality TV broadcast systems and programable rapid random-access computer applications.

Acknowledgment

The experiments were performed on an optical recording system origi-

nally developed by W. Barnette, R. E. Flory, R. W. Jebens, and M. Lurie. We wish to thank L. J. Levin, F. J. Tams, and D. Hoffman for technical assistance in disc fabrication and A. Bloom, C. B. Oakley, and B. F. Williams for technical discussions.

References:

[1] A. E. Bell and F. W. Spong, "Antireflection Structures for Optical Recording," *J. Quant. Electronics*, **14**, p. 487 (1978).

[2] R. A. Bartolini, A. E. Bell, R. E. Flory, M. Lurie, and F. W. Spong, "Optical Disk Systems Emerge," *IEEE Spectrum*, **15**, p. 20, Aug. 1978.

[3] G. C. Kenney, D. Y. K. Lou, R. McFarlane, A. Y. Chan, J. S. Nadan, T. R. Kohler, J. G. Wagner, and F. Zernike, "An Optical Disk Replaces 25 Mag Tapes," *IEEE Spectrum*, **16**, p. 33, Feb. 1979.

[4] K. Bulthuis, M. G. Carasso, J. P. J. Heemskerk, P. J. Kivits, W. J. Kleuters, and P. Zalm, "Ten Billion Bits on a Disk," *IEEE Spectrum*, **16**, p. 26, Aug. 1979.

[5] G. Haas and P. Bradford, *J. Opt. Soc. Amer.*, **47**, p. 124 (1957).

Patents Issued to RCA Inventors Second Quarter 1979

April

P. K. Baltzer Parallel Access Memory System (4,150,364)
L. J. Bazin Automatic Cable Equalizer Circuit (4,151,490)
T. L. Credelle, W. J. Hannan, and F. W. Spong Broadening the Spatial Frequency Pass Band of a Thermoplastic Layer (4,148,636)
W. R. Curtice Time Displaced Signal Sorting Apparatus (4,147,941)
D. A. DeWolf and C. A. Catanese Electron Multiplier Output Electron Optics (4,149,106)
S. S. Eaton, Jr. Voltage Boosting Circuits (4,149,232)
P. Foldes Helical Antennas (4,148,030)
P. Foldes Subwavelength Monopulse Antenna (4,148,035)
M. Glogolja Thermal Protection of Amplifiers (4,149,124)
L. A. Harwood, W. H. Groeneweg, and A. V. Tuma PAL Switching Control Circuit (4,148,058)
M. V. Hoover Frequency Discriminators (4,150,338)
S. K. Khanna Molding Composition (4,151 132)
R. M. Kongelka and P. L. Buess Switched Microphone Hang-Up Bracket (4,151,467)
J. K. Kratz and E. W. Christensen, 2nd Adjustable Yoke Mounting for In-Line Beam Color-Television Picture Tube (4,151,561)
I. Ladany Stripping of Protective Coatings from Glass Fibers (4,149,929)
D. W. Luz and J. C. Peer Complementary Latching Disabling Circuit (4,147,964)
B. G. Marks Interlocking Electron Tube Base and Adapter (4,148,541)
M. Nowogrodzki Surface Roughness Measuring Apparatus (4,148,027)
T. P. Ohrman Magnetic Tape Position Measuring System (4,151,566)
K. D. Peters Disc Caddy and Disc Player System Therefor (4,149,729)
M. A. Polinsky and W. N. Lewis Nonvolatile Semiconductive Memory Device and Method of Its Manufacture (4,151,538)
D. H. Pritchard Time Base Error Correction System (4,150,395)
T. J. Robe Folded-Cascode Amplifier Stages (4,151,482)
T. J. Robe Radiation-Hardened Transistor Amplifiers (4,151,483)
T. J. Robe Radiation-Hardened Transistor Amplifiers (4,151,484)
P. M. Russo Color Display Having Selectable Off-On and Background Color Control (4,149,152)
B. W. Siryj Thermal Processor (4,148,575)
J. Stark, Jr. Over-Voltage Amplitude Prevention Circuit for High Voltage and Deflection Generating System (4,149,209)
E. S. Thall and J. J. Moscony Method for Blackening the Surfaces of a Body of Ferrous Metal (4,149,908)
C. R. Wronski and B. Abeles Method of Making Camera Tube Target by Modifying Schottky Barrier Heights (4,149,907)

May

J. J. Benavie Corrective Optical Device for Homonymous Hemianopsia (4,155,633)
B. W. Beyers, Jr. Display System for Facilitating the Setup of a Tuning System (4,156,850)
A. Bloom and L. K. Hung Liquid Crystal Dyestuffs and Electro-Optic Devices Incorporating Same (4,153,343)
A. T. Crowley Phase-Locked Loop with Variable Gain and Bandwidth (4,156,855)
M. T. Gale, H. W. Lehmann, and R. W. Widmer Color Diffractive Subtractive Filter Master Recording Comprising a Plurality of Superposed Two-Level Relief Patterns on the Surface of a Substrate (4,155,627)
J. M. Hammer Optical Waveguide with Prism Coupler for Parallel Light (4,152,045)
K. G. Hernqvist Mercury Arc Lamps (4,156,826)
R. J. Hollingsworth and C. S. Kim Memory Array with Bias Voltage Generator (4,156,940)
M. V. Hoover High Power Protection Apparatus (4,156,264)
G. W. Hughes and H. Kawamoto Method and Apparatus for the Determination of Signal Pickup Qualities of a Stylus of a Capacitive Disc Video Player (4,152,641)
C. C. Lim Self-Regulating Deflection Circuit with Resistive Diode Biasing (4,153,862)
S. A. Lipp Image Display Employing Filter Coated Phosphor Particles (30,015)
J. M. Neilson Gate Turn-Off Semiconductor Controlled Rectifier Device with Highly Doped Buffer Region Portion (4,156,248)

W. Phillips Wave Device Having a Reverse Domain Grating (4,155,055)
E. S. Poliniak and N. V. Desai Method for Forming a Surface Relief Pattern in a Poly (Olefin Sulfone) Layer (4,153,741)
J. H. Regnault, Jr., and R. E. Benway Base Assembly for an Electron Tube (4,155,618)
W. R. Roach and I. Gorog Groove Depth Estimation System Using Diffractive Groove Effects (4,155,098)
L. R. Rockett, Jr. CCD Gray-to-Binary Code Generator (4,155,076)
W. W. Siekanowicz and T. L. Credelle Proximity Focused Element Scale Image Display Device (4,153,856)
L. H. Yorinks and R. M. Scudder Paraboloid Reflector Antenna (4,156,243)

June

S. Berkman, K. Kim, and H. E. Temple Apparatus for the Production of Ribbon Shaped Crystals (4,157,373)
W. R. Curtice Pulse Train Generator (4,158,784)
N. V. Desai and R. J. Himics Method for Purifying Methyl Alkyl Siloxane Lubricants (4,159,276)
R. A. Dischert Automatic Setup System for Television Cameras (4,158,208)
M. T. Gale and K. Knop Technique for Recording Micropicture-Information on a Diffractive Subtractive Filter Embossing Master (4,157,220)
A. Goldman Aqueous Photoresist Comprising Casein and Methylol Acrylamide (4,158,566)
J. J. Hanak Photodeposition of CRT Screen Structures Using Cermet IC Filter (4,157,215)
W. E. Harlan Video Signal Translating Circuit (4,158,852)
F. Z. Hawrylo Heterojunction Semiconductor Device (4,158,849)
K. G. Hernqvist Method of Reducing Absorption Losses in Fused Quartz and Fused Silica Optical Fibers (4,157,253)
M. V. Hoover Complementary-FET Driver Circuitry for Push-Pull Class B Transistor Amplifiers (4,159,450)
P. A. Levine CCD Comb Filters (4,158,209)
J. M. Neilson Semiconductor Device (4,158,206)
R. A. Nolan Implosion Protected CRT (4,158,419)
R. P. Perry Parallel Transform Analyzer for Performing the Chirp Z Transform (4,159,528)
O. H. Schade, Jr. Anti-Latch Circuit for Amplifier Stage Including Bipolar and Field-Effect Transistors (4,158,178)
J. L. Smith Magnetizing Apparatus and Method for Use in Correcting Color Purity in a Cathode Ray Tube and Product Thereof (4,159,456)
R. G. Thomas and K. Sadashige Dropout Compensator with Proportional Duration Dropout Detector (4,158,855)
C. M. Wine System for Reducing the Number of Binary Signals Representing Channel Numbers (4,158,815)
C. M. Wine Memory Type Tuning System with Provisions for Skipping Nonpreferred Tuning Positions (4,158,816)
H. A. Wittlinger Long-Tailed-Pair with Linearization Network (4,159,449)

AUTHORS

Robert A. Bartolini received a BSEE (1964) from Villanova University, an MSEE (1966) from Case Institute of Technology, and a PhD (1972) from the University of Pennsylvania. In 1966 Dr. Bartolini joined the technical staff of RCA Laboratories, where he has been involved in optical systems developments for a number of years. His work has included the development of optical recording materials for relief-phase and volume-phase holography, integrated optic devices, and optical data storage applications. He currently is responsible for the research and development of materials for optical data storage applications, such as optical discs, and is also Project Scientist under a Government contract for studies of optical recording materials. He holds twelve U.S. patents, and has received two RCA Laboratories Achievement Awards.

Prior to joining the staff at RCA Laboratories, he was a teaching assistant on the faculty of Case Institute of Technology and he is presently a lecturer in the Electronic Physics Department of the Evening Division at LaSalle College in Philadelphia. Dr. Bartolini is a senior member of IEEE and a member of Eta Kappa Nu, Tau Beta Pi, Sigma Xi, American Institute of Physics, and Optical Society of America. He is listed in *American Men and Women of Science.*

Alan E. Bell received his B.Sc. (Hons. 1st Class) in Physics from Imperial College, London University, in 1969. He was a graduate student in the Metal Physics group of the Physics Department at Imperial College and was awarded his PhD degree in 1973 for experimental work on the low-temperature magnetic and electrical properties of dilute alloys (Kondo effect). In 1973 he was awarded the Sarnoff Fellowship to visit RCA Laboratories at Princeton, N.J., to engage in postdoctoral research for a period of nine months. Working in the field of liquid crystalline materials, he used optical Raman scattering to study the molecular order in the nematic phase of the material. Since joining the technical staff at RCA Laboratories in 1974, Dr. Bell has been involved mainly in the optical-video-recording research program, both from an experimental and an analytical viewpoint. His work in the design and optimization of structures for optical recording has led to a new approach which allows significant improvements in the recording characteristics of metallic recording media. By this new approach, the basic feasibility for broadcast-quality optical video recording on a fully encapsulated recording medium has been demonstrated for the first time. Dr. Bell has developed numerical thermal models that provide a thorough description of laser-annealing experiments as well as the shaped growth of silicon ribbon for application to solar-cell fabrication.

Dr. Bell received an RCA Laboratories Achievement Award in 1975 and has been granted three U.S. patents. He is a member of OSA and IEEE, an Associate of the Royal College of Science, and a Diplomate of Imperial College, London.

Walter F. Kosonocky received the B.S. and M.S. degrees in electrical engineering from Newark College of Engineering, Newark, N.J., in 1955 and 1957, respectively, and the Sc.D. degree in engineering from Columbia University, New York, N.Y., in 1965.

Since June 1955, he has been employed at RCA Laboratories, Princeton, N.J. He became a Member of the Technical Staff in 1956 and was appointed Fellow of the Technical Staff in 1979. At RCA Laboratories Dr. Kosonocky has been engaged in research on solid-state devices, circuits, and system applications. This work included the following areas: ferrite memories, parametric digital circuits, tunnel diode circuits, applications of lasers as switching and digital devices, optical hologram memories, and MOS photosensor arrays. Since 1970, he has been engaged in the development of charge-coupled devices for digital, imaging, and signal processing applications. He has been issued 36 U.S. patents.

Dr. Kosonocky is a member of Tau Beta Pi, Eta Kappa Nu, and Sigma Xi. From 1973 to 1976, he was Chairman of the Solid-State Circuits Committee of IEEE's Circuits and Systems Society. From 1974 to 1978, he also served as Chairman of the Integrated Circuits Committee of IEEE's Circuits and Systems Devices Society. He has served on the Technical Program Committes of the 1977 International Electron Devices Meeting and the International Solid-State Circuits Conference from 1976 to 1978, and was the Technical Program Chairman of the 1979 International Solid-State Circuits Conference. He is presently the Chairman of the VLSI Committee of the IEEE Electron Devices Society.

Donald J. Sauer, having studied under a Regents Scholarship at the University of California at Los Angeles, was awarded the BSEE magna cum laude in 1969. Upon graduation he joined RCA, Electromagnetic and Aviation Systems Division, in Van Nuys, Calif. There he was responsible for state-of-the-art circuit designs for audio amplifiers, power supplies, and encoding/decoding devices utilizing the RCA GUAIII PMOS 100-gate universal logic array. In 1973 he began working on charge-coupled digital memory devices intended for the replacement of rotating magnetic drums, and successfully designed and demonstrated experimental 4K-bit and 16K-bit CCD memories.

In 1974, Mr. Sauer transferred to RCA Laboratories, Princeton, N.J., as a Member of Technical Staff. He continued working on CCD technology and has been responsible for the design, layout, and characterization of charge-coupled devices for imaging, memory, and signal-processing applications. Mr. Sauer is the inventor or coinventor named in four U.S. patents and has six patents pending. He has received two RCA Laboratories Outstanding Achievement Awards. In 1976 he received the award for contributions to a team effort in developing and demonstrating the feasibility of charge-coupled delay-line techniques for video-signal processing applications, and in 1978 for contributions to a team effort in the application of charge-coupled devices in color television receivers.

George L. Schnable received a B.S. degree in Chemistry from Albright College, Reading, Pa., in 1950, and M.S. and Ph.D. degrees in Chemistry from the University of Pennsylvania, in 1951 and 1953 respectively. From 1953 until 1971, he was employed by Philco-Ford Corporation, where he became Manager of the Advanced Materials and Processes Department in the R & D Operation of the Microelectronics Division. In 1971, Dr. Schnable joined RCA Laboratories, Princeton, N.J., as Head, Process Research, in the Process and Applied Materials Research Laboratory, where he supervised projects dealing with thin-film dielectrics and metallization, silicon device fabrication technology, ion-implantation technology, and silicon device reliability. In 1977, he was named Head, Solid State Process Research. He is presently Head, Device Physics and Reliability in the Integrated Circuit Technology Center of RCA Laboratories.

Dr. Schnable holds 20 U.S. Patents and is listed in American Men and Women of Science. He is a Member of the American Chemical Society, the Electrochemical Society, the Franklin Institute, the Pennsylvania Academy of Science, Alpha Chi Sigma, Phi Lambda Upsilon, and Sigma Xi; a Senior Member of the American Association for the Advancement of Science and the Institute of Electrical and Electronics Engineers; and a Fellow in the American Institute of Chemists.

Fred W. Spong received the B.S. degree in physics from the University of Utah in 1958 and the Ph.D. in physics from the University of California at Berkeley in 1964. He joined the technical staff of the RCA Laboratories, Princeton, N.J., in 1964. His activities have included work on gas lasers, holography, and television recording by various means including photography, electron beam, holography, and laser beam.

Dr. Spong is a member of Phi Beta Kappa, Sigma Xi, and the American Physical Society.

Chung P. Wu received the B.S., M.S., M.Phil., and Ph.D. degrees in Physics from Yale University in 1965, 1966, 1967, and 1968, respectively. He was a research staff physicist at the Yale Electron Linear Accelerator Laboratory from 1968 to 1970, working on photonuclear reactions and neutron time-of-flight spectroscopy. From 1970 to 1972 he was an Assistant Professor of Physics at Nanyang University in Singapore.

Since 1973, Dr. Wu has been a Member of Technical Staff at RCA Laboratories, Princeton, N.J., where he has worked on different techniques for determining the electrically active ion-implanted doping profiles, the utilization of ion implantation in the fabrication of semiconductor devices, and the characterization and evaluation of such devices. He is presently working on laser annealing of semiconductor materials, including polysilicon, crystalline silicon, SOS, and GaAs, for fabrication of solar cells, devices, and circuits. He has fifteen patents granted or pending.

Dr. Wu is a member of the American Physical Society, IEEE, and Sigma Xi.